New Instrumentation and Methods for Studying Heterogeneous Vapor Uptake by Aerosol Particles Ranging In Size From One Molecule to 10nm

A Dissertation
SUBMITTED TO THE FACULTY OF
UNIVERSITY OF MINNESOTA
BY

Derek Oberreit

IN PARTIAL FULFILLMENT OF THE REQUIREMENTS
FOR THE DEGREE OF
DOCTOR OF PHILOSOPHY

Christopher J. Hogan Jr., Peter H. McMurry

October 2013

© Derek Oberreit 2013

Acknowledgements

I feel incredibly fortunate to have had the co-advising duo of Chris Hogan and Peter McMurry. Their creativity, precision, knowledge, and motivation is infectious and I hope some of it has rubbed off on me. Just thanking them for their contribution doesn't feel adequate.

Being co-advised also let me be a part of two great lab groups. I feel that the culture of collaboration in both groups is uniquely strong and has made my experience all the better. From Chris' group I want to thank Ranga, Thaseem, Vinay, Carlos, Seongho, Hui, Mark, Sean, Seungkoo, Vivek, Jikku, and Hallie. Form Peter's group I want to thank Ranga, Mari, Jacob, Modi, Brent, Jun, Coty, and Julien. All of you have contributed to my work either by giving advice, helping with experiments, or being a welcome distraction when I needed a break. You may have caught that Ranga is mentioned twice. He and I shared co-advisors and therefore became very involved in each others work. He is a good friend and colleague and he deserves the double thanks. In addition to my lab members I want to thank my friends Lance, Vince, Rave, Becky, Ariel, Ben, Trask, and many others who joined me for much needed happy hours.

During my time in industry, I worked with several specific individuals who inspired me to be a better engineer and for being part of the reason I chose to return to school. I want to acknowledge Susanne Hering, Mark Stolzenburg, Stan Kaufmann, and the late Frank Dorman for their contribution although they probably didn't know they were making it.

Several people helped me out along the way either by providing recommendation letters, reviewing my writing, or just providing advice. In this category I wish to thank Susanne Hering (she also deserves double thanks), Jane Davidson, Fred Quant, Pat Keady, David Blackford, and Dave Landry. I also wish to acknowledge the mechanical engineering staff that provides the foundation for all of us to do this, specifically John Gardener, Mark Erickson, Holly Edgett, and Peter Zimmerman.

I also want to acknowledge the Department of Defense for supporting me for three years with the National Defense Science and Engineering Fellowship and the National Science Foundation for supporting me with the Graduate Research Fellowship for the remainder of my stay. I also want to acknowledge the Minnesota Supercomputing Institute for helping me make my simulations run in a reasonable amount of time.

Lastly and most importantly I want to thank my family (Claudie, Trent, and Kyle), my parents (Bill and Fran), and my friends (you know who you are) who have been incredibly supportive and never once gave me a hard time for quitting my job and chasing a dream.

Dedication

This dissertation is dedicated to my wife Claudie. You've earned it.

Abstract

Aerosol particles in the presence of a vapor will often change in size and composition due to heterogeneous vapor uptake. The physics and thermodynamics of this phenomenon are not well understood for particles less than ~10 nm where traditional models using bulk properties begin to break down. Further, existing methods for measuring/quantifying vapor uptake by particles are not effective for examining particles below 5 nm in size, and at relatively high vapor saturation ratios. This dissertation presents two new methods for measuring vapor uptake by aerosol particles in this size range. Each system measures the change in electrical mobility (which can be related to size) of aerosol particles when they are introduced to a vapor of known concentration. The first system consists of a tandem High Resolution Differential Mobility Analyzer – Drift Tube Ion Mobility Analyzer (HRDMA-DTIMS) for measuring uptake by particles ranging from ~2nm to >12nm, and the second system is a tandem HRDMA-Mass Spectrometer for measuring uptake by particles ranging from a single molecule to ~2nm. For the HRDMA-DTIMS system a new drift tube ion mobility spectrometer was developed and is described, with the goal of high resolution and fast measurement times. The device is capable of sub second mobility distribution scans and resolving powers similar to DMAs currently used in similar vapor uptake experiments. Measurement of water vapor uptake by hygroscopic salts of lithium iodide and sodium iodide particles compared to theoretical calculations exposes the flaws in existing vapor uptake models. The precision of the growth factor (wet diameter / dry diameter) measured using this system is shown to be ~0.2% for the presented data. For the HRDMA-MS system we are able to identify electrospray generated ions of a specific composition and then measure their change in electrical mobility as a function of relative humidity. Using this system we measured vapor uptake by alkyl halide salt cluster ions ranging from one to 27 molecules. We also describe how structures determined using density functional theory can be used to estimate the change in electrical mobility due to additions of vapor molecules. In addition to describing new instrumentation and systems, a model for estimating mobility changes based on collision mechanics as well as thermodynamics of individual molecule uptake is presented. This model can be applied to any vapor uptake measurement systems

Table of Contents

List of Tables vi
List of Figures vii
Chapter 1 Introduction 1
1.1 Motivation 1
1.2 Summary of Dissertation 4
Chapter 2 Mobility Analysis of 2 nm to 11 nm Aerosol Particles with an Aspirating Drift Tube Ion Mobility Spectrometer 7
2.1 Introduction 7
2.2 Experimental and Theoretical Methods 10
2.2.1 *DTIMS Prototype Overview* 10
2.2.2 *DTIMS Prototype Design* 15
2.2.3 *DTIMS Arrival Time Distribution Measurements* 16
2.2.4 *Predictions of Arrival Time Distributions & Simulation of Particle Trajectories* 18
2.3 Results and Discussion 32
2.4 Measurement of Multimodal Protein Aerosols 43
2.5 Enhancements to the Prototype Device 46
2.5.1 *Spatially Varying Fields* 46
2.5.2 *Time Varying Fields* 48
2.6 Conclusions 50
Chapter 3 Tandem High Resolution Differential Mobility – Drift Tube Ion Mobility Spectrometer Analysis 52
3.1 Introduction 52
3.2 Experimental Methods 54
3.2.1 *DMA-DTIMS System Description* 54
3.2.2 *Laboratory Measurements* 58
3.3 Results and Discussion 61
3.3.1 *Measurement Results* 61
3.3.2 *Comparison to Theoretical Predictions* 66
3.3.3 *Growth Factor Precision* 81
3.4 Conclusions 85
Chapter 4 Analysis of Heterogeneous Vapor Uptake by Cluster Ions via Differential Mobility Analysis-Mass Spectrometry (DMA-MS) 87
4.1 Introduction 87
4.2 Experimental Methods 89
4.2.1 *Differential Mobility Analysis-Mass Spectrometry* 89
4.2.2 *Measurement Analysis* 92
4.2.3 *Cluster Ion Structure & Collision Cross Section Calculations* 96
4.3 Results & Discussion 101
4.3.1 *Experimental Results* 101
4.3.2 *Comparison to Classical (KTR) Predictions* 103
4.4 Conclusions 105

Chapter 5 Conclusions and Future Work 113
5.1 Conclusions 113
5.2 Recommendations for Future Work 114
Bibliography 116
Appendix A Particle Trajectory Simulation 125
A.1 Instructions for using Fluent User Defined Functions 125
A.1.1 Setting up a UDF Within Fluent 126
A.1.2 Using UDFs For Particle Tracking Within Fluent 127
A.2 Modeling Porous Jump Surfaces in Fluent 128
A.3 Using ParticleTracker.exe 129
A.4 Using MovieMaker.exe 134
A.5 Using DTIMS Analytical.exe 135
A.6 LabVIEW program and Excel template 135
A.7 Source Code – Analytical Solver 136
A.8 Source Code – ParticleTracker.exe 140
A.9 Source Code – Movie Maker.exe 148
A.10 Source Code – Fluent UDF 152
Appendix B Schematics and Diagrams 160
B.1 DTIMS High Voltage Switcher 160

List of Tables

Table 3.1: A list of continuum and free molecular enhancement factors for the ion-dipole potential as a function of the dimensionless ion-dipole potential energy to thermal energy ratio. 71

Table 3.2: Parameters used for calculations performed here 77

Table 4.1: PA values using air as a probe radius 107

Table 4.2: PA values using water as a probe radius 108

Table 4.3: PA values using a zero probe radius 109

Table 4.4: Measured CCS ratios, temperature 1. 110

Table 4.5: Measured CCS ratios, temperature 2. 111

Table 4.6: Measured CCS ratios, temperature 3. 112

List of Figures

Figure 1.1: Operating ranges for existing instrumentation are shown in the hashed areas where TDMA = Tandem Differential Mobility Analysis, EDB = Electrodynamis balance, and HPMS = High Pressure Mass Spectrometry. Region A, shown in green, is the operating range for the high resolution DMA – Drift Tube Ion Mobility Spectrometer system. Region B, shown in red, is the high resolution differential mobility analyzer – mass spectrometer system. 3

Figure 2.1 a) Schematic of the DTIMS prototype. b) A three dimensional cutaway image of the DTIMS prototype 13

Figure 2.2: Depictions of (a.) the streamlines and isopotential lines at the DTIMS prototype inlet formed by the sample inlet flow and counterflow, (b.) the streamlines and isopotential lines formed by the counterflow at the prototype outlet, and (c.) relative isopotential lines (V/Vmax, where Vmax is the applied voltage) in the drift region. 14

Figure 2.3: Schematic of the system used for NaCl particle generation, DMA based electrical mobility section, and DTIMS electrical mobility analysis 16

Figure 2.4: Schematic of the system used for CPC response time distribution determination. 24

Figure 2.5: The normalized response time distribution functions, $\frac{df}{dt_{\det}}$, as measured with the system shown in Figure 2.4, for the CPCs used in this work.. 24

Figure 2.6: Depictions of characteristic particle trajectories through the drift region, for the indicated particle diameters (singly charged) and applied voltage. The colors of particle pathlines are varied with the drift time. 32

Figure 2.7: Normalized arrival time distributions (*dN*: the number of particles per measurement bin, *N*: the total number of detected particles, $d\log_{10}(t)$: the log-scale bin width) as a function of measurement time, as determined from experiments (circles), numerical based simulations (triangles), and the analytical based simulations (squares). The midpoint particle diameter (singly charged) selected by the upstream DMA is noted near the peak of each distribution. 34

Figure 2.8. (a.) Peak time in ATDs as a function of inverse mobility for DMA size selected particles from experiments (red circles), numerical based simulations (black triangles), and the analytical based simulations (white squares). (b). Dimensionless peak time as a function of Pe/Ψ_E 37

Figure 2.9. The number of detected particles during a measurement per unit inlet concentration as a function of Pe/Ψ_E. Red circles show measured values and black triangles show simulated results. 39

Figure 2.10. The system resolving power of for the DTIMS prototype determined with (a.) a 3786 WCPC and (b). a 3788 WCPC used as detectors. Red circles correspond to measured values, black triangles to simulation results, green triangles to simulation results neglecting detector influences, and open squares to analytical results. The scatter in the calculated results reflects the finite number of particles that were tracked numerically. 42

Figure 2.11: (a) Cytochrome C, (b) Lysozyme, and (c) Myoglobin ion electrical mobility spectra for DTIMS voltages of 1kV (black squares), 3kV (open diamonds), 9kV (black triangles), and published results using a high resolution DMA (red circles)..... 45

Figure 2.12: Particle pathlines and E_r contours for a spatially varying field. 48

Figure 2.13: Transmission efficiency including results from voltage ramping 49

Figure 3.1: (a.) Schematic of the DMA-DTIMS system. EAG: Electrospray Aerosol Generator; DMA: Differential Mobility Analyzer; CPC: Condensation Particle Counter. (b.) Schematic of the nebulizer used to humidify the drift tube counterflow gas. 58

Figure 3.2: DMA-DTIMS Measured normalized arrival time distributions for lithium iodide and sodium iodode particles. The corresponding inverse electrical mobility is shown on the secondary axis for each of the measurements. 63

Figure 3.3: DMA-DTIMS inferred growth factors for (a.) lithium iodide and (b.) sodium iodide nanoparticles, measured at 23.2^{o} C and 24.2 ^{o} C respectively, as a function of the relative humidity of the drift region in the DTIMS. The method for determining the error bars is defined subsequently. 65

Figure 3.4a: Comparison of measured (colored symbols) to theoretically predicted growth factors considering collision rate enhancement factors based on the ion-dipole potential (solid line) and collision rates calculated without potential interaction influences (dashed line). 79

Figure 3.5: The arrival time standard error (symbols) for simulated DTIMS measurements and GF standard error (lines) as a function of $\Delta N_{peak}/\Delta log_{10}t$. Circles represent 150 bins per scan and triangles represent 240 bins/scan. Black symbols, peak arrival time of 1.5s; white: 2.5s; gray: 3.5s. The solid black line represents GF=1, the dashed line is GF=1.1, and the solid gray line is GF=2. For the GF error, the value used for t_0=2.5s..... 85

Figure 4.1: DMA-MS Experimental Comnfiguration. 91

Figure 4.2:Contour plots showing DMA-MS spectra for a) dry conditions and b) at a saturation ratio of 0.65. 95

Figure 4.3: Cluster structures found via density functional theory calculations with g sorbed vapor molecules. Water molecules are represented by the red and white atoms and the Iodine is represented with green atoms. 99

Figure 4.4: Ratio of collision cross sections found by orientation averaged projected area measurements of the simulated cluster structures. Circles represent simulated structures. Line segments between these structures are generated by linear interpolation. Beyond the largest modeled structure the CCS ratio is determined geometrically using the volume of a water molecule. 101

Figure 4.5: Raw measured data for select clusters with *n* neutral pairs of 2, 3, 4, 6, and 9. All data were taken at gas temperature of ~ 27° C. Ions with greater numbers of neutral pairs were not detected at the highest saturation ratios..... 102

Figure 4.6:: Comparison of measurements to model results. Measured results are shown as data points, the KTR model results using the corresponding colored lines. The dotted lines represent $\Delta E = -1x10^{-21}$ and the dashed lines represent $\Delta E = -1x10^{-20}$ 105

Chapter 1 Introduction

1.1 Motivation

In an aerosol (defined as suspended solid or liquid particles in a gas), particles undergo collisions with the background gas molecules at a rate dependent on the particle size, molecular concentration and mass, and the gas temperature. For air molecules these collisions lead to momentum transfer but not mass transfer. For vapor molecules in the gas (defined as a material that is found in the condensed phase at ambient temperatures) these collisions may lead to uptake of vapor molecules by the particle (sorption). If the particle contains material other than the vapor composition this is referred to as heterogeneous vapor uptake. In equilibrium, the rate at which vapor molecules are sorbed by the particle is equal to the rate at which the vapor molecules are desorbed. Under these conditions, there exists a probability distribution function for the number of vapor molecules associated with a particle at any given moment. This distribution varies with the number concentration of the vapor molecules, the collision rates between vapor molecules and particles, sorption energy, and temperature. The degree of vapor uptake at a given vapor concentration can be quantified using techniques that measure a property of the particle that is dependent on the amount of sorbed vapor (e.g. diameter or mass) or by directly measuring the distribution (High Pressure Mass Spectrometry [8-9]). The operating ranges for HPMS as well as existing widely used techniques used to measure equilibrium vapor uptake by aerosol particles are shown in Figure 1.1. Tandem

Differential Mobility Analysis (TDMA) measures the change in the electrical mobility of a particle which is a function of the particle diameter [13] and Electrodynamic Balance (EDB)[14-15] measures the change in particle mass. The limiting factor for TDMA measurements is the reduction in instrument resolution with decreasing size[19-20] whereas the limitation for EDB is that the particles must be able to be optically detected. Evident in Figure 1.1, there is gap in the particle size range and relative humidity that can be measured with these established systems and new methods must be developed to explore vapor uptake by particles in this region. Specialized high resolution DMAs are able to achieve resolving powers greater than 50 for particle sizes down to a single molecule. In principle, with the development of a sampling, humidification, and detection system these devices could be utilized to expand the range of conventional TDMA measurements, although low particle transport efficiencies could be problematic. Drift Tube Ion Mobility Spectrometers (DTIMS) are capable of high resolution measurements for small particles and use reasonably low drift gas flows[1]. The use of a high resolution DMA[2] coupled to a DTIMS is a promising approach although DTIMS devices have several limitations that must be addressed before they can be used with aerosols.

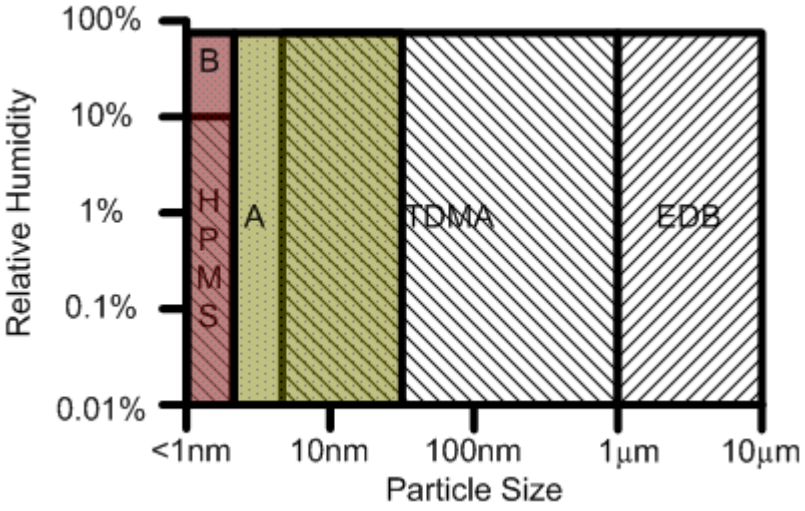

Figure 1.1: Operating ranges for existing instrumentation are shown in the hashed areas where TDMA = Tandem Differential Mobility Analysis, EDB = Electrodynamis balance, and HPMS = High Pressure Mass Spectrometry. Region A, shown in green, is the operating range for the high resolution DMA – Drift Tube Ion Mobility Spectrometer system. Region B, shown in red, is the high resolution differential mobility analyzer – mass spectrometer system.

The objective of this research is to develop new methods for measuring vapor uptake by aerosol particles ranging from dry particles consisting of single molecules up to particles several nanometers in diameter and to develop a method to predict particle growth using discreet values for the change in Gibbs free energy upon the addition of each vapor molecule.. In this work we describe two new measurement systems: System A: a tandem High Resolution DMA - Drift Tube Ion Mobility Spectrometer (HRDMA-DTIMS) for the study of vapor uptake by particles in the size range of 2nm to 20nm and System B: a High Resolution DMA in tandem with a high resolution time of flight Mass Spectrometer (HRDMA-MS) to study water uptake by electrospray generated molecular clusters of known composition. The operating ranges for these new systems are also shown in Figure 1.1.

1.2 Summary of Dissertation

The work described in this thesis consists of two main sections. The first section (Chapter 2- Chapter 3) describes the development of new instrumentation and a measurement technique for charged particles in the size range of 2-11 nm using a High Resolution DMA in tandem with a Drift Tube Ion Mobility Spectrometer (DMA-DTIMS). The second section (Chapter 4) describes a measurement technique applicable to charged particle sizes ranging from single molecules to about 1.5 nm using a High Resolution Differential Mobility Analyzer in tandem with a Mass Spectrometer (HRDMA-MS).

Chapter 2: Design of a DTIMS for use with aerosol particles

This chapter describes the design of a drift tube ion mobility spectrometer designed specifically for measurement of the electrical mobility of aerosol particles including the design of a sampling system which overcomes the limitation of traditional drift tube devices for sampling pre-charged particles. The ability to sample charged particles is essential when charged particles flow into the DTIMS downstream of a DMA. The chapter also describes the design of an interface to a high sensitivity condensation particle counter (CPC), which replaces the electrometers commonly used with drift tube ion mobility spectrometry. Results from fluid flow and electrostatic computational models along with computational results for the arrival time probability distributions of particles with a known mobility are also provided. These results are compared to measured values.

Chapter 3: Measurement of water vapor uptake by small particles using HRDMA-DTIMS

This chapter describes a technique for measuring heterogeneous vapor uptake by small particles using a DTIMS downstream of a High Resolution Differential Mobility Analyzer (HRDMA). The chapter then presents results from water uptake measurements of particles composed of salts with low water activity (LiI and NaI). Also described is a method for estimating the amount of particle growth using discrete equilibrium constants the addition of each vapor molecule.

Chapter 4: Measurement of water vapor uptake by small particles using HRDMA-DTIMS

This chapter provides a description of the HRDMA-MS system, including its principle of operation, experimental methods, and data analysis methods. Also presented are the results of experiments revealing of the extent water vapor sorption by clusters of the structure $X^+(XI)_n$, where *X* represents Sodium, Potassium, Rubidium, or Cesium and *n* ranges from 0 to 13. The results are presented in terms in changes in the collision cross section of individual core ions as a function of relative humidity.

Further described is how the measured shift in collision cross section is linked to equilibrium binding coefficients for the successive uptake of water molecules, and the collision cross sections of ions of the structure $(XI)_nX^+*(H_2O)_m$. Measured shifts in collision cross section are compared to theoretical predictions based upon classical

heterogeneous uptake theories as well as the collision cross sections of density functional theory inferred structures of water bound clusters.

Chapter 5: Conclusions and Future Work

This chapter summarizes the work presented in this dissertation and proposes future development work.

Appendix A: Description of Software

This chapter describes in detail how to perform the numerical simulations referenced in this work as well as the programs used to acquire and analyze data. Specific instructions are provided for creating a model within Fluent and applying a user defined function to find the electrostatic gradients. The chapter also describes the algorithms used to simulate particle trajectories. Lastly the LabVIEW data acquisition program and the accompanying Excel template for gathering and analyzing data are described.

Chapter 2 Mobility Analysis of 2 nm to 11 nm Aerosol Particles with an Aspirating Drift Tube Ion Mobility Spectrometer

2.1 Introduction

Differential mobility analyzers (DMAs) [3-5], as well as a number of other recently developed devices [6-10], can be categorized as spatial electrical mobility spectrometers, as these instruments separate continuously sampled particles in electrical mobility by directing them along mobility dependent trajectories (mobility separation in space). Because the residence time of transmitted particles in a DMA is fixed and independent of particle size, diffusional broadening leads to degradation of instrument resolution for sub 20 nm particles [11-13]. Furthermore, instruments that use DMAs to obtain information about particle size or size distributions, such as tandem differential mobility analyzers and scanning mobility particle spectrometers, typically require several minutes to complete voltage scans [14]. This limits information that can be obtained when aerosols are varying rapidly, such as can occur during sampling with an aircraft or near roadways.

Electrical mobility spectrometry is likewise used for the detection of gas phase ions (referred to as ion mobility spectrometry in this circumstance), which consist of <1000 atoms and have mobility equivalent diameters < 2 nm [15-16]. In contrast to aerosol particle analysis, electrical mobility based analyses for ions are frequently carried out with drift tubes, in which ions, sampled at a specific time, migrate across an electrostatic gradient towards a detector, and the electrical mobility of an ion is inversely

proportional to its transit time through the drift tube (mobility separation in time). DTIMS instruments do not need to be scanned in operational parameters to measure ions with a range of electrical mobilities, as all measured entities migrate along similar trajectories towards the detector. Unsteady size/mobility distributions can be examined via DTIMS, even those which vary on timescale faster than the ion/particle drift times. Because transit time within a drift tube is inversely proportional to the diffusion coefficient of a charged particle [17], instrument resolution is additionally independent of particle size in an ideal drift tube [18]. Moreover, to access the electrical mobilities of nanometer sized particles with modest to high resolution (>20), DMAs require high sheath gas flows, which pose operational difficulties in maintaining laminar and steady flow [19] and necessitate the use of electrical mobility standards for sheath flow calibration [20-21]. With these limitations DMAs rarely have resolving powers in excess of 50 [22]; free of such restrictions, current state-of-the-art DTIMS systems can attain resolving powers well in excess of this value [23].

However, the application of DTIMS for measurements of aerosol particles > 2.0 nm in size remains unexplored, because of several limitations in current instrument designs. First, many DTIMS systems operate at reduced pressure (several Torr) and require that analytes (vapor phase species or particles) are ionized within the inlet region at high potential. Existing DTIMS systems are hence incapable of sampling charged species from atmospheric pressure environments at or near ground potential without substantial electrostatic particle deposition. Second, DTIMS instruments commonly employ low sensitivity, fast response Faraday plate detectors internal to their drift regions

and cannot be readily coupled with aspirating, single particle detectors (i.e. condensation particle counters, CPCs), leading to the requirement that analyte concentrations be in excess of those commonly encountered in aerosols. Third, drift times in existing DTIMS systems are on the order of milliseconds, which is significantly faster than the response time of any existing CPC [24]. Therefore, even if an existing DTIMS instrument was modified to couple with an aspirating detector, CPC response times would prohibit measurement.

The advantages of DTIMS suggest that a suitable DTIMS instrument for aerosol analysis would find application in a number of instances (e.g. determination of size distribution functions in turbulent flows). We have hence constructed a prototype DTIMS instrument which overcomes the aforementioned obstacles in implementation for aerosol particles. In the subsequent sections, the design of the prototype DTIMS instrument is described in detail, as are measurements of DMA-classified aerosol particles with the prototype instrument coupled to a CPC. Analytical models and a combined Eulerian-Lagrangian simulation approach are used to predict particle transport through the instrument, and are compared to measurements. We show that with the prototype DTIMS device, it is possible to analyze particles in the 2.2 – 11.1 nm size range with measurement times ranging from 15 seconds down to subsecond scales (with longer times and larger sizes are also analyzable).

2.2 Experimental and Theoretical Methods

2.2.1 *DTIMS Prototype Overview*

A labeled schematic of the prototype DTIMS is shown in Figure 2.1a (cross-sectional view), with a rendered cutaway image shown in Figure 2.1b. Calculated flow streamlines at the inlet and outlet (with calculations described subsequently), are depicted in Figure 2.2a and 2.2b, respectively. Lines of isopotential (electrostatic), formed when voltage is applied for measurement, are also shown in Figure 2.2a & 2.2b, as well as in Figure 2.2c for the entire device. We concurrently refer to Figure 2.1a-b and Figure 2.2a-c in providing a general description of the DTIMS prototype manner of operation.

During operation, aerosol is continuously directed into the "sample inlet". The entire device is held at ground potential prior to the start of each measurement, and any particles entering the device follow the indicated "sample inlet streamlines", i.e. entering particles traverse the "approximate sample volume", and are then transported to the "excess outlet". Particles do not traverse the "drift region" under these circumstances, as an additional flow, sent continuously into the device at the "counterflow inlet", passes through the drift region from outlet to the inlet. The inlet of the DTIMS can therefore be described as a fluid-mechanical gate, which is distinct from the electrostatic gating schemes employed in conventional DTIMS instruments [25].

The "drift region" is a cylindrical tube consisting of a series of ring electrodes. Connected to the first ring electrode is a conducting mesh screen (labeled in Figure 2.1a); sample inlet streamlines pass through this mesh screen both as they enter the device, and as they leave through the excess outlet. To begin a measurement, voltage is applied to

the 1st ring electrode and the mesh screen (noted as the "location of maximum potential" in Figure 2.2a), and the voltage decreases nearly linearly from electrode to electrode, leading to the electrostatic isopotential lines in Figure 2.2c. The trajectories of uncharged particles, both those that have already entered the "sample inlet" and those entering after the voltage is applied, are unchanged, and they continue to exit through the "excess outlet". The sample inlet remains grounded at all times. Therefore, particles charged to the opposite polarity of the applied voltage, irrespective of whether they enter the device before or after the voltage is applied, are directed electrostatically towards the mesh screen. Conversely, particles charged with the same polarity as the applied voltage are transported in a manner dependent upon whether they enter the device prior to voltage application (and are to the right "location of maximum potential" in Figure 2.2a) or after voltage is applied. In the latter instance, the electrostatic potential gradient between the mesh screen and sample inlet tube directs these particles onto the sample inlet tube. In the former instance, an electrostatic force directs particles axially across the drift region. If a particle's resulting electrophoretic velocity (the product of its electrical mobility and the axial electrical field strength) is greater than the velocity of the counterflow in the drift region, the particle will traverse the drift tube, with the time required to traverse the drift region (i.e. the drift time) a function of the particle's electrical mobility, Z_p. Upon traversing the drift region, particles near the center of the drift region tube are driven by fluid flow to the detector (along the "flow to detector streamlines"), where the detector (a CPC) aspirates flow out of the drift region. Particles at outer radial locations deposit diffusively and electrostatically on the device outer walls. Additional time is required for

particles to be detected, yet provided that the response time distribution of the detector is sufficiently narrow relative to the particle drift time (the time required for a particle to traverse the drift region), then the time at which a particle is detected (with zero time defined as the instant at which the voltage is first applied) is primarily a function of the electrical mobility of the particle.

We note that with a DTIMS instrument operated as described, at no point are measured particles required to travel “upstream” across electrostatic gradients, and that charged particles may be directly sampled from ground potential, atmospheric pressure aerosols. Particles which traverse the drift region once voltage is applied are considered to be part of the sample volume for each measurement. Although the actual size of the sample volume is electrical mobility dependent and difficult to quantify, with sufficiently small sample volumes DTIMS instruments are capable of substantially higher time resolution measurement than their spatial mobility filter counterparts, with the time resolution related to the time required to fill the sample volume.

a)

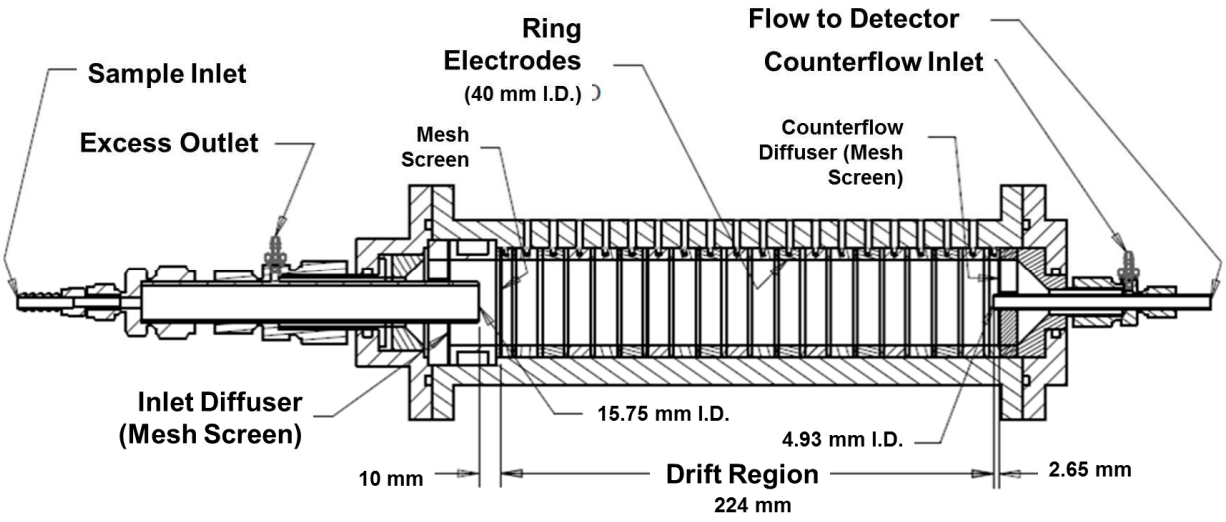

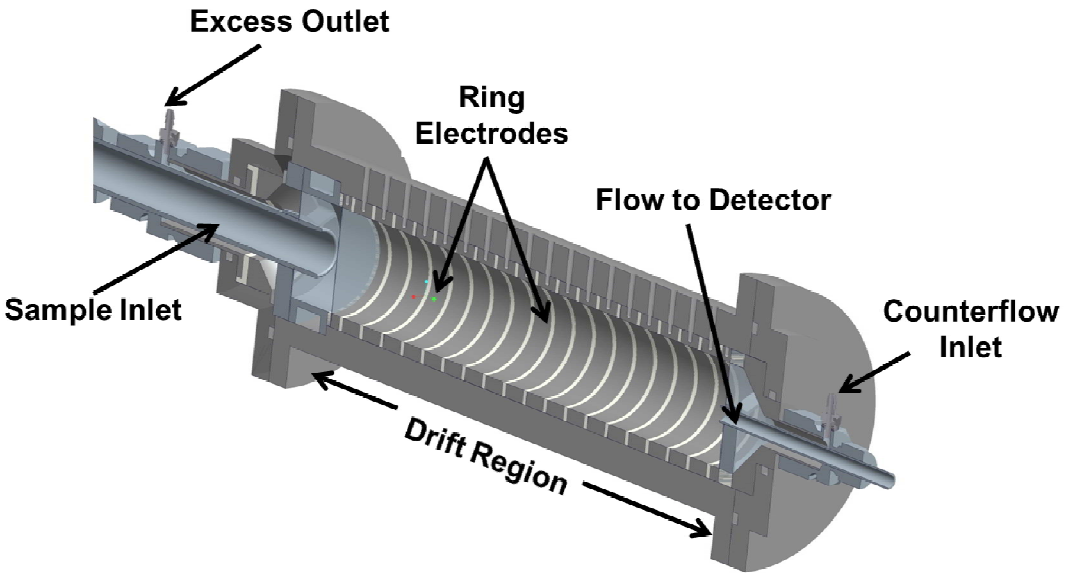

b)

Figure 2.1 a) Schematic of the DTIMS prototype. b) A three dimensional cutaway image of the DTIMS prototype

a)

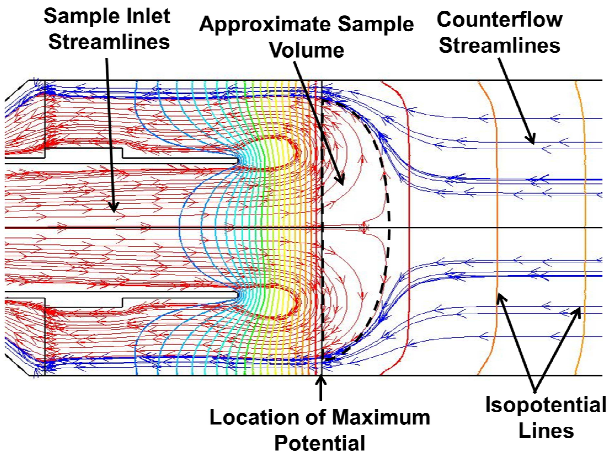

b)

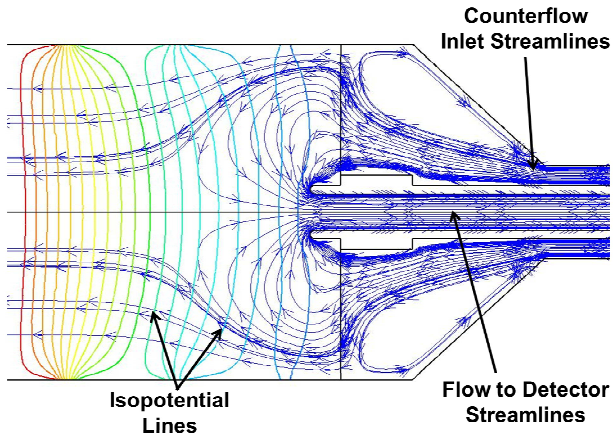

c)

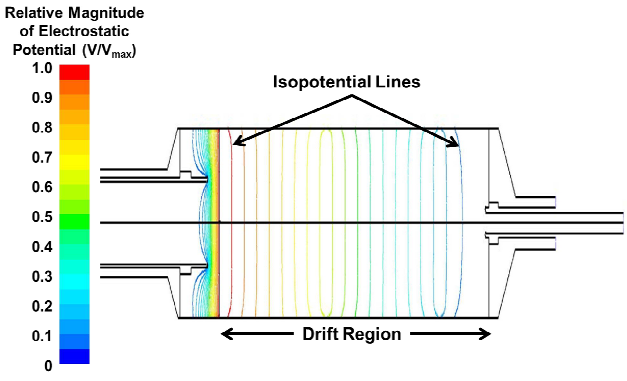

Figure 2.2: Depictions of (a.) the streamlines and isopotential lines at the DTIMS prototype inlet formed by the sample inlet flow and counterflow, (b.) the streamlines and isopotential lines formed by the counterflow at the prototype outlet, and (c.) relative isopotential lines (V/Vmax, where Vmax is the applied voltage) in the drift region.

2.2.2 *DTIMS Prototype Design*

A number of DTIMS systems can be designed which operate in the aforementioned manner to separate particles of disparate electrical mobilities from one another. The dimensions of the prototype DTIMS device presented here are provided in Figure 2.1a. Measurements are carried out with a counterflow inlet air flowrate of 0.815 l min^{-1}, and a CPC detector flowrate of 0.615 l min^{-1} (Figure 2.1a and Figure 2.2b). Air is hence transported across the drift region (from outlet to inlet) at a net flowrate of 0.2 l min^{-1}. The excess outlet flow is regulated at 1.0 l min^{-1}, which results in a sample inlet flowrate of 0.8 l min^{-1} (excess outlet flowrate = sample inlet flowrate + counterflowrate). The cylindrical tube defining the drift region is made of nonconductive polycarbonate plastic, in which 20 stainless steel ring electrodes are fixed. The electrodes themselves are ~10 mm in width with ~2 mm wide insulating spacers between electrodes. Connected to the first electrode is a stainless mesh screen (15 x 15 wire mesh, 0.01" diameter wires, covering the entirety of the drift region cross section), which the sample flow traverses prior to exiting through the excess outlet. A voltage in the range 1 kV to 9 kV is applied to the first electrode, while the last electrode is held at ground during measurement. A chain of equivalent value resistors (600 kΩ for all but the final three electrodes) connects all electrodes to their immediate neighbors, creating a near constant axial electric field in the drift region, as depicted in Figure 2.2c. A slight non-linearity in the voltage profile is present at the end of the drift region; the final three electrodes are connected by two resistors of lower resistance than those prior (300kΩ and 150kΩ, respectively). This causes a radial electric field to develop at the outlet, an effect which is expanded upon

and discussed subsequently. After particles pass through the sample outlet tube, they arrive at the detector, which is a water based condensation particle counter for the present setup (TSI model 3788 or 3786 [26-28]).

2.2.3 *DTIMS Arrival Time Distribution Measurements*

In DTIMS, measurements are quantified via arrival time distributions (ATDs), i.e. the signal (number of particles, when using a CPC) per unit measurement time (adjustable to per unit log time, as is used in this study) as a function of measurement time. The performance of the prototype DTIMS was tested by measuring the ATDs of DMA classified particles. A schematic of the system used for the tandem DMA-DTIMS experiments is provided in (Figure 2.3).

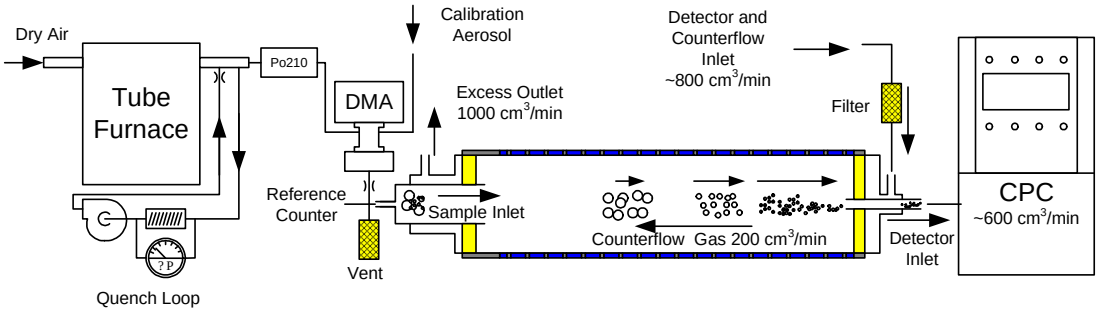

Figure 2.3: Schematic of the system used for NaCl particle generation, DMA based electrical mobility section, and DTIMS electrical mobility analysis

The test aerosol was generated using a tube furnace generator (Lindberg Blue) as described by Scheibel & Porstendorfer [29] with sodium chloride as the particle material. The supply gas flowrates for the furnace ranged from 3 to 5 l min^{-1} and the set furnace temperature was ~645°C. The particle electrical mobility (diameter) window was selected using a high resolution DMA (Nano-Engineering Corp., the half-mini DMA [4]) operated in recirculating mode with a resolving power, R≈36 (determined using an

electrospray generated mono-mobile calibration ion, tetradodecylammonium^{+} [20]). The calibration ion was also used to determine the DMA voltage/mobility relationship and was measured at the beginning and end of each experiment. The DMA sheath flow was controlled using a blower in a closed loop configuration (Domel D.D., Slovenia). The sheath temperature was controlled using an air-to-water heat exchanger coupled to a laboratory chiller. An orifice was placed downstream of the DMA to insure that the aerosol was well mixed prior to branching the flow into the DTIMS prototype, a reference counter to monitor the inlet concentration, and an excess aerosol vent to a filter. The "detector and counterflow gas flow rate" is approximate and was adjusted to maintain a counterflow of 200 cm^3 min^{-1}. For comparison to models, the size distribution function at the DMA outlet/DTIMS instrument inlet was approximated as a Gaussian distribution using the measured resolving power of 36.

At the start of a measurement the DTIMS voltage (either 1 kV, 3 kV, or 9 kV, facilitating the migration of positively charged particles) was applied to the first electrode using a high voltage power supply (Bertan high voltage) and relay (Cynergy 3 Components ltd.), which was switched via a data acquisition module controlled using *Labview* software (*National Instruments*). The software counts the number of digital pulses sent by the detector, which indicate detected particles, and assigns them to a time interval based on the delay between onset of the relay and the detection of the pulses. The software further facilitates the collection of multiple ATDs, which were exported and later averaged. 150 bins in time were used to define ATDs. For the test results presented in this work the number of measurements was varied from 3 to 10 with higher numbers of

scans chosen for lower input concentrations. Multiple measurements were employed primarily to ensure repeatability; under most operating conditions particle concentrations at the DMA outlet were high enough to allow for sufficient signal-to-noise during collection of a single ATD.

2.2.4 *Predictions of Arrival Time Distributions & Simulation of Particle Trajectories*

For comparison to experimental measurements, we examine DTIMS measurements via both an analytical based simulaitons and numerical simulations. In the analytical model we define $d\tilde{N}$ as the number (not number concentration) of particles with diameter between d_p and $d_p + dd_p$ contained in volume element dv within the sampling volume, V_s. Integrating over the sampling volume, it follows that the number distribution of all particles in the sampling volume is:

$$\tilde{n} = \frac{d\tilde{N}}{dd_p} = \int_{V_s} \frac{d\tilde{N}}{dd_p dv} dv \tag{2.1a}$$

The sample volume V_s likely varies with particle size, and particles of a given size are probably not uniformly distributed within V_s. Quantifying the relationship between measured ATDs and the size-resolved number concentrations of the sampled aerosol would require an understanding of how particles of a given size are distributed within V_s as well as a detailed understanding of size-dependent transport efficiencies, which is beyond the scope of this work. Therefore, our analysis focuses on measurements of size and not concentration.

It follows that the number of particles carrying q charges and having diameter in the range d_p to d_p+dd_p is $f_{q,d_p}\tilde{n}\cdot dd_p$, and in the absence of any particle depositional losses, the number of these particles traversing the drift tube between time t_{drift} and t_{drift}+dt_{drift} is: $f_{q,d_p}\tilde{n}\cdot dd_p\Theta_{IMS}\left(Z_p,t_{drift}\right)dt_{drift}$. Correspondingly, the number of these particles which are transmitted and detected when considering depositional losses (and the detector efficiency) is: $f_{q,d_p}\tilde{n}\cdot dd_p\Theta_{IMS}\left(Z_p,t_{drift}\right)dt_{drift}\eta_T\eta_A\eta_{Det}$.

Particles that traverse the drift tube enter the detector inlet. The time at which a particle is detected, t, equals the sum of the drift time and the detection time: i.e., $t_{det} = t - t_{drift}$. The total number of these particles detected per unit detection time (dN_p/dt) is:

$$\frac{dN_p\left(d_p,q,t,t_{drift}\right)}{dt}=\tilde{n}(d_p)dd_p f_{q,d_p}\eta_T\eta_A\eta_{Det}\Theta_{IMS}\left(Z_p,t_{drift}\right)dt_{drift}\Phi(t-t_{drift}) \tag{2.1b}$$

The left side of Equation (2.2b) has dt substituted in the denominator, as for a specified drift time $dt = dt_{det}$. Equation (2.1a) only considers particles within a narrow diameter range, and with a specified charge level. The number of particles detected per unit measurement time at measurement time t, traversing the drift tube within the specified range, but considering the entire particle size distribution function and all possible charge levels, is:

$$\frac{dN_p\left(t,t_{drift}\right)}{dt}=\left(dt_{drift}\sum_{q=1}^{q=\infty}\left[\int_0^\infty\eta_T\eta_A\eta_{Det}f_{q,d_p}\Theta_{IMS}\left(Z_p,t_{drift}\right)\tilde{n}(d_p)\cdot dd_p\right]\right)\Phi(t-t_{drift}) \tag{2.1c}$$

The sum over values of q is used in lieu of an integral because q only takes integer values. Positive values of q only are considered since, when a positive voltage is applied to the ring electrodes and mesh screen, negatively charged particles are not transported to

the detector. Finally, the *ATD(t)* is calculated for a given total measurement time *t* by accounting for the contribution of all particles detected for all possible drift times less than or equal to *t*:

$$ADT(t) = \int_0^t \left(\sum_{q=1}^{q=\infty} \int_0^{\infty} \eta_T \eta_A \eta_{Det} f_{q,d_p} \Theta_{IMS}\left(Z_p, t_{drift}\right) \tilde{n}(d_p)\, \Phi(t - t_{drift}) dd_p \right) dt_{drift} \quad (2.1d)$$

For prescribed DTIMS operating conditions (flowrates and voltage) the ATD (for positively charged particles) can be approximated as:

$$ATD(t) = \int_0^t \left[\Gamma\left(t_{drift}\right) \Phi\left(t_{\det}\right) \right] dt_{drift} = \int_0^t \left[\Gamma\left(t_{drift}\right) \Phi\left(t - t_{drift}\right) \right] dt_{drift} \quad (2.2a)$$

$$\Gamma\left(t_{drift}\right) = \sum_{q=1}^{q=\infty} \left[\int_0^{\infty} \eta_T \eta_A \eta_{Det} f_{q,d_p} \Theta_{IMS}\left(Z_p, t_{drift}\right) \tilde{n}\, dd_p \right] \quad (2.2b)$$

$$\Phi\left(t_{\det}\right) = \frac{df_{\det}}{dt_{\det}} \quad (2.2c)$$

where *t* is the total measurement (arrival) time, t_{drift} is the time required for a particle to traverse the drift tube, and t_{det} is the time required for a particle, having exited the drift region, to be detected. A detected particle only contributes to the ATD at an arrival time equal to sum of its drift time and detection time; hence $t_{det} = t - t_{drift}$. Equation (2.2a) expresses the ATD as a convolution integral over the product of two near-independent functions: the first, $\Gamma(t_{drift})$, dependent upon the time for particles to traverse the drift tube (t_{drift}) and representing the ATD of a DTIMS device with a perfect detector (i.e., a detector that responds at the same instant to all particles with a given t_{drift}), and the second, $\Phi(t_{\det}) = \frac{df_{\det}}{dt_{\det}}$, the probability distribution function for the detector response

times (i.e., $\Phi(t_{\det})dt_{\det}$ is the fraction of particles between $t_{\det}$ and $t_{\det}+dt_{\det}$ after they flow into the detector inlet at the exit from the drift tube). In $\Gamma(t_{drift})$, $\tilde{n}\ dd_p$ is the number of particles in the sample volume with sizes between d_p and $d_p + dd_p$ in the sampling volume (see Figure 2.2a), and $f_{q,dp}$ is the (dimensionless) fraction of particles of diameter d_p that have integer charge level q. $f_{q,dp}$ must be known *a priori* [30-31], and for a given set of background gas conditions (temperature, pressure, and composition) the electrical mobility of a particle is defined exactly by its diameter and integer charge level from the Stokes-Millikan equation:

$$Z_p = \frac{qe}{3\pi\mu\left(d_p + d_g\right)}\left(1+\frac{2\lambda}{\left(d_p+d_g\right)}\left(1.257+0.4\exp\left[-\frac{0.55\left(d_p+d_g\right)}{\lambda}\right]\right)\right) \qquad (2.2d)$$

where e is the unit electron charge, λ is the gas mean free path, d_g is the effective gas molecule diameter (0.3 nm in air near room temperature [32]), and μ is the gas dynamic viscosity. η_T, η_A, and η_{Det} are the transmission efficiencies of the sample inlet and drift region, drift region outlet and aspirating detector inlet, and the detector itself, respectively. These transport efficiencies are governed by particle deposition due to both diffusion and electrostatic precipitation at the counterflow screen, though we neglect electrostatic effects in the analytical model. $\Theta_{IMS}\left(Z_p, t_{drift}\right)$ is the ideal drift time probability distribution function [18], i.e. $\Theta_{IMS}\left(Z_p, t_{drift}\right)dt_{drift}$ is the fraction of particles in the sampling volume with electrical mobility Z_p, and with drift times from t_{drift} to t_{drift} + dt_{drift}, assuming negligible particle depositional loss during migration.

The transmission efficiency into the drift region, η_T, is approximated as the product of the penetration of particles through a wire mesh screen [33] and through the sample inlet tube [34]. Particle losses in the drift region are not considered in the analytical model as there is a complex relationship between electrostatic deposition and particle residence time. The transmission of particles through the mesh screen (part of η_T) is calculated with the equation developed by Cheng & Yeh [33]:

$$\eta_{Mesh} = \exp\left(\frac{-10.8\alpha_s h_m \left(\frac{U_f d_f ze}{Z_p kT} \right)^{-2/3}}{\pi(1-\alpha_s) d_f} \right) \tag{2.3a}$$

where α_s is the solid fraction of the wire mesh (calculable using the specifications provided in the main text), h_m is the effective mesh thickness (approximated as twice the wire diameter), and U_f is the free stream velocity (upstream of the mesh). In numerical simulations, particles are additionally deposited on the mesh screen by calculating η_{Mesh} for each particle encountering it, and then depositing the particle in question if a random number chosen from a uniform distribution between 0 and 1 is less than η_{Mesh}.

Similar to the sampling inlet tube, the transmission efficiency through drift region outlet and aspirating detector inlet, η_A, can be approximated with the Gormley & Kennedy equations [34],

$$\eta_{tubing} = 1 - 2.56\gamma^{2/3} + 1.2\gamma + 0.1767\gamma^{4/3} \qquad \gamma < 0.02 \tag{2.3b}$$

$$\eta_{tubing} = 0.819e^{-3.66\gamma} + 0.0975e^{-22.3\gamma} + .0325e^{-57.0\gamma} \qquad \gamma \geq 0.02 \tag{2.3c}$$

where $\gamma = \frac{\pi k_B T Z_P L_{tube}}{Qze}$, Q is the volumetric flowrate through the tube under examination, and L_{tube} is the tube length. The diffusion losses to tubing were only considered for the inlet region leading up to the wire mesh (part of η_T) and the sample exit tube (η_A). Diffusion losses in the drift region were not accounted for in the analytical model. For calculations we neglect size dependencies in the detector efficiency, η_{Det}, setting η_{Det} = 1.0 under all circumstances..

The condensation particle counter response time distribution function neglecting the influence of tubing between the drift region outlet and the CPC (which is incorporated into the analytical model as is noted previously), was determined as follows: As is depicted in Figure 2.4, a flow of aerosol first passed through an electrostatic precipitator and subsequently enters the CPC. A *Labview* software program (*National Instruments*) was used to control both the high voltage relay to the electrostatic precipitator as well as to monitor the particle counts detected by the condensation particle counter. During non-measurement periods, voltage was applied to the electrostatic precipitator continuously, such that no particles entered the detector. At the start of the measurement ($t_{det}=0$), the precipitator electrode was grounded and the particle counts relative to this instant were collected. This enabled determination of the cumulative arrival time distribution function for particles. The probability distribution function, df_{det}/dt_{det}, was subsequently inferred from the slope of the cumulative distribution function, and is displayed in Figure 2.5 for WCPC models 3788 & 3786. The resulting peak response times for the WCPC 3788 and

WCPC 3786 are 280 and 850 milleseconds and the resulting measured FWHM values are 50 and 210 milleseconds respectively.

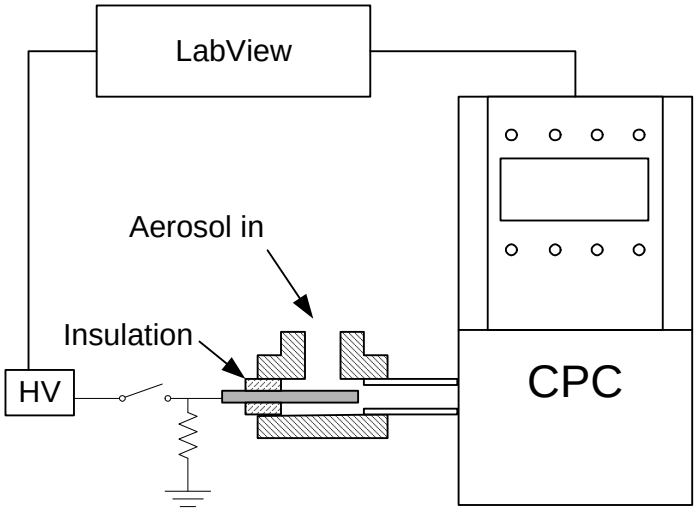

Figure 2.4: Schematic of the system used for CPC response time distribution determination.

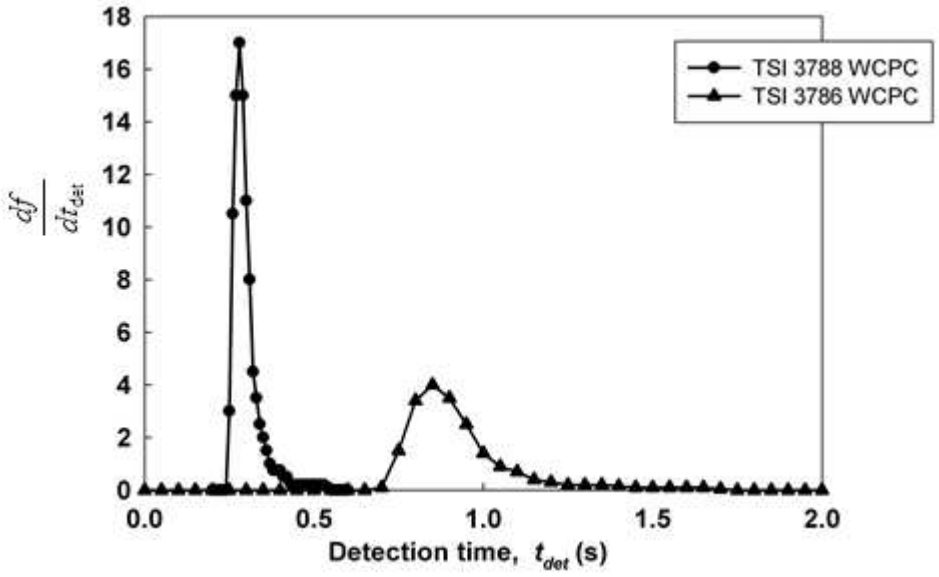

Figure 2.5: The normalized response time distribution functions, $\frac{df}{dt_{\det}}$, as measured with the system shown in Figure 2.4, for the CPCs used in this work..

To develop an expression for $\Theta_{IMS}(Z_p, t_{drift})$, we note that with negligible counterflow in the drift region, the square of the full width at half-maximum (FWHM) of the drift time distribution for an ideal DTIMS instrument, $(\Delta t_{drift})^2$, is given by Revercomb & Mason (1975) as:

$$(\Delta t_{drift})^2 = (\Delta t_0)^2 + \frac{16\ln(2)t_{ave}^2}{\Psi_E} \tag{2.4a}$$

where Δt_0 is the half width of the input pulse (determined by the axial length of the sample packet, as indicated in Figure 2.2a), Ψ_E is the electrical potential energy to thermal energy ratio [35] for the drift tube, defined as qeV/k_BT (where qe is the particle charge, V is the applied voltage, k_B is Boltzmann's constant and T is the gas temperature), and t_{ave} is the average ideal drift time ($L*L_E / Z_pV$, where L is the drift region length, and $L_E = 22.7$ *cm* is electrode to electrode distance defining the electric field). The value for Δt_0 is related to the axial length of the sample volume, indicated in Figure 2.2a (Δx), through the equation:

$$\Delta t_0 = \frac{\Delta x L_E}{Z_p V}. \tag{2.4b}$$

We estimate $\Delta x \approx 0.8$ cm and correspondingly assume $L = 22$ *cm* (the average length of drift region considering particles begin migration Δx/2 into the drift tube) for the prototype. Equations (2.4a) & (2.4b) neglect any influence of counterflow. Following the procedure of Revercomb & Mason (1975) with the assumption of simple plug flow acting in the drift region, the square of the FWHM of the drift time distribution becomes:

$$\left(\Delta t_{drift}\right)^2 = \left(\Delta t_0\right)^2 + \frac{16\ln(2)t_{ave}^{\ 2}}{\Psi_E - Pe}. \tag{2.4c}$$

where *Pe* is the Peclet number, defined as $u_cLze/(Z_pkT)$, t_{ave} is redefined as $(L*L_E / [Z_pV-u_cL_E])$, and Δt_0 is similarly modified to $(\Delta xL_E/([Z_pV-u_cL_E]$. Ψ_E, the electrostatic energy to thermal energy ratio, may also be treated as the ratio of a particle's electrophoretic speed to its diffusive speed (i.e. an electrostatic Peclet number [36]), hence the parameter Ψ_E-*Pe* is the net Peclet number for transport through the drift tube and Pe/Ψ_E is the ratio of a particle's advective speed to its electrophoretic speed (equivalent to $u_cL/(Z_pV)$). The resolving power of a DTIMS instrument considering counterflow ($R = t_{ave}/\Delta t_{drift}$) is approximated as:

$$R = \left[\left(\frac{\Delta x}{L}\right)^2 + \frac{16\ln(2)}{\Psi_E - Pe}\right]^{-1/2}. \tag{2.4d}$$

and the probability distribution function for drift times, approximated as a normal distribution, is given by the equation:

$$\Theta_{IMS}\left(Z_p, t_{drift}\right) = \sqrt{\frac{2\ln(2)}{\pi}}\frac{1}{\Delta t_{drift}}\exp\left(-4\ln(2)\left[\frac{t_{drift}}{\Delta t_{drift}} - R\right]^2\right). \tag{2.4e}$$

Equation (2.4d) reveals that a DTIMS instrument's resolving power is limited by the finite width of its sample volume and by particle diffusion, and has a maximum value of $L/\Delta x$ even in the absence of particle diffusion. Analogously, Equation (2.4e) shows that the distribution of drift times becomes narrower as *R* increases.

In analytical based simulaitons, peak normalized ATDs were determined by first randomly selecting a particle of specified electrical mobility (and diameter, assuming

particles are singly charged only) from a distribution of particle sizes, chosen to match those used in experiments. Second, η_T and η_A were determined, and whether the selected particle reached the detector was determined stochastically using the product of these values. If the selected particle did indeed reach the detector, its drift time was randomly selected from the distribution described by Equation (2.4e), with all parameters needed to describe this distribution defined by the particle's electrical mobility and instrument operating conditions. The particle's residence time within the tube (Length = 16.3 cm) connecting the end of the drift region and the CPC inlet was determined stochastically selecting the streamline (neglecting diffusion) on which a particle migrated to the detector. Assuming a fully developed laminar flow profile within the tube, the probability, *P(r)*, of a particle traveling along a streamline at radial location *r*, is given by the equation:

$$P(r) = 4\int_{r}^{r+\Delta r} \frac{r}{A^2}\left[1 - \frac{r}{A^2}\right] dr \tag{2.5}$$

where A is the tube radius, and Δr is a small differential in the radius. The time the particle resided within tubing at the outlet was calculated from the fully developed, laminar flow profile velocity at the radial location selected, and the time to reach the detector after exiting the tubing was subsequently randomly selected from the detector response time distribution function, $\Phi(t_{\text{det}})$. Finally, the contribution of the selected particle to the ATD was determined by placing it into an appropriate time bin based upon the value of $t = t_{drift} + t_{det}$ (where t_{det} is the sum of the time the particle resided within the tube connecting the drift region to the CPC and the sampled detector response time). Normalized ATDs were determined by repeating this procedure for 10^4 particles, dividing

the number of particles in each time bin by the log scale bin width (note $\frac{df}{dt} = \frac{1}{2.303t}\frac{df}{d\log_{10}(t)}$), and then by dividing this value by the total number of detected particles.

While the analytical model based simulation is useful for understanding device performance and to estimate the ATD for a given particle size distribution and $f_{q,dp}$, evaluation of the effects of complexities in the sample volume shape, the size distribution function variation within the sample volume, and the velocity field requires use of a numerical model. Therefore, we also determined particle drift times through a combination of fluid flow and electrostatic field simulations (with *ANSYS® Fluent*) coupled to a *FORTAN* Lagrangian particle tracking model. In calculations the geometry was treated as two dimensional and axi-symmetric, and all flows were laminar; simulations led to the streamlines at the prototype inlet and outlet shown in Figure 2.2a & Figure 2.2b, respectively. Three mesh screens are used in the prototype: in the inlet for the sample flow which affects both the flow and electrostatic field, and in the counterflow and excess flow diffusers (the latter two are both 400 x 400 , 0.001" diameter wire meshes covering the entirety of their respective cross sections). The pressure drop across the screens was calculated as a 'porous jump' within *Fluent*, with the pressure drop (ΔP) across the screen given by:

$$\Delta P = -K\left(\frac{1}{2}\rho U^2\right) \tag{2.6a}$$

where U is the average normal flow speed approaching the mesh. The pressure drop coefficients, K, were calculated using the equations [37]:

$$K = 6.5\,\mathrm{Re}_d^{-1/3}\frac{1-\beta}{\beta},\ \mathrm{Re}_d = \frac{Ud_{wire}\rho}{\beta\mu} \tag{2.6b}$$

where ß is the fractional open area of the mesh, d_{wire} is the mesh wire diameter, μ is the fluid viscosity and ρ is the fluid density. The pressure drop across the screen is modeled as isotropic though the incoming velocity varied spatially along the mesh. Electrostatic fields were calculated by creating a user defined scalar within *ANSYS® Fluent* and then determining the scalar gradients in the radial and axial directions with a user defined function. All of the polycarbonate components were modeled as zero flux surfaces. Voltage boundary conditions were applied to the simulation by creating localized mesh zones near the sample inlet and counterflow inlet screen surfaces, and directly assigning the desired potential to those grid points.

From *ANSYS® Fluent* calculations, velocity vectors and electrostatic field vectors were exported as two-dimensional arrays. Particle trajectories and their associated arrival time distributions were then simulated using the algorithm described by Ermak and Buckholz [38] to solve the equation of motion for test particles of prescribed electrical mobility, where the equation of motion is given as:

$$m_p\frac{d\vec{v}_p}{dt} = ze\vec{E} - \frac{ze}{Z_p}\left(\vec{v}_p - \vec{u}\right) + \vec{X} \tag{2.7}$$

$\vec{E}$ and $\vec{u}$ are the electrostatic field and fluid velocity vector, respectively, at the nearest location to the particle's present location, $\vec{v}_p$ is the particle velocity, and $\vec{X}$ is a random

force vector accounting for particle thermal motion (diffusion). For the conditions of interest (atmospheric pressure, room temperature), particle inertia negligibly influences motion at all locations within the prototype; thus, although the full solution to the equation of motion was used, the mass of the particle, m_p had no bearing on results with realistic values. Details of this algorithm are described in 0. Adaptive timesteps were used in simulations, based on the distance traveled and the particle speed in the prior timestep as well as the distance to the nearest boundary [39]. The particles were stochastically seeded at the inlet (of the sample tube) with a radial weighting to account for volumetric flux, such that the probability, *P(r)*, of a particle being initialized at radial location *r*, is given by Equation (2.5). Sampled particles had electrical mobility and diameters sampled from size distribution functions matching experiments. As the particles traversed the simulation domain they could be removed either by deposition to walls or by deposition to the sample inlet screen (via diffusion) and counterflow screen (via electrostatic precipitation, directly from the simulation). Particles were initiated at random times throughout a defined 'seeding' period, in which the voltage was not applied and electrostatic influences on trajectories were neglected. The seeding procedure was repeated until the average of number concentration of particles in the sample volume region tended to a steady value. Subsequently, the voltage was applied in the simulation, and the trajectories of particles present were then subject to both fluid flow and electrostatic influences. Drift times were determined directly for all monitored particles, and as with the analytical model, each 'detected' particle was then assigned an additional detection time value sampled from the measured detector response time distribution

$\Phi(t_{det})$ and the residence time within the tubing connecting the drift region to the detector. To predict normalized ATDs the binning procedure used for the analytical model was similarly employed with simulation results, though unlike the analytical model, simulations also permitted quantification of DTIMS instrument transmission. In total, for each reported simulation value $\geq 10^4$ particle trajectories were simulated.

Trajectories are shown Figure 2.6 for selected monodisperse singly charged particles and applied voltages. Arrows indicate the direction of particle migration in the figure. Under all conditions particles traverse the drift tube axially against the counterflow, with slight oscillatory radial motion (induced by the presence of insulating rings) apparent for particles initiated near the prototype walls. These particles, however, do not reach the detector inlet tube and are hence not detected. The simulations show that at low Pe/Ψ_E values particles are more likely to deposit on the counterflow screen electrostatically, while at high Pe/Ψ_E values particles are lost in the inlet region due to advection. The influences of both electrostatic and advective motion are quantified subsequently in the discussion of particle transmission through the DTIMS instrument.

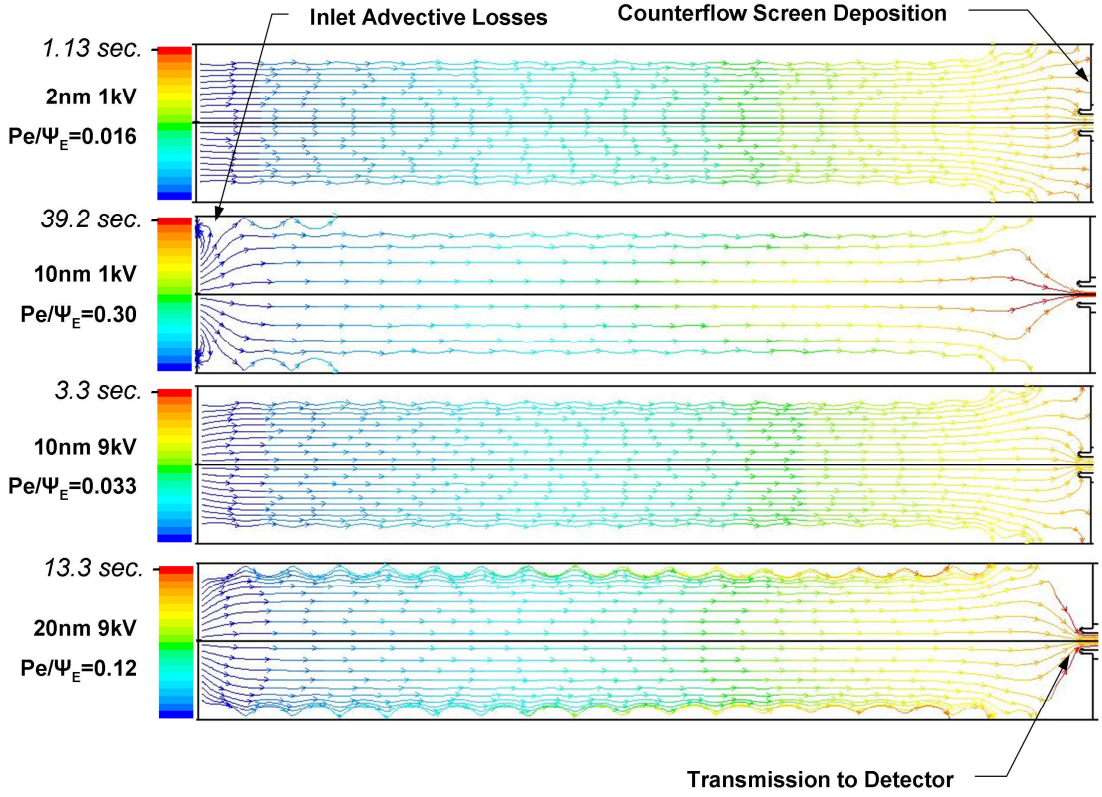

Figure 2.6: Depictions of characteristic particle trajectories through the drift region, for the indicated particle diameters (singly charged) and applied voltage. The colors of particle pathlines are varied with the drift time.

2.3 Results and Discussion

Analytical Model, Numerical Simulation, & Experimental Measurement Comparison

Figure 2.7a-c displays plots of simulated (of both the analytical and numerical based models) and experimentally measured normalized ATDs as a function of measurement time for DMA selected NaCl particle electrical mobility windows, with applied voltages of 1 kV, 3 kV, & 9 kV, respectively. For all displayed results the detector was a TSI model 3788 WCPC, which has a response time distribution peaked below 0.3 s; thus, only in instances where the total measurement time is below ~2.0 s

does the CPC response time substantially influence the distribution. Overall, strong agreement is found between the simulated and measured ATDs, with the peak time in distributions determined by all three methods coinciding (<7%) under nearly all conditions. This demonstrates clearly that not only can the prototype DTIMS instrument be used for the measurement of aerosol particles, but also that the prototype functions within its theoretical bounds. At the same time, however, deviations in peak location and an increased FWHM for experimental ATDs as compared to the calculated distributions are evident, with deviations more pronounced at longer measurement times. We suspect this is due to slight imperfections in flow paths in the prototype device near the mesh screens, which have a more pronounced influence on particles of slower electrophoretic velocities (and hence longer drift times). Evidence supporting this is found with non-axisymmetric (3-dimensional) fluid flow model of the prototype device. However, we elect not to examine this deviation further here in light of the strong agreement between numerically simulated and measured ATDs below 10 seconds (though it is also evident in subsequent examination of instrument resolving power).

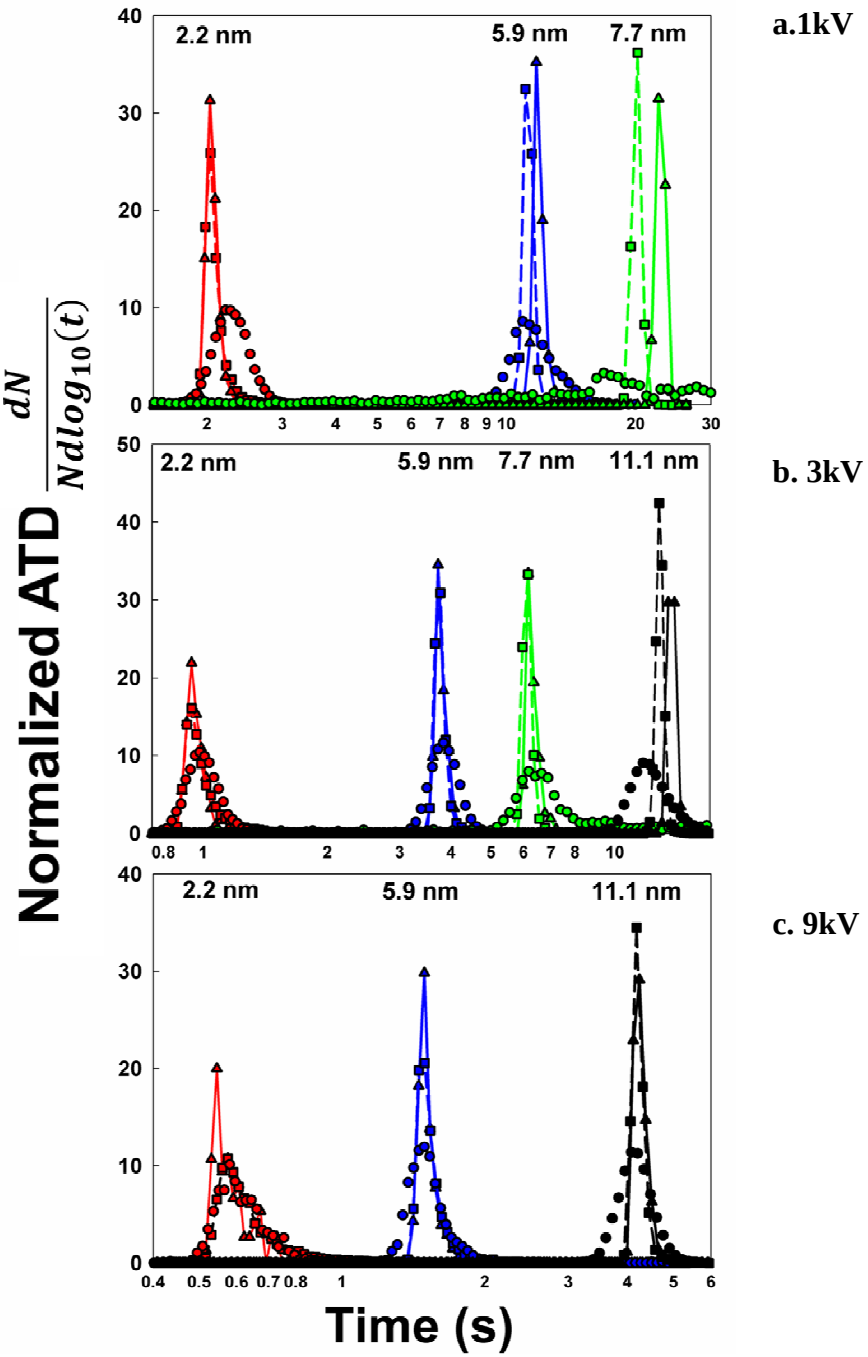

Figure 2.7: Normalized arrival time distributions (*dN*: the number of particles per measurement bin, *N*: the total number of detected particles, $dlog_{10}(t)$: the log-scale bin width) as a function of measurement time, as determined from experiments (circles), numerical based simulations (triangles), and the analytical based simulations (squares). The midpoint particle diameter (singly charged) selected by the upstream DMA is noted near the peak of each distribution.

Figure 2.8a is a plot of the peak measurement time in ATDs as a function of inverse electrical mobility as well as *Pe* for DMA-selected NaCl particles. Curves for 3 different applied voltages, and hence 3 different values of Ψ_E (for singly charged particles) are displayed. A near-linear relationship is expected for this plot provided $\Psi_E >> Pe$. This criterion is approximately valid for all displayed conditions with the lone exception possibly at 1 kV; at the longest measurement time $Pe = 7.31 \times 10^3$ and $\Psi_E = 3.86 \times 10^4$. Correspondingly, for drift times below 10 seconds, the simulated and experimentally measured curves are highly linear, with $R^2 > 0.998$ found via linear regression for all three result sets. When the normalized peak time ($\tau = tu_c/L$) is plotted as function of parameter Pe/Ψ_E, as is shown in Figure 2.8b, all results (both experimental and simulated) collapse to a single curve, described by the equation:

$$\tau = 1.127\frac{Pe}{\Psi_E} + 0.0047 \quad R^2 = 0.998 \tag{2.8}$$

For a given set of instrument flowrates, such collapse is expected, as Pe/Ψ_E is inversely proportional to the electrophoretic velocity of particles within the drift region and all data were collected with a constant advective (counterflow) velocity profile. Equation (2.8) specifically applies for the experimental data below 12 seconds, for which $\Psi_E >> Pe$ is approximately satisfied and for which the average deviation in electrical mobility for the measured and simulated values compared to the values obtained from Equation (2.8) is 4.8%. The additional value of 0.0047 results from particle transit time to the detector, and is thus tubing length and detector dependent, while the coefficient 1.127 would vary with changing flow conditions in the drift region. However, with the prototype operated

as described here, Equation (2.8) can be used as a calibration curve for DTIMS measurements, directly linking the midpoint electrical mobility of detected particles to the measurement time, drift region length, and applied voltage for $Pe/\Psi_E<0.1$.

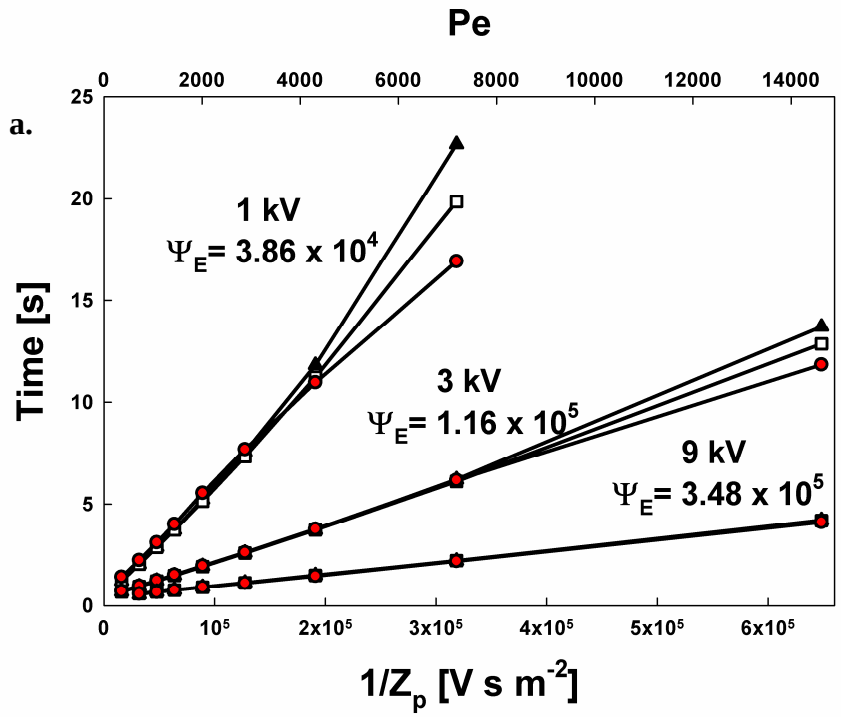

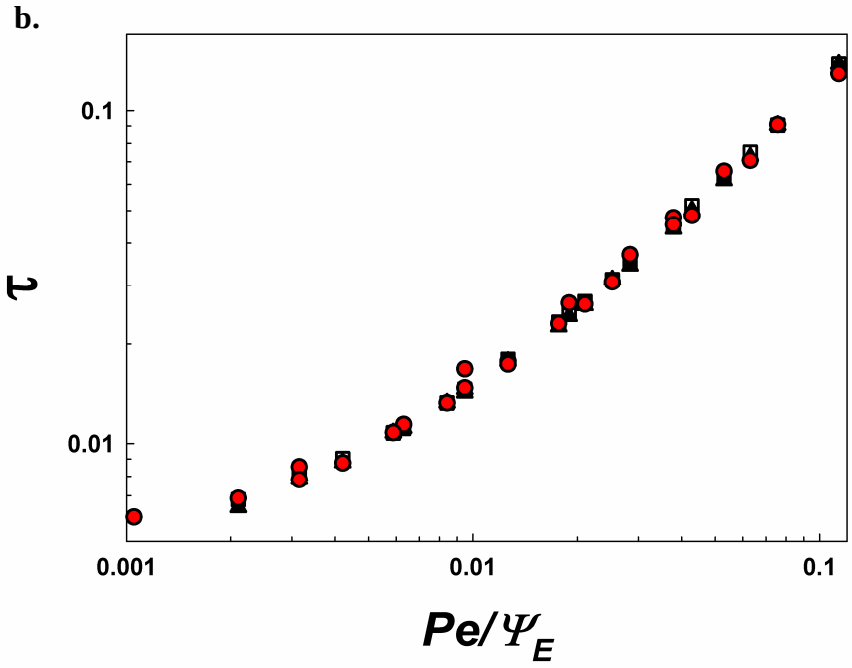

Figure 2.8. (a.) Peak time in ATDs as a function of inverse mobility for DMA size selected particles from experiments (red circles), numerical based simulations (black triangles), and the analytical based simulations (white squares). (b). Dimensionless peak time as a function of Pe/Ψ_E.

Simulated & Experimentally Measured Transmission Efficiency

The transmission efficiency of the DTIMS instrument was also examined via both experiments and numerical simulations. The number detected per unit inlet concentration is appropriately non-dimensionalized by the sample volume. However, as noted prior, the sample volume itself is difficult to estimate, and further is dependent on a number of instrument operating parameters, most of which remained fixed in the instrument. Therefore we opt to quantify transmission efficiency dimensionally, by plotting the total number of detected particles per unit inlet concentration as a function of Pe/Ψ_E in Figure 2.9, with results from both simulations and experiments shown. In the absence of losses, the value on the ordinate in Figure 5, with units of volume, is a measure of the sample

volume size. The absolute values found are in reasonable agreement with the sample volume width of 0.8 cm assumed in the analytical model (the sample volume would be a 4.8 cm^3 oblate semi ellipsoid with 1.7 cm, estimated from the *Fluent* model, as the major radii). Experimental data and simulation results are in excellent agreement with one another, and both again collapse to a curve dependent on Pe/Ψ_E, displaying a clear maximum about $Pe/\Psi_E \approx 0.08$, near the value above which non-linearity in the measurement time- inverse electrical mobility curve is evident. For values of this ratio below 0.1, the transmission efficiency of particles is heavily influenced by electrostatic deposition at the counterflow screen (examples visible in Figure 2.6). For high concentration aerosols, where losses do not prohibit measurement, this effect can also be beneficial to resolution, as the detector preferentially samples particles which have traversed the drift region near the axis, limiting plume spreading due to the flow profile. Conversely, $Pe/\Psi_E > 0.1$ results in particle losses at the drift region inlet (also visible in Figure 2.6 for the 10 nm, 1kV example).

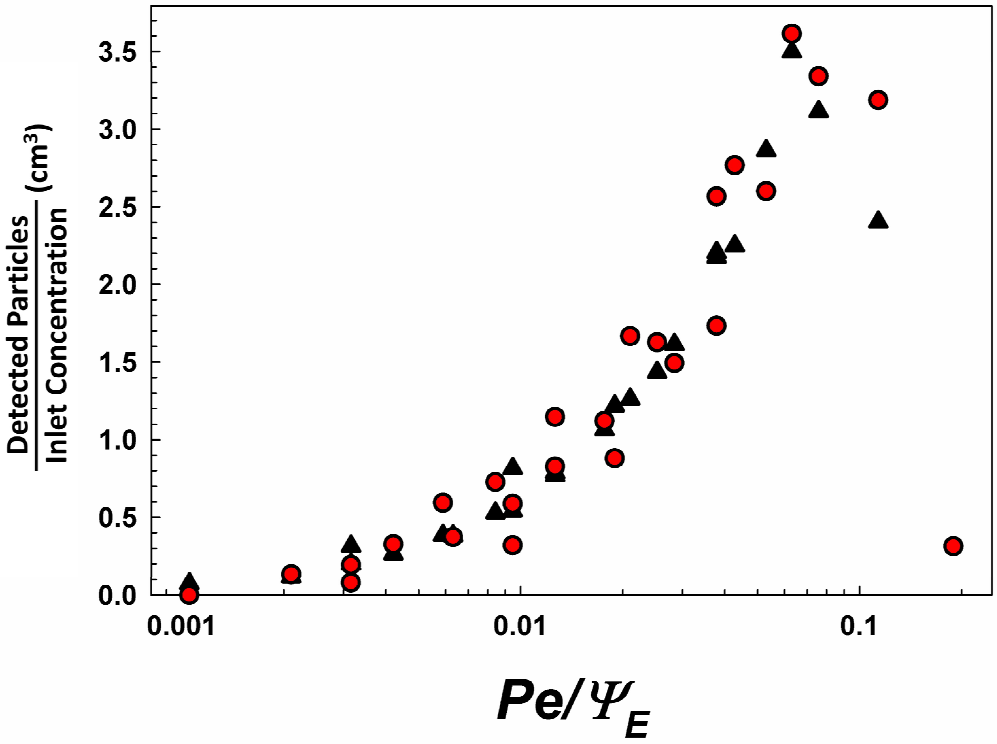

Figure 2.9. The number of detected particles during a measurement per unit inlet concentration as a function of Pe/Ψ_E. Red circles show measured values and black triangles show simulated results.

Resolving Power

The resolving power introduced in the analytical model describes the variation in drift time for perfectly monodisperse particles entering the inlet. However, this value alone does not reflect the resolution attained during a measurement, as in its calculation variations in counterflow velocity in the drift region (spatial), transit time through tubing, and transit time within the detector are not considered. In order to quantify the total resolving power of the prototype when coupled to a specific detector, we infer the value $R_{sys} = (Z_{p,peak}^{-1})/(\Delta(Z_p^{-1}))$. This is accomplished by first fitting normalized ATDs to Gaussian distributions (described by a mean value and variance, and determined

neglecting the tails within ATDs as well as Poisson weighting distributions [40]), and then converting Gaussian distributions to an inverse mobility scale (based on calibration), with mean value $Z_{p,peak}^{-1}$ and FWHM $\Delta(Z_p^{-1})$. The fitting procedure was performed for measured, simulated, and analytical results using both WCPC models 3786 and 3788, whose average response times (neglecting the tubing connect the drift region to the CPC inlet) are 280 and 850 milleseconds, respectively, with response time distribution FWHM of 50 and 210 milleseconds, respectively.

Measured, simulated, and analytical values of R_{sys} with the WCPC model 3786 and 3788 are shown as functions of Pe/Ψ_E in Figure 2.10a & b, respectively. In calculating resolving powers we assume that the contribution of the DMA transfer function width is negligible (i.e. DMA-selected particles with a resolving power of 36 are effectively monodisperse). Additionally shown are the resolutions calculated from simulation results neglecting the influences of the detector. As evidenced by Equation (2.4d) directly, R_{sys} for the drift region alone is not a function of Pe/Ψ_E alone, as the resolving power of the drift region is expected to be determined by Ψ_E-Pe. Nonetheless, results are plotted in this manner because (1) Equation (2.4d) predictions suggest that resolution for the prototype instrument is more dependent on $\Delta x/L$, and (2) the other influences on R_{sys} are those that also influence transmission, and are approximately dependent on Pe/Ψ_E. Fluctuations in both the analytical model calculated and simulation inferred resolving powers are evident, which result from the fact that both models utilize stochastic particle sampling to construct ATDs, and because obtained ATDs are not purely Gaussian distributions. Even so, Gaussian fitting reveals that system resolution

increases with increasing Pe/Ψ_E, which correspondingly indicates that system resolution increases with increasing drift time. Evidenced by the higher resolving powers found for results of simulations without including the influence of the detector, as well as the difference in resolving power found with the model 3788 & 3786, a substantial improvement in resolution at low Pe/Ψ_E values can be made through the use of a narrow response time distribution detector. This differs from the manner in which resolution is improved in DMAs and in drift tubes used in gas phase ion measurement, which is by increasing Ψ_E [6, 18]. We note finally, that for the measured distributions, as Pe/Ψ_E increases, deviations from analytical and simulated results are apparent. This is further indicative of flow non-uniformities detected in non-axisymmetric simulations, which can be rectified through prototype modification. For the size range examined (< 10 nm), however, the measured drift tube resolving power is on par with that of the TSI nano-DMA model 3085 [5].

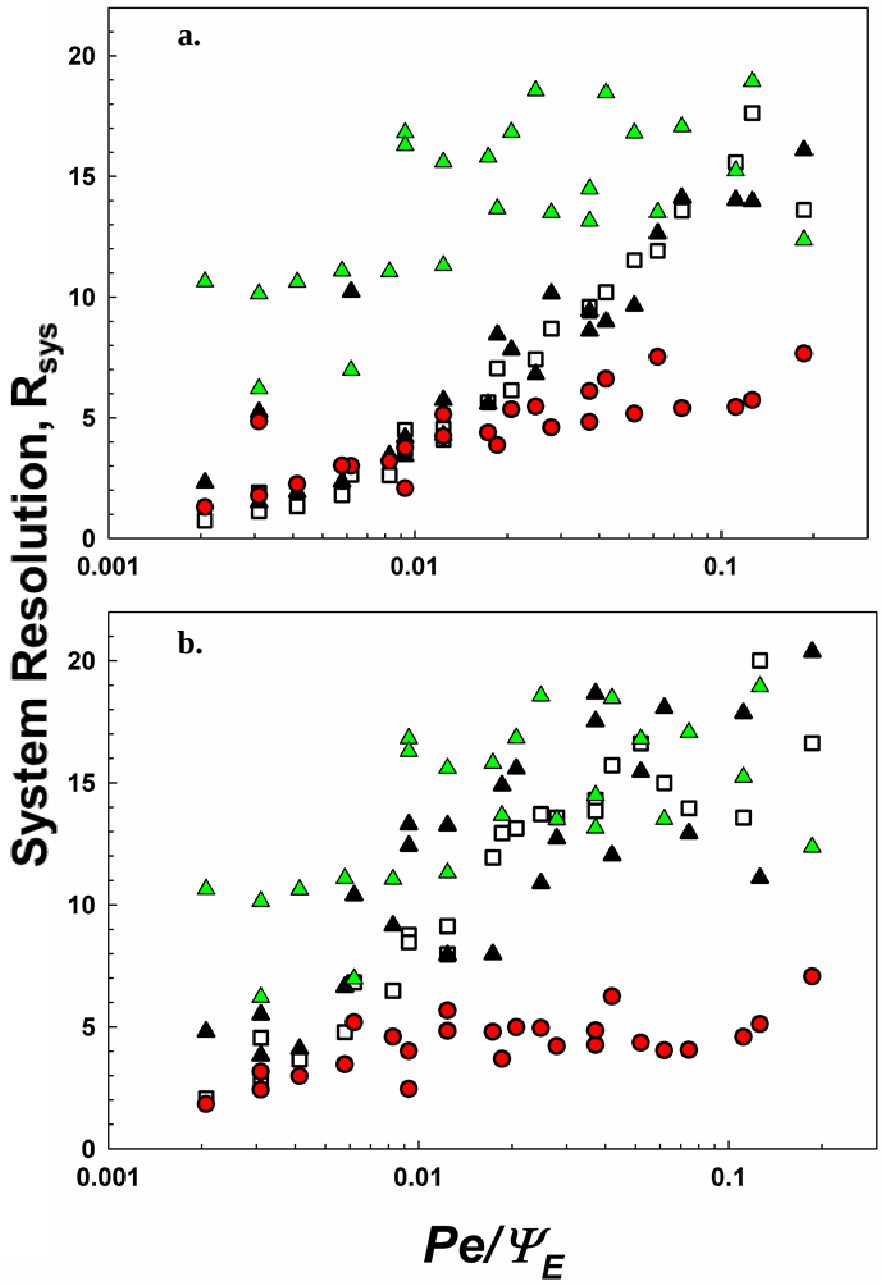

Figure 2.10. The system resolving power of for the DTIMS prototype determined with (a.) a 3786 WCPC and (b). a 3788 WCPC used as detectors. Red circles correspond to measured values, black triangles to simulation results, green triangles to simulation results neglecting detector influences, and open squares to analytical results. The scatter in the calculated results reflects the finite number of particles that were tracked numerically.

2.4 Measurement of Multimodal Protein Aerosols

Measurements of electrosprayed protein solutions [41] were made to demonstrate the performance of the DTIMS prototype for particles with multimodal electrical mobility distributions. For these experiments, non-denatured protein solutions were prepared following the procedure described by Maiβer et. al. [42] and an electrospray aerosol generator (EAG, TSI 3480) with a Po-210 bipolar ion source installed was used for ion generation. The output of the EAG of ~1.0 l min^{-1} was delivered directly to the DTIMS inlet where the excess aerosol is also vented to a filter. Maximum counts per channel normalized results are shown in Figure 2.11. Multimodal distributions arise for the proteins examined (cytochrome C, lysozyme, & myoglobin) because during the electrospray process both non-specific protein multimers form when more than a single protein is enclosed within a produced droplet and although the Po-210 bipolar ion source within the electrospray aerosol generator substantially reduces the level of charge on produced droplets, singly, doubly, and triply charged particles exit the Po-210 chamber [42]. The peaks in electrical mobility distributions for monomer and dimer protein ions detected are labeled in the Figure 2.11 plots, with additional peaks also apparent. In addition, the measured ATDs were converted to inverse electrical mobility, facilitating direct comparison to the measurements of Maiβer et al (2011). In plots it is clear that the DTIMS prototype is able to sufficiently resolve the separate protein peaks, and enables similar measurements to a DMA for charged reduced protein ions. The small offset in the peak locations between the measurements with the DTIMS prototype and the DMA is presumably due to a variable amount of residue on the protein ions generated in each

experiment; noticeable differences in the sizes of electrospray generated but charge reduced protein ions have been noted previously [43-44]. Of note for DTIMS generated spectra is the speed at which they were obtained (<30 seconds for 1kV, <5 seconds for 9 kV) compared to scanning tandem DMA measurements, which often span several minutes. However, for the shorter drift times (where Ψ_E is smaller) it is apparent that the resolution of the device (peak separation) suffers, and differences in relative peak intensity are apparent because of the electrical mobility dependent transmission of the DTIMS prototype as compared to the DMA.

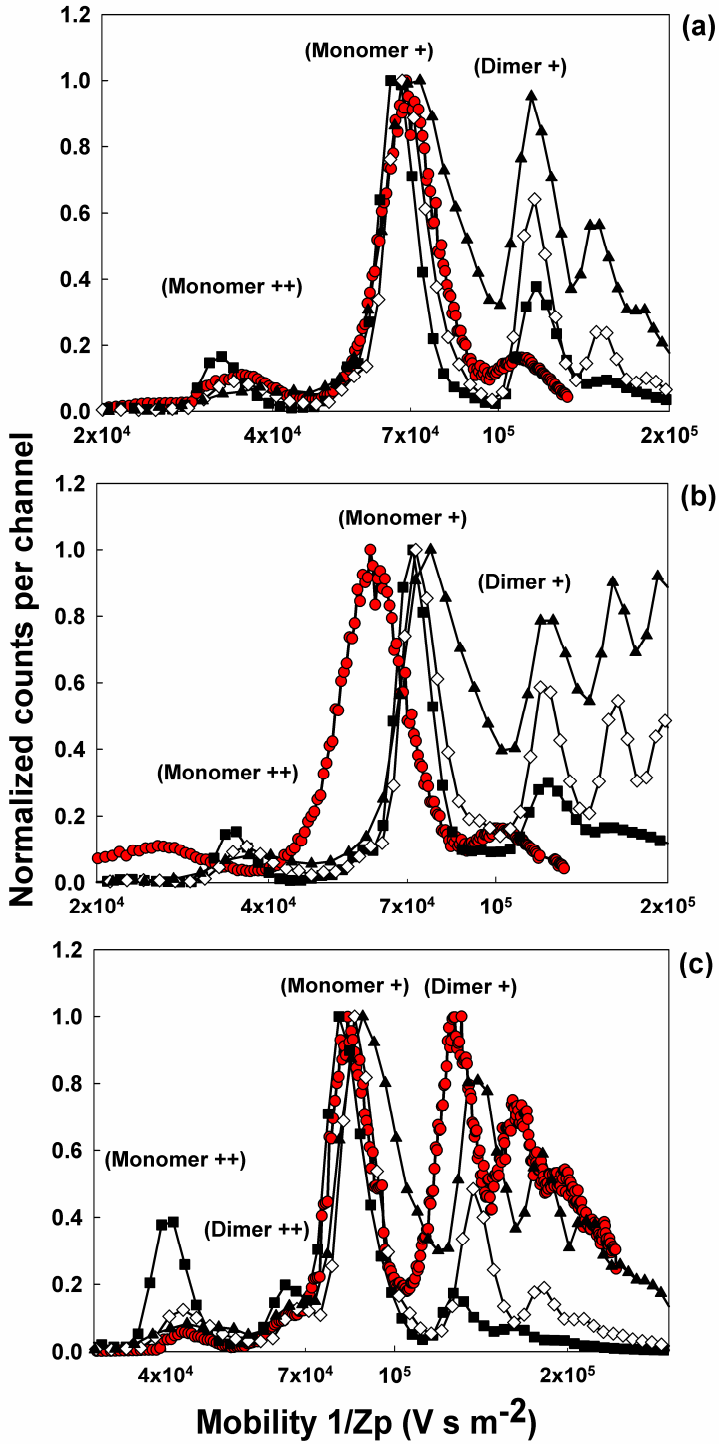

Figure 2.11: (a) Cytochrome C, (b) Lysozyme, and (c) Myoglobin ion electrical mobility spectra for DTIMS voltages of 1kV (black squares), 3kV (open diamonds), 9kV (black triangles), and published results using a high resolution DMA (red circles).

2.5 Enhancements to the Prototype Device

2.5.1 *Spatially Varying Fields*

Particle trajectory simulations show that a significant portion of the sampled aerosol is deposited on the ground electrode and the end of the drift region versus being drawn into the detector. This effect is in some ways beneficial in that the particles that are ultimately sampled have experienced a more uniform drag force from the drift gas, limiting flow induce degradation of resolution. For low number concentration aerosols, when resolution is not as critical as compared to the need to maximize signal intensity, the aerosol can be focused by exploiting the Poisson-Laplace equation in the absence of space charge:

$$\nabla^2 V = 0, \tag{2.9}$$

where V is the voltage potential. The Laplacian can be written in cylindrical coordinates,

$$\frac{1}{r}\frac{\partial}{\partial r}\left(r\frac{\partial V}{\partial r}\right)+\frac{\partial^2 V}{\partial z^2}=0, \tag{2.10}$$

due to the axial symmetry of the drift tube geometry. The electric field in the device is determined by the voltage gradient:

$$\nabla V = -\vec{E}, \tag{2.11}$$

which allows Equation 2 to be written as

$$\frac{1}{r}\frac{\partial}{\partial r}(-rE_r)+\frac{\partial}{\partial z}(-E_z)=0, \tag{2.12}$$

where E_z and E_r are the electric fields in the axial and radial directions. For typical applications of drift tubes, E_z is constant and therefore E_r must be zero. If E_z varies with

the axial position z then a radial field E_r is present and can be exploited to guide charged particles towards, or away from, the axis. If the value for

$$\frac{\partial}{\partial z}\left(-E_z\right)=\frac{\partial^2}{\partial z^2}V = f(z)\,. \tag{2.13}$$

Equation (2.12) can then be written as

$$\frac{1}{r}\frac{\partial}{\partial r}\left(rE_r\right)= f(z)\,, \tag{2.14}$$

leading to

$$d(rE_r) = f(z)rdr\,, \tag{2.15}$$

which after integration gives

$$E_r = \frac{f(z)r}{2}\,. \tag{2.16}$$

Equation (2.16) shows that when the magnitude of E_z increases along the axis then there is a corresponding gradient $E_r(r)$ that acts radially, pushing ions towards the center of the drift region.

In an ideal case, particles that are near the wall at the beginning of the drift region will approach the centerline just prior to the end of the drift region. To determine $f(z)$ required for this case, the time required for the desired radial displacement of the particle can be equated to the total drift time. The velocity v of a charged particle in an electric field is given by

$$\vec{v} = Z_p\vec{E}\,, \tag{2.17}$$

where Z_p is the electrical mobility of the particle. The time required for a given radial displacement of a particle is found by integrating Equation (2.16) in the *r* and *z* directions. For *r*:

$$\frac{dr}{dt} = Z_p E_r = \frac{Z_p f(z) r}{2},$$

$$\int_{r_{max}}^{r_{min}} \frac{dr}{r} = \int_0^t \frac{Z_p f(z) dt}{2},$$

$$\ln\left(\frac{r_{max}}{r_{min}}\right) = \frac{-Z_p f(z) t}{2}, \tag{2.18}$$

$$t = -\frac{2\ln\left(\frac{r_{max}}{r_{min}}\right)}{Z_p f(z)}.$$

Figure 2.12 shows pathlines for 2nm particles along with the gradient E_r (blue represents $E_r=0$, red is $E_r=1000$ *V/m*) for *V(z) set at* $V=-19000z^2-95z+1000$ which represents a sample case for a prototype geometry with r_{max} = 0.02m r_{min} = 0.002m, and z_{end}.= 0.227m.

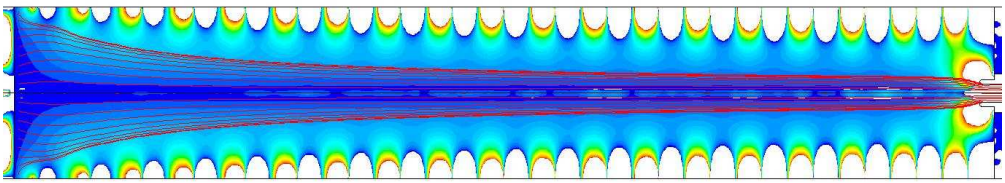

Figure 2.12: Particle pathlines and E_r contours for a spatially varying field.

2.5.2 *Time Varying Fields*

As shown in Figure 2.6, the losses of small particles at high drift voltages are attributed to the increased drift velocity near the detector inlet causing a higher fraction of particles to precipitate at the end of the drift region vs. being aspirated by the detector. In addition to advective losses at the inlet, the reduced transmission efficiency for large particles at low drift flows is due to the longer drift times and associated diffusion losses to the walls of the device. This effect can be reduced by ramping the drift voltage from a low value to a higher value (linearly or by some other time dependence) throughout the measurement. Figure 2.13 shows the transmission efficiency for a voltage ramp beginning at 500V and rising linearly to 9kV over 20 seconds compared to constant voltage transmission.

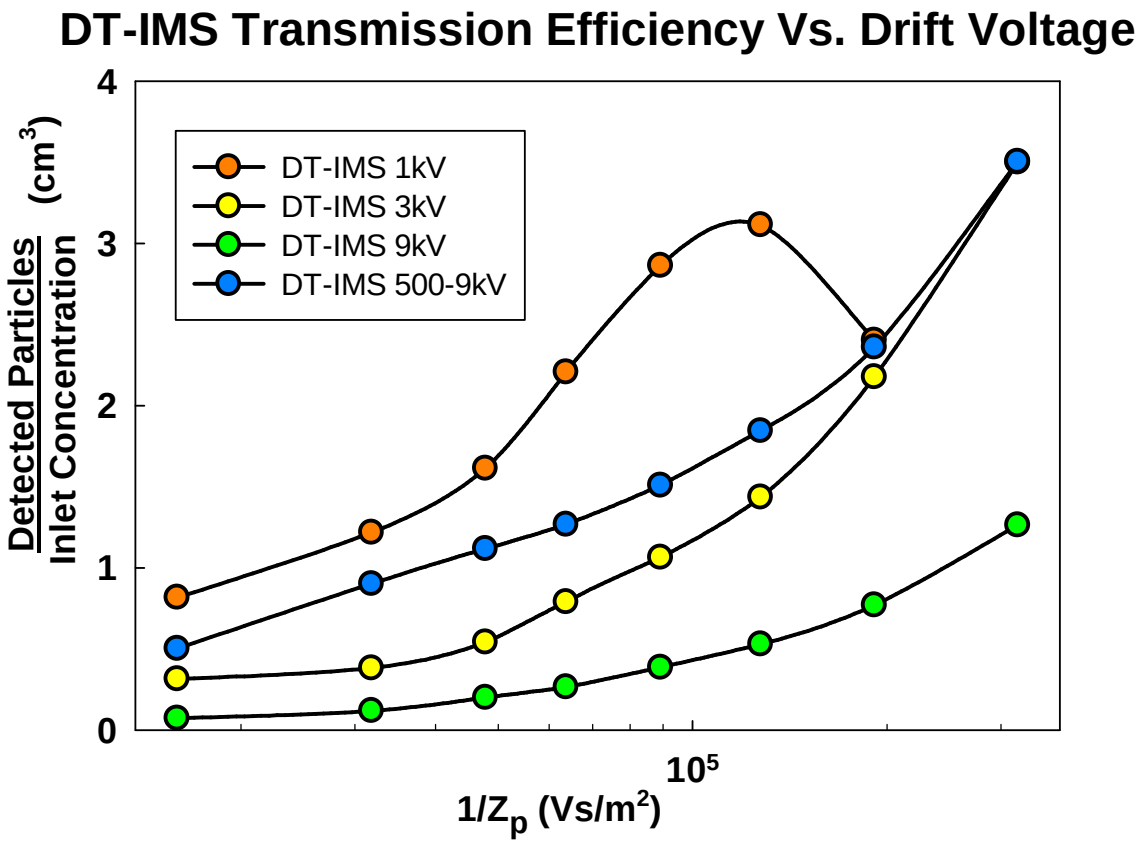

Figure 2.13: Transmission efficiency including results from voltage ramping

The transmission efficiency for small particles is improved as is the uniformity of transmission efficiency vs. size. The ramp rates and endpoints have not been optimized and it is expected that further improvements could be achieved.

2.6 Conclusions

A drift tube ion mobility spectrometer for measurement of aerosol particles has been developed, and the instrument's performance has been analyzed by experimental, theoretical, and numerical means. The arrival times and transmission efficiency of the device are shown to be a function of the ratio of the dimensionless parameters Ψ_E and Pe. Comparison of arrival time distributions between models and measurements support the efficacy of these models for estimating device performance for drift times less than ~10 seconds. At longer drift times predictions for ATDs diverge from measurements, and the measured resolving power of the device falls well below the predicted resolving power. Better agreement between the simulated and measured ATDs can likely be achieved by improvements to the flow diffusers used to distribute the flow evenly within the device. Further improvements to the design may include shortening the inlet and outlet regions to minimize diffusion losses as well as reduce time based broadening, and use of a detector with a narrower response time distribution function. The advantages of the DTIMS for particle analysis over traditional devices include relatively fast measurement times and insensitivity to changing aerosol conditions throughout the measurement period. Additionally the DTIMS is ideally suited to be placed downstream of a DMA for tandem electrical mobility measurements, as the DMA-DTIMS combination is the electrical

mobility analog of a quadrupole mass filter-time of flight mass spectrometer (both system utilize narrow pass filters followed by time-based spectrometers). To date, our work has focused on analyses that allow measurement of size and size change. Additional work will be required to assess number distributions of the sampled aerosol, although in principle this is possible.

Chapter 3 Tandem High Resolution Differential Mobility – Drift Tube Ion Mobility Spectrometer Analysis

3.1 Introduction

Vapor molecules present in an aerosol can substantially alter the size and chemical composition of particles,[45-48] as particle-vapor molecule collisions lead to the sorption of vapor molecules onto particles (heterogeneous uptake). Although classical theories (e.g. Kelvin-Thomson equation [49-50]) can be used to describe heterogeneous uptake, in many situations these approaches are inadequate,[51-54] as they invoke bulk property values for both vapor molecules and particles. Errors with classical approaches are particularly evident in predicting heterogeneous uptake by particles which have sizes close molecular dimensions,[51-52] when the particle is soluble in the condensed liquid,[55-57] or if sorption leads to formation of a vapor molecule monolayer on the particle surface.[58] While modifications to classical theories have been developed [57, 59-64], measurements of vapor molecule sorption by aerosol particles remain necessary to better understand heterogeneous uptake, particularly during the initial stages, i.e. when the sorbed species represents only a small fraction of the total particle mass.

Previously developed experimental techniques designed to study uptake can be described as either equilibrium or non-equilibrium methods. The latter involve measurement of either the critical diameter for particle nucleation [27, 65] (the smallest sized particle/cluster which will grow continuously via vapor molecule uptake subject to a given vapor saturation ratio) or nucleation rates of particles in a controlled supersaturation ratio vapor [51, 54, 66-67] (which can be linked to the critical diameter).[68] Such experiments provide valuable information on particle growth in supersaturated environments; however, they do not afford direct examination of the initial stages of uptake, as measurements on particles are made only after uptake increases particle sizes to the supermicrometer size range. Conversely, experiments that investigate heterogeneous uptake under equilibrium conditions are suited to examine the initial stages of vapor molecule sorption, e.g. the formation the vapor molecule monolayers. Techniques along these lines include tandem differential mobility analysis (TDMA),[69-70] electrodynamic balances (EDB),[71-74] and high pressure mass spectrometry (HPMS).[52-53] Collectively, such measurements enable study of particles over a wide size range, yet leave a window in the ~2 - 10 nm size (diameter) range where measurements are difficult. The objective of this work is therefore to demonstrate the capabilities of a measurement system for equilibrium measurements of heterogeneous uptake by sub-10 nm particles. Specifically, the measurement system is composed of a high sheath flow rate DMA coupled to the drift tube ion mobility spectrometer (DTIMS) described in Chapter 2. The use of a DMA-DTIMS aids in overcoming issues encountered using TDMA with low concentrations of particles in the sub 10 nm size

range, and further controlled vapor molecule concentrations in the drift tube region of the DTIMS are more easily achieved than in non-recirculating DMA sheath flows (necessary in TDMA measurements). In the proceeding sections, the DMA-DTIMS system is described in detail and laboratory results for the sorption of water vapor molecules to LiI and NaI salt particles in the 2.85 – 7.6 nm size range are presented. In addition, an analysis approach is provided which facilitates comparison of DMA-DTIMS measurements to theoretical predictions of heterogeneous uptake. This approach is utilized for comparison to a modified form of classical theory here, and can be used for comparison to other theoretical predictions as well as with results from similar mobility based measurement systems (e.g. TDMAs). Finally, we examine the precision of the system and estimate the minimum detectable shift in electrical mobility (quantified by growth factor) arising from heterogeneous uptake, and show that for an experimentally reasonable number of detected particles, precisions on the order of 0.1% are possible.

3.2 Experimental Methods

3.2.1 *DMA-DTIMS System Description*

A schematic of the tandem DMA-DTIMS system is shown in Figure 3.1a. The DMA in the presented system is the ½ mini-DMA (Nanoengineering corp.) which is described in detail by Fernandez de la Mora & Kozlowski,[4] with the general operating principles of modest-to-high resolving power DMAs described elsewhere.[75] The DMA is operated with a sheath flow of air in recirculating mode (using a Domel Inc. vacuum blower) with a HEPA filter to remove particles positioned downstream of the blower. A

water cooled heat exchanger similar to that used by Fernandez-Garcia & Fernandez de la Mora[76] is used to maintain the sheath gas temperature at ~22^{o} C. The flowrate of aerosol entering and exiting the DMA is held at ~5 l min^{-1}. Because the sheath flowrate is on the order of 100 l min^{-1}, it is difficult measure precisely. Therefore, the electrical mobility selected when a specific applied voltage is applied to the DMA is inferred by first determining the voltage at which an ion of known electrical mobility is maximally transmitted. The calibration ion is the tetradodecylammonium^{+} ion, whose electrical mobility was measured accurately by Ude & Fernandez de la Mora [20] in air, near atmospheric pressure close to 20^{o}C. Assuming that a hard-sphere relationship can describe the electrical mobility of this ion (supported by measurements [32] and calculations [77] by Larriba & coworkers), the tetradodecylammonium^{+} electrical mobility is adjusted [78] to correct for the slight temperature (~22^{o}C) and pressure (1% above atmospheric pressure) differences in the DMA employed here. To select particles of a prescribed electrical mobility (a function solely of particle diameter for singly charged particles under prescribed background gas conditions, noted subsequently), voltage is applied to the inner electrode; for this reason, at the DMA outlet, a semiconductive polymeric tube (Ensital SD, Piper Plastics Inc., Illinois, USA) is connected to isolate the DMA inner electrode electrostatically from the remainder of the system, which is held at ground potential.

After exiting the DMA, the flow of electrical mobility selected particles is split, with 1 l min^{-1} entering the DTIMS and the remainder entering a HEPA filter and vented to atmosphere. The DTIMS is operated as described previously,[79] with 1 or 3 kV

applied as the drift voltage and with a WCPC[26-27] (water CPC) model 3788 (TSI Inc., Minnesota, USA) used as the detector. The WCPC operates with a flowrate of 0.615 l min^{-1}, and the DTIMS counterflow is nominally set at 0.2 l min^{-1}, with the sum of these flows entering the drift region at the counterflow inlet. DTIMS measurements are quantified by arrival time distributions (ATDs), which express the number of particles detected per unit measurement time, as a function of the measurement time. Total measurement times less than 10 seconds are employed. The DTIMS operates in its linear range, wherein the drift time (and measurement time) is linearly proportional to the inverse electrical mobility of the particles traversing the drift region.[18] To control the vapor molecule concentration in the drift region for heterogeneous uptake experiments, a nebulizer, depicted in Figure 3.1b, is placed upstream of the counterflow inlet. The nebulizer is operated with 0.815 l min^{-1} of ultra high purity zero air (Airgas) with controlled water volumetric flow (using New Era syringe pump). Liquid water flowrates range from 0.05 – 4 μl min^{-1}. The present study is limited to measurements with water vapor in the RH < 30% range near room temperature; expanding the operational range will addressed in future DMA-DTIMS embodiments. To remove residue particles remaining after the nebulizer (water droplets evaporate, however each droplet contains some amount of non-volatile residue) a glass fiber filter is placed downstream of the nebulizer prior to the counterflow inlet. The dew point of the drift region is nominally calculated from the mass flow rate of water entering the nebulizer and the counterflow inlet rate (0.815 l min^{-1}), and periodically validated using a dew point hygrometer (General Eastern). It is found that the measured and the calculated dew points vary by

0.5^{o} C at most for the values that can be measured by the hygrometer. The temperature is also measured at the counterflow inlet, and used in conjunction with the dew point measurement/calculation to determine the RH of the drift region.

All DTIMS flows are maintained with mass flow controllers (MKS Instruments) and calibrated using a bubble-type flowmeter (Sensidyne Inc.). The operation of the complete DMA-DTIMS system is controlled via a *LabVIEW*^{TM} (National Instruments) program, and all voltages are applied using Bertan high voltage power supplies. Positively charged particles are examined for the presented results; thus, a negative voltage is applied to the DMA inner electrode and the drift voltage is positive. DTIMS ATDs are determined directly from the WCPC counts (collected via the *LabVIEW*^{TM} program) and binned in units of log scale time.

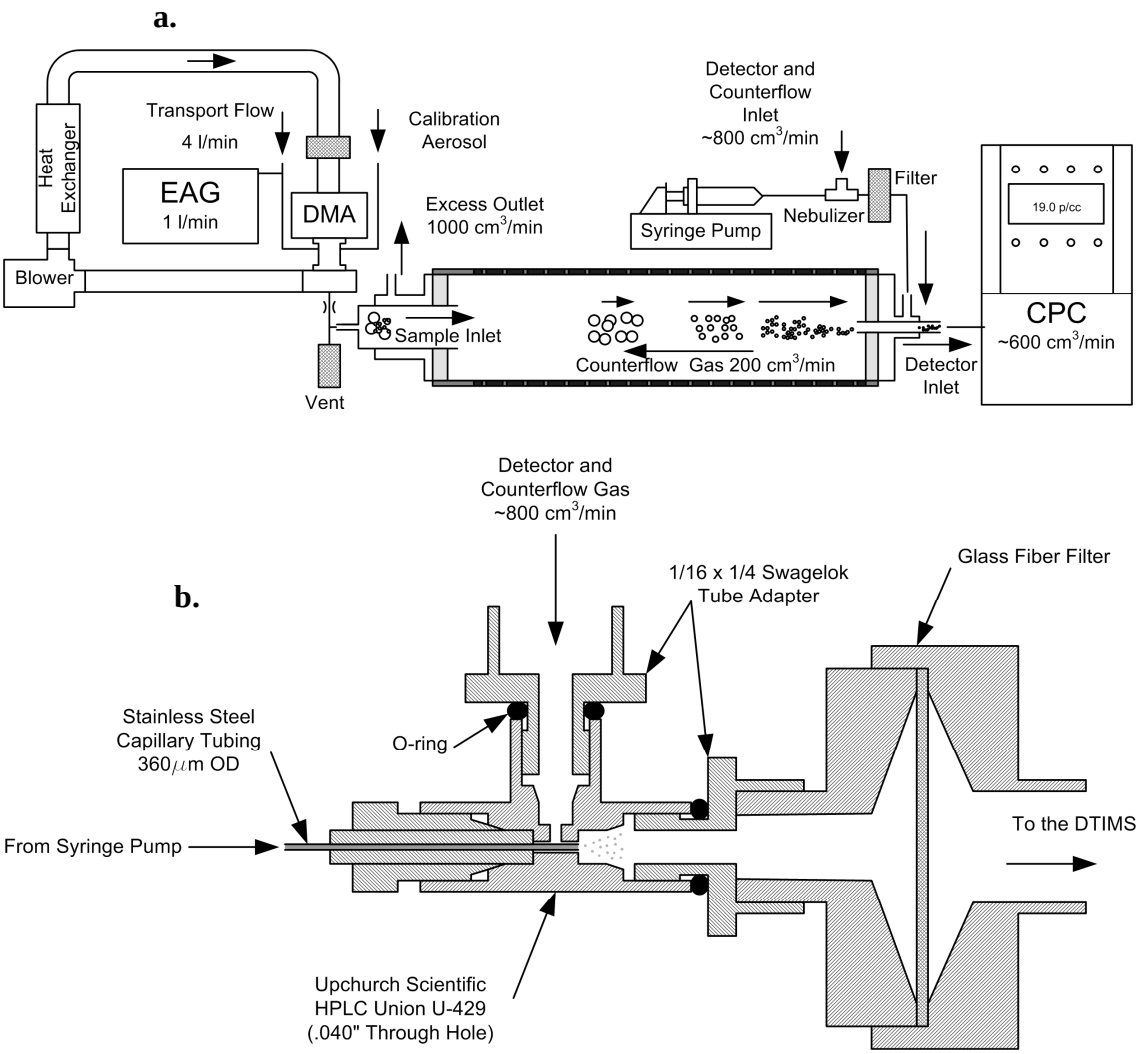

Figure 3.1: (a.) Schematic of the DMA-DTIMS system. EAG: Electrospray Aerosol Generator; DMA: Differential Mobility Analyzer; CPC: Condensation Particle Counter. (b.) Schematic of the nebulizer used to humidify the drift tube counterflow gas.

3.2.2 *Laboratory Measurements*

With the DMA-DTIMS operated as noted, measurements of vapor uptake were performed for particles composed of lithium and sodium iodide. These salts were chosen for analysis due to their low saturated aqueous solution activities, $a_{w,sat}$, (0.186 ± 0.002 and 0.397 ± 0.006 at 20°C for LiI and NaI respectively).[80] Nanometer scale particles

composed of these salts were generated via charge reduction electrospray with a model 3480 electrospray aerosol generator [41] (TSI Inc., Minnesota, USA) operated with a 40 μm inner diameter silica capillary and with ultrapure zero air as the carrier flow at 1.0 l min^{-1}. The electrosprayed solutions were prepared in HPLC grade methanol (Sigma-Aldrich, Saint Louis, MO, USA) at salt concentrations of 0.1, 0.3, and 1.0 mM. Ammonium acetate (20 mM) was added to increase the solution electrical conductivity, facilitating stable cone-jet formation. Although the addition of ammonium acetate led to significantly more NH_4^+, CH_3COO^- ions in electrospray solutions and generated droplets than Li^+, Na^+ or I^- ions, we believe this minimally influenced the chemical composition of electrospray generated particles, as ammonium acetate clusters themselves are known to be extremely volatile at room temperature (with cations and anions reacting and evaporating as ammonia and acetic acid, respectively). In separate differential mobility analyzer-mass spectrometer (DMA-MS)[81] measurements of electrosprayed ions generated from the solutions used in experiments (but not charge reduced, as is described subsequently for DMA-DTIMS measurements), we did not detect any stable NH_4^+ or CH_3COO^- containing cluster ions, while at concentrations of 20 mM with non-volatile species and under near-identical electrospray conditions, 1-10 nm diameter cluster ions are routinely observed.[32, 78, 82] Moreover, small perturbations to the chemical composition of the generated particles neither invalidate the ability of DMA-DTIMS system to detect heterogenous uptake derived mobility shifts, nor do they strongly influence the results of the comparison performed to classical theory predictions.

A 5 mCi Po-210 source was used to produce roughly equal concentrations of positive and negative ions, which, via collisions,[30, 35] reduced the charge levels of electrosprayed droplets such that most of them did not fission during the evaporation process. The resulting size distribution of nanoparticles produced hence reflected the initial size distribution of the electrosprayed droplets (determined by the droplet size distribution and non-volatile salt volume fraction in the solutions used [83]). Upon achieving a near-steady state charge distribution due to collisions with ions, the majority of generated nanoparticles were neutral, and the majority of the charged particles were singly charged (positively or negatively).[30] In stable operation the electrospray aerosol generator produced particles in the 2-10 nm diameter range with a fairly monodisperse (geometric standard deviations of ~1.1) size distribution function, the geometric mean of which was adjustable based on the salt concentration in solution and liquid flowrate. An additional ~4.0 L min^{-1} was added immediately downstream of the EAG to reduce diffusion losses in the tubing leading to the DMA inlet. For each of the salt concentrations, the peak electrical mobility of the distribution was measured and this mobility was then selected by the DMA. DMA selected particles entered the DTIMS, which was operated with a prescribed RH. Three to ten individual ATDs were accumulated for each DMA selected electrical mobility and RH value; reported ATDs are the average of these individual ATDs. A two-minute pause between different RH values was used to ensure that RH within the drift tube achieved the prescribed value. After the final RH measurement the syringe pump was stopped and a final ‘dry’ ATD was measured after a ten-minute delay.

3.3 Results and Discussion

3.3.1 *Measurement Results*

Figure 3.2 displays plots of the normalized, $\log_{10}$ based ATDs, i.e. the average normalized counts per unit of $\log_{10}$ arrival time ($\Delta N/\Delta log_{10}(t)/N_{tot}$, where ΔN is the average number of counts in a channel, N_{tot} is the total number of average counts in all channels, and $\Delta log_{10}(t)$ is the measurement channel width, a constant for each measurement) as a function of arrival time, as determined for DMA selected particles. The electrical mobilities (Z_p) of these particles (singly charged) are determined directly from the DTIMS calibration equation [79] and are also displayed in Figure 3.2 plots. As the examined particles are approximately spherical, their electrical mobilities are converted to estimates of their diameters (d_p) via the free molecular limit of the Stokes-Millikan relationship [32]:

$$Z_p = \sqrt{\frac{\pi m_{air}}{8 k_B T}} \frac{3e}{\pi \rho \xi} \frac{1}{\left(d_p + d_{air}\right)^2} \tag{3.1}$$

where m_{air} and d_{air} are the average mass (29 Da) and diameter (0.3 nm) of the surrounding gas molecules, ρ is the gas mass density, ξ is a scattering coefficient (1.36), e is the unit charge, k_B is Boltzmann's constant and T is the temperature. Diameters corresponding to the peak electrical mobility selected by the DMA, calculated with Equation (3.1), are labeled in each Figure 3.2 graph (i.e. the diameters of the particles at zero relative humidity). In the plot for initially 5.6 nm NaI particles, a portion of the distribution was not measured, and therefore N_{tot} is artificially low. Apparent for measurements of both

NaI and LiI particles is a shift in the peak arrival time in ATDs at higher drift region RHs. To quantify this shift, which is indicative of heterogeneous uptake, the peak arrival time in each ATD is inferred by fitting a Gaussian curve to the experimental data using least squares regression.[40] In the fitting procedure, the contribution to the least squares error for each channel is weighted by $\Delta N^{1/2}$ for the channel in question (the average number of counts in the channel), which is in accordance with Poisson counting statistics. In addition, only arrival times within two standard deviations of the peak drift time are considered. The peak arrival times are converted to electrical mobility using a calibration curve [79] and Equation (3.1) is again used to infer a particle diameter for the peak arrival time.

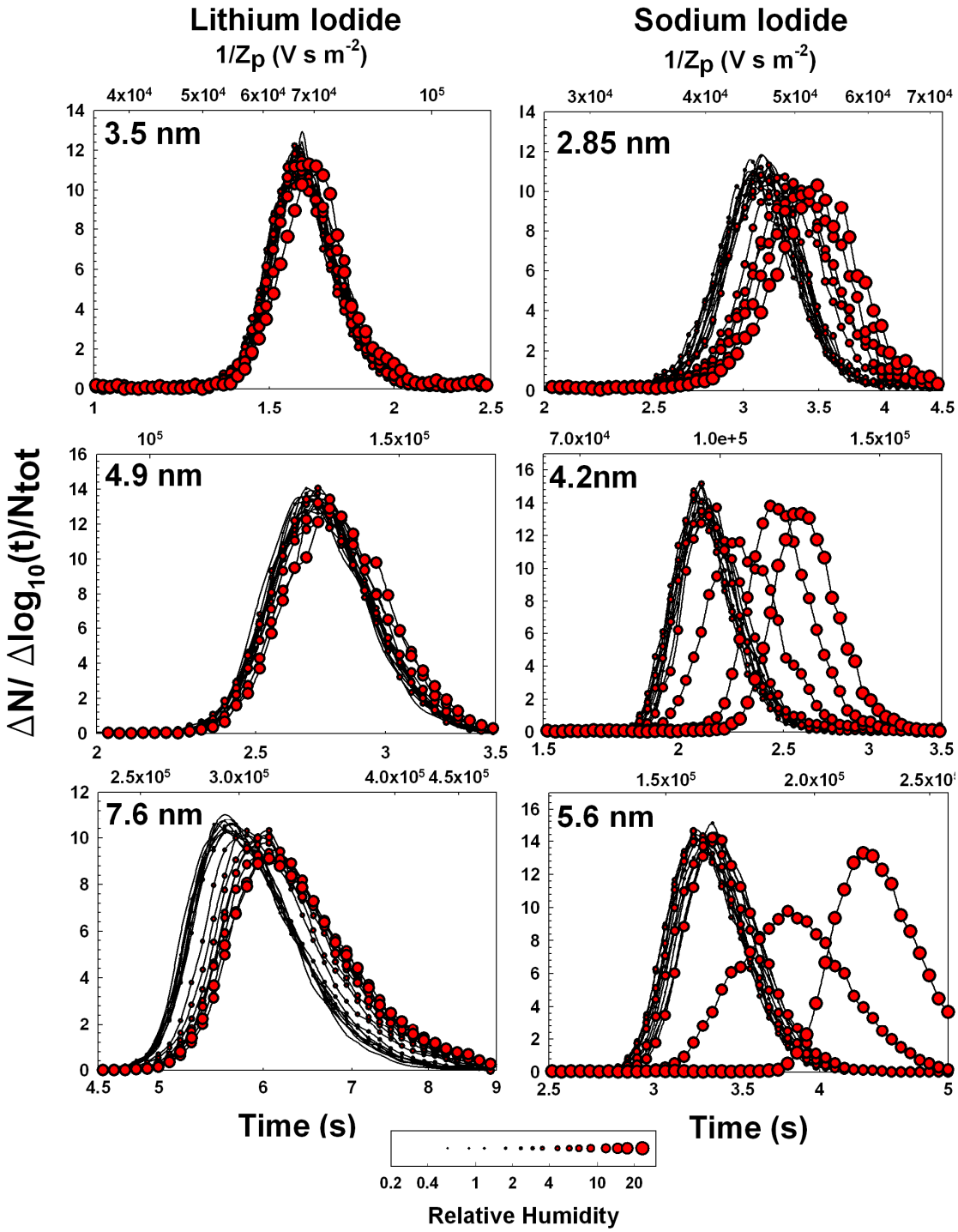

Figure 3.2: DMA-DTIMS Measured normalized arrival time distributions for lithium iodide and sodium iodode particles. The corresponding inverse electrical mobility is shown on the secondary axis for each of the measurements.

For measurements made with a particular relative humidity, a growth factor (*GF*) [56, 84] can be defined as the ratio of the peak arrival time's diameter under humidified conditions to the peak diameter for the same DMA settings in the absence of water vapor. To aid in subsequent analysis, we define the growth factor including the effective gas molecule diameter:

$$(GF)_{RH} = \frac{(d_p + d_{air})_{RH}}{d_0 + d_{air}} \tag{3.2}$$

where the subscript *RH* denotes the relative humidity of counterflow gas and the subscript *0* denotes dry conditions. Growth factors are plotted as a function of RH for three mobility selected diameters of lithium iodide and sodium iodide clusters are shown in Figure 3.3a and Figure 3.3b respectively. A growth factor slightly less than one is found at low RHs (< 5%) in several instances. This is likely due to either restructuring particles facilitated by collisions with water vapor molecules, or evaporation of ammonium acetate upon the addition of water. For lithium iodide, higher GFs are observed for larger particles, and the onset of growth for larger particles also occurs at lower RH values. For sodium iodide particles, larger GFs are again observed for the larger particles examined at the highest RHs; however, unlike lithium iodide particles, the onset of growth is apparent at lower RHs for the smaller particles examined.

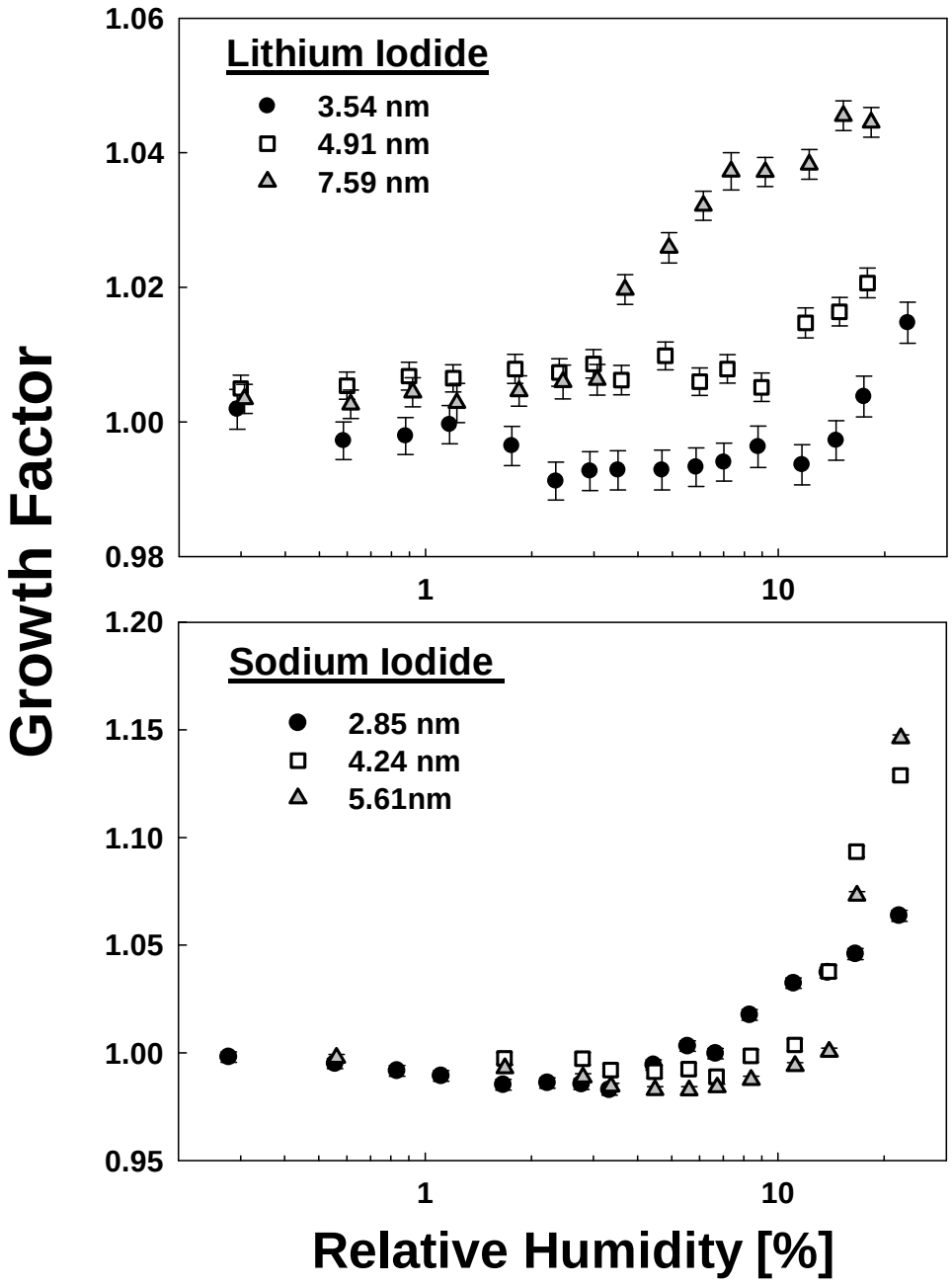

Figure 3.3: DMA-DTIMS inferred growth factors for (a.) lithium iodide and (b.) sodium iodide nanoparticles, measured at 23.2^{o} C and 24.2 ^{o} C respectively, as a function of the relative humidity of the drift region in the DTIMS. The method for determining the error bars is defined subsequently.

3.3.2 *Comparison to Theoretical Predictions*

The presented results show that DMA-DTIMS measurements can be used to probe heterogeneous uptake onto nanometer scale particles. Furthermore, measurements reveal differences in particle growth factors for different particle chemical properties and dry particle diameters. We now compare the extent of heterogeneous uptake observed, quantified in terms of the growth factor, to predictions based on classical (bulk) theories. For this analysis, we consider monomobile, singly charged, nanoparticles of homogenous chemical composition, which uptake individual vapor molecules. We further assume that nanoparticles traversing the drift region are in equilibrium with the surrounding water vapor, such that the rate of vapor molecule sorption onto nanoparticles with *g-1* vapor molecules attached (i.e. the number of vapor molecule- nanoparticle collisions per unit volume per unit time) is equivalent the rate of desorption of vapor molecules from nanoparticles with *g* vapor molecules attached. Therefore, the relationship:

$$\frac{n_g}{n_{g-1}} = n_{vap} K_{eq,g} = \frac{\alpha_{g-1}}{\beta_g} \tag{3.3}$$

holds valid, where n denotes a number concentration, $K_{eq,g}$ denotes the equilibrium constant for the reaction $n_{g-1} + n_v \Leftrightarrow n_g$, α_{g-1} is the sorption rate coefficient (vapor molecules sorbed per unit time from a single nanoparticle) and β_g is the desorption rate coefficient (vapor molecules desorbed per unit time from a single nanoparticle). The sorption rate is dependent upon the vapor molecule concentration (n_{vap}), the sticking probability (assumed unity here), as well as the vapor molecule-nanoparticle collision kernel.[85-86] For nanoparticles in the 2.85-7.6 nm diameter range, the ion-dipole

potential between charged nanoparticles and water vapor molecules (dipole moment = 1.85 D) may influence vapor molecule motion[87]. We therefore calculate $\alpha_{g\text{-}1}$ with the relationship:

$$\alpha_{g-1} = \frac{n_v \mathrm{H}_S k_B T (d_{g-1} + d_v)^3}{8 m_v D_v} \frac{\eta_{FM}^2}{\eta_C} \tag{3.4a}$$

where n_v is the vapor molecule number concentration, H_S is the dimensionless collision rate coefficient/collision kernel [85, 87], $d_{g\text{-}1}$ is the diameter of the particle undergoing vapor molecule collisions, d_v is the effective vapor molecule diameter (~0.38 nm, approximated from water's bulk density), m_v is the mass of the vapor molecule, D_v is the diffusion coefficient of the vapor in the background gas, and η_{FM} and η_C are the free molecular and continuum enhancement factors brought about by potential interactions, respectively.[35, 87] A similar equation can be written for the desorption rate coefficient:

$$\beta_g = \frac{n_s \mathrm{H}_D k_B T d_g^{\,3}}{8 m_v D_v}, \tag{3.4b}$$

where n_s is the vapor molecule concentration at the particle surface and H_D is the desorption rate collision kernel coefficient. These functional forms are adapted from those proposed by Ouyang et al[87], and in them the influence of potential interactions on the collisions (but not on desporption) is considered. Rigorously, these relationships apply for circumstances in which the vapor molecule is substantially more massive than the background gas molecules. Although this is clearly not the case for water vapor molecules in air, most theoretical studies suggest that deviations from the equations

presented here brought about by low mass vapor molecules are minimal.[85] Both H_S and H_D are dependent on appropriately defined diffusive Knudsen numbers (Kn_D) [88]:

$$\mathrm{H}_{S/D} = \frac{4\pi Kn_D^2 + C_1 Kn_D^3 + (8\pi)^{1/2} C_2 Kn_D^4}{1 + C_3 Kn_D + C_4 Kn_D^2 + C_2 Kn_D^3} \tag{3.5a}$$

where C_1 =25.836, C_2 = 11.211, C_3 = 3.502, and C_4 = 7.211. For sorption, the diffusive Knudsen number is expressed as:

$$Kn_{D,S} = \left(\frac{m_v}{k_B T}\right)^{1/2} \frac{2D_v \eta_C}{(d_{g-1} + d_v)\eta_{FM}} \tag{3.5b}$$

which again considers the influence of potential interactions on collisions. For desorption, neglecting potential interactions, the diffusive Knudsen number is defined as:

$$Kn_{D,D} = \left(\frac{m_v}{k_B T}\right)^{1/2} \frac{2D_v}{d_g} \tag{3.5c}$$

Enhancement factors (η_C and η_{FM}) are determined for the ion-dipole potential using the method of Fuchs[89] for the continuum regime and using kinetic theory relationships[87, 90-91] for the free molecular regime, with the approximation that the water dipole is "locked" in alignment during its migration to a particle. This approximation, though it considerably simplifies the analysis, can lead to overestimation of the collision kernel.[91] Comparison to experimental results are hence made both considering and neglecting ion-dipole potential influences (for the latter $\eta_C = \eta_{FM} = 1$). We evaluate both η_C and η_{FM} as functions of Ψ_D, the characteristic ion-dipole potential energy to thermal energy ratio, which is defined as:

$$\Psi_D = \frac{ze\mu_D}{\pi\varepsilon_0 k_b T (d_g + d_v)^2} \tag{3.6}$$

where z is the integer number of charges on the particle (absolute value), μ_D is the vapor molecule dipole moment (1.85 D for water), ε_0 is the permittivity of free space, and the remaining parameters are defined earlier in the text. The continuum regime enhancement factor can be calculated using Fuchs's[89] integral expression as:

$$\eta_C = \left(\int_1^\infty \frac{1}{r^2} \exp\left(\frac{-\Psi_D}{r^2} \right) dr \right)^{-1} = \frac{2\Psi_D^{1/2}}{\pi^{1/2} \operatorname{erf}\left(\Psi_D^{1/2}\right)} \tag{3.7}$$

where "erf" denotes the error function evaluated for the interval $(0,\Psi_D)$. In the free molecular regime, through a combination of conservation of energy and angular momentum, a given vapor molecule's dimensionless initial impact parameter ($b^* = 2b/(d_g+d_v)$), dimensionless distance of closest approach to a particle ($r_m^* = 2r_m/(d_g+d_v)$), Ψ_D, and dimensionless initial speed ($v^* = v\left(\frac{m_v}{2kT}\right)^{1/2}$), can be related to one another as:

$$r_m^* = \left(b^{*2} - \frac{\Psi_D}{v^{*2}} \right)^{1/2} \tag{3.8}$$

If the value of r_m^* either does not exist (condition 1) or is less than unity (condition 2), then the vapor molecule in question, with the prescribed initial speed and impact parameter, will collide with the particle. Condition (1) leads to the criteria for collision that $b^* \leq (\Psi_D/v^{*2})^{1/2}$, while condition (2) leads to $b^* \leq (1+\Psi_D/v^{*2})^{1/2}$. As the latter of these is more inclusive for all possible values of Ψ_D and v_*, the minimum dimensionless impact parameter (b_m^*) for a given v^* is:

$$b_m^* = \left(1 + \frac{\Psi_D}{v^{*2}} \right)^{1/2} \tag{3.9}$$

From b_m^*, following Ouyang et al[87] the free molecular enhancement factor can be calculated as:

$$\eta_{FM} = 2\int_0^\infty b_m^{*2} v^{*3} \exp\left(-v^{*2}\right) dv^* = 2\int_0^\infty \left(v^{*3} + \Psi_D v^*\right) \exp\left(-v^{*2}\right) dv^* = 1 + \Psi_D \qquad (3.10)$$

In the development of Equation (3.10), again, a "locked" dipole has been assumed. Table 3.1 displays values of η_C and η_{FM} for selected Ψ_D values. As is encountered with many other attractive potential functions, $\eta_{FM} > \eta_C$, and strong potential interactions serve to decrease the diffusive Knudsen number.

Table 3.1: A list of continuum and free molecular enhancement factors for the ion-dipole potential as a function of the dimensionless ion-dipole potential energy to thermal energy ratio.

. Ψ_D	η_C	η_{FM}	Ψ_D	η_C	η_{FM}
1.00E-02	1.003334	1.01E+00	1.00E+00	1.339003	2.00E+00
2.00E-02	1.006671	1.02E+00	2.00E+00	1.671838	3.00E+00
3.00E-02	1.01001	1.03E+00	3.00E+00	1.982775	4.00E+00
4.00E-02	1.013351	1.04E+00	4.00E+00	2.267364	5.00E+00
5.00E-02	1.016694	1.05E+00	5.00E+00	2.527088	6.00E+00
6.00E-02	1.020039	1.06E+00	6.00E+00	2.765424	7.00E+00
7.00E-02	1.023386	1.07E+00	7.00E+00	2.985957	8.00E+00
8.00E-02	1.026735	1.08E+00	8.00E+00	3.19174	9.00E+00
9.00E-02	1.030086	1.09E+00	9.00E+00	3.385212	1.00E+01
1.00E-01	1.033439	1.10E+00	1.00E+01	3.568276	1.10E+01
2.00E-01	1.067065	1.20E+00	1.50E+01	4.370194	1.60E+01
3.00E-01	1.100845	1.30E+00	2.00E+01	5.046265	2.10E+01
4.00E-01	1.134747	1.40E+00	2.50E+01	5.641896	2.60E+01
5.00E-01	1.168737	1.50E+00	3.00E+01	6.180387	3.10E+01
6.00E-01	1.202786	1.60E+00	3.50E+01	6.675581	3.60E+01
7.00E-01	1.236865	1.70E+00	4.00E+01	7.136496	4.10E+01
8.00E-01	1.270945	1.80E+00	4.50E+01	7.569398	4.60E+01
9.00E-01	1.304999	1.90E+00	5.00E+01	7.978846	5.10E+01

In classical approaches, the vapor molecule concentration at a nanoparticle surface is commonly expressed in terms of the vapor pressure over a flat liquid surface, n_{sat}, as:

$$\frac{n_s}{n_{sat}} = \exp\left(\frac{-\Delta E}{k_B T}\right) \tag{3.11a}$$

where ΔE is the change in free energy upon desorption of vapor molecule. A number of functional forms[50, 55, 66] have been proposed for ΔE, which can give rise to drastically different expected degrees of heterogeneous uptake for nanoparticles; ΔE values for comparison to measurements can additionally be extracted via the methods of

computational chemistry.[59] For simplicity, we first elect to test the combined Kelvin-Thomson-Raoult (KTR, classical theory) functional form for a singly charged particle, expressed as:

$$\Delta E = -\gamma \frac{\delta A_g}{\delta g} - \frac{e^2}{4\pi\varepsilon_0}\left(1-\frac{1}{\varepsilon_r}\right)\frac{\delta\left(\frac{1}{d_g}\right)}{\delta g} - k_B T \ln a_w \tag{3.11b}$$

where γ is the surface tension of the liquid-air interface, A_g is the surface area of the particle, d_g is the particle diameter, g is the number of vapor molecules bound, ε_0 is the vacuum permittivity, ε_r is the relative permittivity of water, and a_w is the water activity on the surface of the particle. Changes in surface area and in inverse diameter are calculated for discrete changes in g assuming that particles are spheres obeying the following relationships:

$$A_g = \pi\left[\left(d_0^3 + \frac{6}{\pi} g v_m\right)\right]^{2/3} \tag{3.11c}$$

$$d_g = \left[\left(d_0^3 + \frac{6}{\pi} g v_m\right)\right]^{1/3} \tag{3.11d}$$

where v_m is the volume of a liquid phase water molecule. Water activities are evaluated assuming that that particles undergoing heterogeneous uptake are each composed of a soluble central core with an outer saturated solution phase present, until uptake leads to complete dissolution of the core. In instances where a core exists, a_w is taken to be equivalent to the previously noted $a_{w,sat}$ values, and in instances where the core is expected to be dissolved, the activity is equated with the mole fraction of water in

solution (Raoult's Law). The activity of water on a particle, a_w, is determined for particles of known dry diameter, d_0 and number of sorbed vapor molecules, g. First, the combined number of cations and anions, n_{ca} in each dry particle is calculated as:

$$n_{ca} = 2\frac{\rho_{ca}\frac{\pi}{6}d_0^3}{m_{ca}} \tag{3.12}$$

where ρ_{ca} is the bulk density of the cation-anion pair, and m_{ca} is the cation-anion pair mass. With g number of vapor molecules sorbed, the number of cations and anions dissolved in a saturated solution $n_{d,ca}$ is calculated as:

$$n_{d,ca} = 2\frac{gm_{H_2O}}{m_{ca}}\mathrm{X}_{sat} \tag{3.13}$$

where X_{sat} is the mass ratio of the cation-anion pair to water in a saturation solution (which is a function of temperature). If $n_{d,ca} < n_{ca}$, then the activity of water on the particle surface is taken to be equal to the saturated solution activity ($a_w = a_{w,sat}$) for the cation-anion pair under examination. Otherwise, the activity is equated with the mole fraction of water in solution, i.e. a_w is calculated with the equation:

$$a_w = \frac{g}{g + n_{ca}} \tag{3.14}$$

Clearly, this manner of estimating the water activity is approximate; for low amounts of sorbed vapor molecules it is not necessarily appropriate to define the sorbed layer as a saturated solution, and further activities do not "jump" from saturated solution values to ideal mixture values. In defining the free energy of desorption, other researchers have also considered the influence of surface energy at the solid core-solution interface.[60-61, 92] While the surface energy of the solid-liquid interface can significantly affect the

water activity of particles, there is limited experimental data for this parameter, and it is therefore neglected here. Finally, the liquid-air interfacial surface tension is assumed to be that of bulk solution, and free of curvature dependencies.[59] Combining equations (3.3), (3.4), & (3.11a) leads to:

$$K'_g = \frac{\alpha_{g-1}}{\beta_g} = S \exp\left(\frac{\Delta E}{k_B T}\right) \frac{\mathrm{H}_S}{\mathrm{H}_D} \left[\frac{d_{g-1} + d_v}{d_g}\right]^3 \frac{\eta_{FM}^2}{\eta_C} \tag{3.15a}$$

where $K'_g(n_v)$ is a dimensionless reaction parameter, S is the saturation ratio (n_v/n_{sat}; RH/100). Noting that $\Delta G_g = -k_B T \ln(K_{eq,g}) = \Delta H_g - T\Delta S_g$ where ΔG_g, ΔH_g, and ΔS_g are the changes in Gibbs free energy, enthalpy, and entropy for the reaction $n_{g-1} + n_v \Leftrightarrow n_g$, from Equation (3.11b) and (3.15a) ΔH_g and ΔS_g can be defined as:[52]

$$\Delta H_g = \gamma \frac{\delta A_g}{\delta g} + \frac{e^2}{4\pi\varepsilon_0}\left(1 - \frac{1}{\varepsilon_r}\right) \frac{\delta\left(\frac{1}{d_g}\right)}{\delta g} \tag{3.15b}$$

$$\Delta S_g = k_B \left(-\ln a_w + \ln\left(\frac{1}{n_v}\right) + \ln\left[\frac{\mathrm{H}_S}{\mathrm{H}_D}\right] + 3\ln\left[\frac{d_{g-1} + d_v}{d_g}\right] + 2\ln\eta_{FM} - \ln\eta_C \right) \tag{3.15c}$$

We note that in most circumstances wherein classical theories for heterogeneous uptake are invoked, the ratios ($\mathrm{H}_S/\mathrm{H}_D$), $(d_{g-1}+d_v)/d_g$ as well as both enhancement factors, are assumed equal to unity, leading to $\Delta S_g = -k_B(\ln a_w + \ln n_v)$. The inclusion of these terms here is akin to relaxing the assumptions $d_g >> d_v$ and that ion-vapor molecule potential interactions negligibly influence the collision rate. In addition to using classical models, we also compare measurements using a constant value for ΔE.

At equilibrium, the concentration of particles with g vapor molecules sorbed, relative to the concentration which have no bound vapor molecules is expressed as:[93]

$$\frac{n_g}{n_0} = \prod_{i=1}^{g} K'_i \tag{3.16a}$$

With equation (8a), the probability (P_g) that a randomly selected nanoparticle has g vapor molecules sorbed is:

$$P_g = \frac{n_g}{n_0 + \sum_{j=1}^{\infty} n_j} = \frac{\prod_{i=1}^{g} K'_i}{1 + \sum_{j=1}^{\infty} \left(\prod_{i=1}^{j} K'_i \right)} \quad \text{for } g > 0 \tag{3.16b}$$

$$P_g = \frac{n_0}{n_0 + \sum_{j=1}^{\infty} n_j} = \frac{1}{1 + \sum_{j=1}^{\infty} \left(\prod_{i=1}^{j} K'_i \right)} \quad \text{for } g = 0 \tag{3.16c}$$

Water vapor molecules continuously sorb and desorb from a charged particle as it traverses the drift region. Each particle traverses the drift region in a time t_{tot}, and with the linear electric field of magnitude E, the distance L, traversed by the particles is equal to the product of t_{tot}, E and the ion's measured mobility:

$$L = Z_{p,meas} E t_{meas} = \sum_{g=0}^{\infty} Z_{p,g} E t_g \tag{3.17a}$$

where t_g denotes the time an ion spends within the DMA with g vapor molecules bound, and $Z_{p,g}$ is the particles's mobility under the same conditions. Because of the ergodicity of systems in equilibrium, P_g is additionally the fraction of time each nanoparticle spends within the drift region (t_g/t_{meas}) with g sorbed vapor molecules (i.e. each nanoparticle probes the equilibrium distribution of sorbed vapor molecules). Therefore, the average

electrical mobility inferred from measurements of monomobile particles at a prescribed vapor concentration is equal to:

$$Z_{p,RH} = \sum_{g=0}^{\infty} P_g Z_{p,g} \tag{3.17b}$$

Correspondingly, the ratio of the electrical mobility measured at a prescribed relative humidity to the electrical mobility of nanoparticles in the absence of vapor molecules ($Z_{p,0}$) is expressed as:

$$\frac{Z_{p,RH}}{Z_{p,0}} = \sum_{g=0}^{\infty} P_g \left(\frac{Z_{p,g}}{Z_{p,0}} \right) = \frac{1 + \sum_{g=1}^{\infty} \left(\frac{Z_{p,g}}{Z_{p,0}} \prod_{i=1}^{g} K'_i \right)}{1 + \sum_{j=1}^{\infty} \left(\prod_{i=1}^{j} K'_i \right)} \tag{3.17c}$$

For approximately spherical particles, $Z_{p,RH}/Z_{p,0}$ in the free molecular limit is approximately equal to $(GF)_{RH}^{-2}$, and combining Equations (3.1), (3.2), and (3.17b) yields:

$$(GF)_{RH} = \left(\frac{1 + \sum_{j=1}^{\infty} \left(\prod_{i=1}^{j} K'_i \right)}{1 + \sum_{g=1}^{\infty} \left[\left(\frac{d_0 + d_{air}}{d_g + d_{air}} \right)^2 \prod_{i=1}^{g} K'_i \right]} \right)^{1/2} \tag{3.17d}$$

Equations (3.16) & (3.17) are sufficiently general to enable comparison of measured growth factors to any theoretical prediction of $K'_{,i}$ values (i.e. they are independent of Equations (3.4)-(3.15), and further can be employed for any measurement system in which growth factors are inferred from the electrical mobility shifts of free molecular regime spherical particles. However, measurements are limited to instances where $\prod_{i=1}^{g} K'_i \rightarrow 0$ as $g \rightarrow \infty$; otherwise, particles grow without bound. For saturation ratios well

below unity this criterion is typically satisfied, as the product sum of equilibrium constants is proportional to $(S)^g$. A summary of the parameters used in Equation (3.17d) calculations here, which match those during measurements, is provided in Table 3.2.

Table 3.2: Parameters used for calculations performed here

	Lithium Iodide	**Sodium Iodide**
d_0, dry diameters (nm)	3.54, 4.91, 7.59	2.85, 4.24, 5.61
Saturation Ratio Range	0-0.32	0-0.38
Bulk Density, ρ_{ca} (kg m^{-3})	4080	3670
Cation-anion pair mass, m_{ca} (kg mol^{-1})	0.13385	0.14989
$a_{w,sat}$	0.186	0.397
Solubility Mass Ratio, X_{ca}	1.51	1.84
Water molecule diameter (nm)	0.385	0.385
Water Diffusion Coefficient (m^2 s^{-1})	2.68 X 10^{-5}	2.68 X 10^{-5}

Figure 3.4a displays plots of the value *GF-1* from both experiments and theoretical predictions for LiI and NaI particles. Instances where *GF-1* is below unity are not shown. With the exception of initially 3.54 nm diameter lithium iodide particles, the measured GFs are orders of magnitude higher than the predicted GFs, both with and without the ion-dipole potential influence considered. The incorporation of trace amounts of ammonium acetate into particles additionally cannot explain the large disagreement between predictions and measurements, as the ammonium acetate saturated solution activity does not differ substantially from the iodide salts examined (note the activity would need to be significantly lower to bring predictions in agreement with measurements). As emphasized in the introduction, differences between measurements and predictions with classical theory ΔE values are expected; classical predictions are often in stark disagreement with GF measurements for nanometer scale particles.[52]

While the results presented here are for particles in a size range rarely examined, they are qualitatively similar to previous measurement of heterogeneous uptake, in which significantly more sorption has been typically observed than is predicted at low saturation ratios.[62, 94-95] Figure 3.4a also shows that theoretically-predicted GFs begin to increase rapidly at a critical saturation ratio that depends upon particle size, chemical composition, and whether potential interactions influence collisions (most evident for smaller particles). This increase corresponds to the expected onset of deliquescense.[45, 56, 72] Though not clear from Figure 3.4a, more pronounced heterogeneous uptake at a particular RH is evident in Figure 3.3a and Figure 3.3b for both NaI and LiI particles, which may correspond to the onset of deliquescence, though in all instances at RHs well below the expected onset RHs. Figure 3.4b shows the predicted growth factor using constant values for ΔE*=-1e-21, -5e-21, and -10e-21 J* in Equation (3.15a). Although assuming a constant ΔE is not a physically realistic beyond the formation of a monolayer of vapor molecules, Figure 3.4b is provided to illustrate the sensitivity of the degree of vapor uptake to the accuracy of this value. In most cases the critical saturation ratio where rapid growth is observed varies from ~0.05 to ~0.2 for a factor of 5 change in ΔE. Qualitatively the growth curves for LiI particles do not appear to mimic the predicted growth yet for the NaI particles (especially for the larger two sizes) the measured growth curve tends to mimic the general shape of the constant ΔE curve.

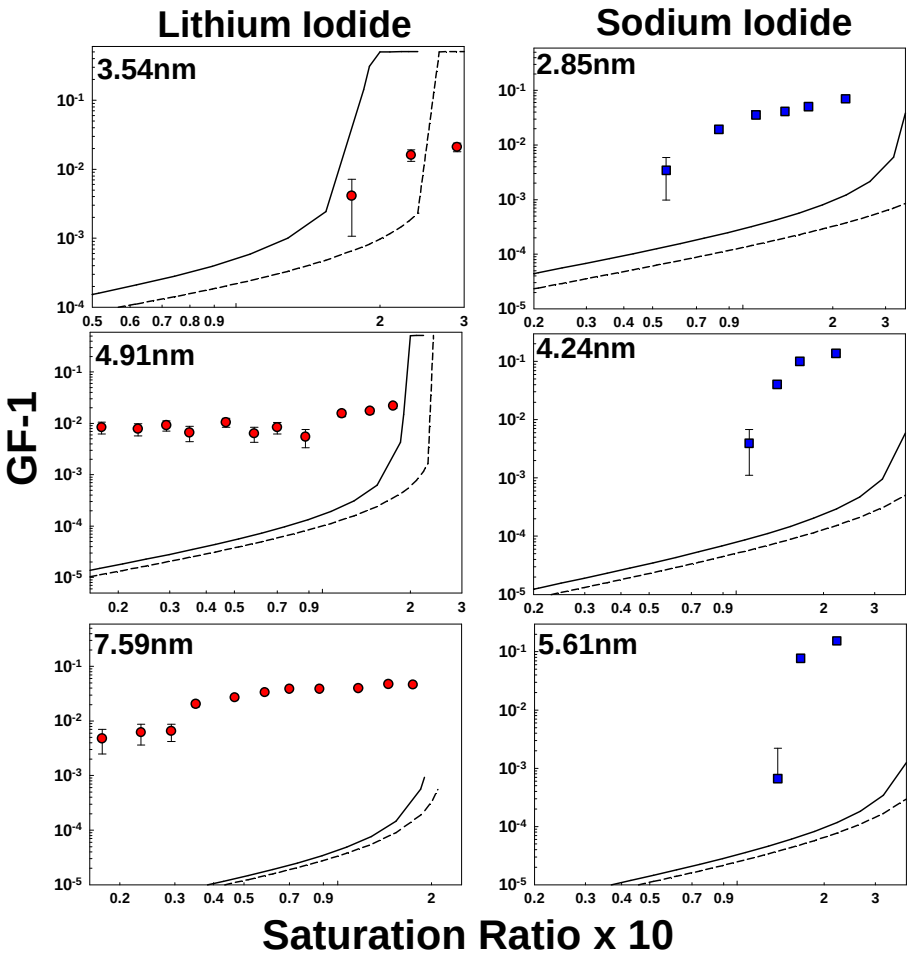

Figure 3.4a: Comparison of measured (colored symbols) to theoretically predicted growth factors considering collision rate enhancement factors based on the ion-dipole potential (solid line) and collision rates calculated without potential interaction influences (dashed line).

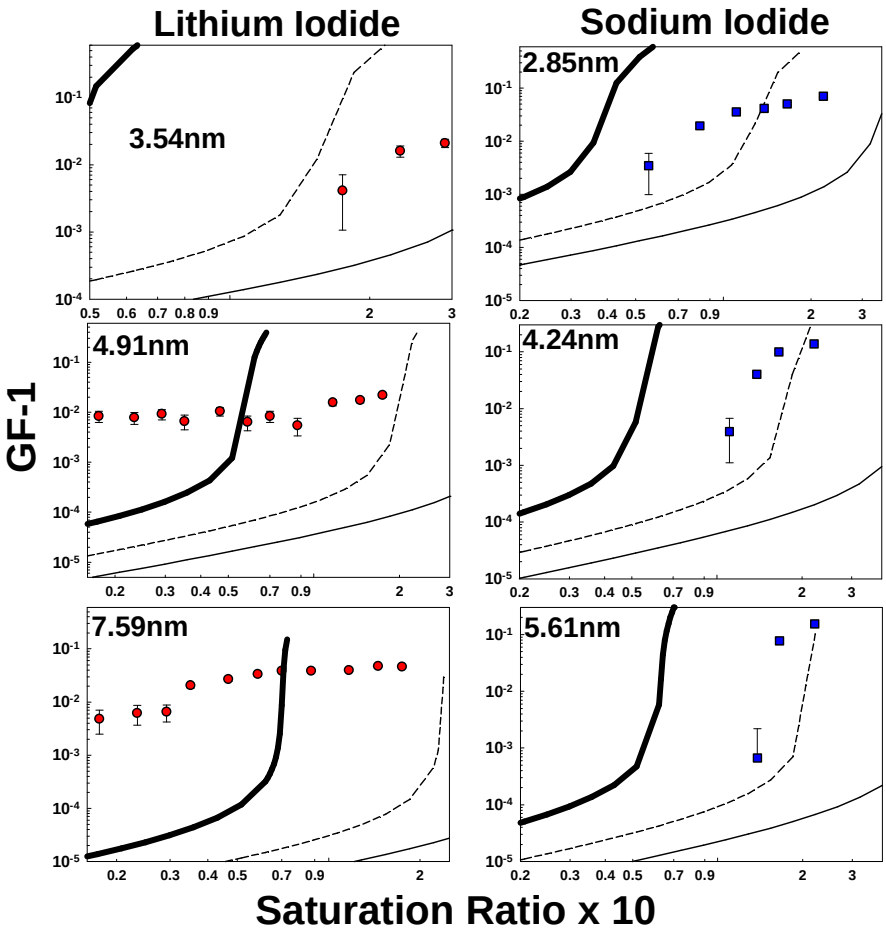

Figure 3.4b: Comparison of theoretically predicted growth factors considering collision rate enhancement factors using constant values of ΔE= -1x10^{-21} thin black line, -5x10^{-21} dashed line, and -10x10^{-21} thick solid line.

Overall, modified classical theory predictions do not agree well with DMA-DTIMS inferred GFs, promoting the need for further experimental and theoretical examination of heterogeneous uptake. Only in instances where theoretical predictions of the Gibbs free energy changes associated with the sorption of successive vapor molecules are extremely accurate will predictions and measurements agree well with one another. This is clear from the functional form of Equation (3.17d); GFs observed via DMA-DTIMS measurement are dependent on the product sum of an exponential of these free

energies. Small disparities between predicted and actual free energy changes, such as the influence of vapor molecule-ion potential interactions or improper estimates of the water activity on the particle surface, can hence substantially alter GFs.

3.3.3 *Growth Factor Precision*

To test theoretical predictions, a system designed to examine heterogeneous uptake via the inference of GFs must enable sufficient measurement precision to detect small changes in particle size. An instrument of perfect (infinite) resolving power gives rise to a delta-function ATD, with a non-zero peak value of $\Delta N_{peak}/\Delta log(t)$ found only at the expected arrival time for the particles in question, and would have infinitely high precision. However, the finite resolution of actual instruments spreads out signal across multiple detection channels, reducing the precision with which the actual peak measurement time can be determined. The precision of the DTIMS is additionally dependent on the peak value of the ATD observed ($\Delta N_{peak}/\Delta log(t)$) and is governed by Poisson (counting) statistics. To explore the counting statistics errors in the DMA-DTIMS system, we determine the standard deviation of the peak arrival time (σ_t). Analogous to the approach utilized by Rader and McMurry [69] to examine the precision of TDMA systems, we apply the Gaussian fitting procedure described in the *Measurement Results* section to randomly generated data sets produced to mimic DMA-DTIMS results. These data sets are generated by first assuming a maximum value for ΔN_{peak} in the range 10-1000. The simulated ATDs are assumed to be Gaussian distributed with normalized full width half maxima of 1/5, based upon the resolving

power of the DTIMS [79]. The total measurement time is assumed to be 5.0 s, with both 150 and 240 time bins (starting at 0.1 s) used to mimic the effect of detector bin widths. The peak arrival time is varied from 1.5-3.5s. Artificial "noise" signal is added to each simulated distribution by multiplying each of the 'ideal' channel counts (ΔN_{ideal}) by the product of a normally distributed random number and the Poisson standard deviation $(\Delta N_{ideal})^{1/2}$. σ_t is calculated as the standard deviation of the peak arrival time over 100 simulated ATDs for each prescribed condition. Figure 3.5 displays values of σ_t/t (where t is the specified peak arrival time) as a function of $\Delta N_{peak}/\Delta log(t)$, which reveals that all simulated results collapse to a single curve, a power law regression to which gives: $\sigma_t/t = 0.6806\,[\Delta N_{peak}/\Delta log(t)]^{-0.545}$ ($R^2 = 0.9949$). To directly assess the influence of instrument precision on GF measurements, we define the standard deviation of the growth factor σ_{GF} as:

$$\sigma_{GF} = \left(\left[\sigma_{Zp^{-1},RH} \frac{dGF}{dZ^{-1}_{p,RH}} \right]^2 + \left[\sigma_{Zp^{-1},0} \frac{dGF}{dZ^{-1}_{p,0}} \right]^2 \right)^{1/2} \tag{3.18a}$$

where $\left(\frac{dGF}{dZ^{-1}_{p,RH}} \right)^2 = \frac{Z_{p,0} Z_{p,RH}}{4}$ and $\left(\frac{dGF}{dZ^{-1}_{p,0}} \right)^2 = \frac{Z^3_{p,0}}{4Z_{p,RH}}$. For the evaluation of dZ_p^{-1} terms, in most experiments it is acceptable to assume that the random errors negligibly impact measured GFs when compared to errors due to counting statistics. We convert the arrival time standard deviation to the standard deviation in the inferred inverse mobility for the peak arrival time, using the dimensionless calibration equation for the DTIMS [79]:

$$\tau = 1.127\,\frac{Pe}{\Psi e} + .0047 \tag{3.18b}$$

where τ is the dimensionless drift time, equivalent to tu_cL^{-1} (u_c is the average counterflow velocity; L is the drift length), and Pe/Ψe is the ratio of the Peclet number to the dimensionless ratio of the electrostatic potential and the thermal energy (equivalent to $u_cLZ_p^{-1}\,V^{-1}$; V is the applied voltage to the DTIMS) [79]. The second term in Equation (3.18a) arises from the finite detector response time. This equation can be rearranged to express the inverse electrical mobility as:

$$Z_p^{-1} = \frac{tV}{1.127\,L^2} - .0047\,\frac{V}{1.127\,u_c L} \tag{3.18c}$$

The standard deviation of Zp^{-1} is defined as:

$$\sigma_{Zp^{-1}} = \frac{\partial Zp^{-1}}{\partial t}\sigma_t \,. \tag{3.18d}$$

This leads to:

$$\sigma_{Zp^{-1}} = \frac{V}{1.127\,L^2}\sigma_t \tag{3.18e}$$

with the assumption that $\Delta N_{peak}/\Delta log(t)$ is equivalent for measurements under both dry and humidified conditions, by combining Equations (3.18a-e), it can be shown that:

$$\frac{\sigma_{GF}}{GF} = \frac{1}{1 - 0.0047\,\dfrac{L}{u_c t_{RH}}}\left(\frac{\sigma_{t,RH}}{2t_{RH}}\left(1 + \left(\frac{t_0}{t_{RH}}\right)^2 GF^4\right)^{1/2}\right) \tag{3.18f}$$

For a drift tube with extremely high counterflow velocity (or with a faster response detector, for which the time-independent term in Equation (3.18f) is negligible), combining Equations (3.18c) and (3.18f) leads to:

$$\frac{\sigma_{GF}}{GF} = \frac{\sigma_{t,RH}}{2^{1/2} t_{RH}} \qquad u_c >> L/t_{RH} \tag{3.18g}$$

Therefore the precision of DMA-DTIMS measurements can be approximated via the σ_t / t regression equation. Using Equation (3.18f) and parameters corresponding to the present DMA-DTIMS system, Figure 3.5 additionally shows calculated values of σ_{GF}/GF for GF values of 1.0, 1.1, and 2.0, with t_0 held constant at 2.5s. For the measurements performed here, the mean σ_{GF}/GF was 0.0024 with a standard deviation of 0.00045. Therefore, under the conditions operated, the DMA-DTIMS system had sufficient precision to distinguish measured GFs from classical predictions, with greater precision achievable via measurement of larger numbers of particles. Moreover, for particles whose diameters are shifted several percent by the sorption of one vapor molecule, with a suitable number of particles counted, DMA-DTIMS measurements have sufficient precision to examine the onset of heterogeneous uptake.

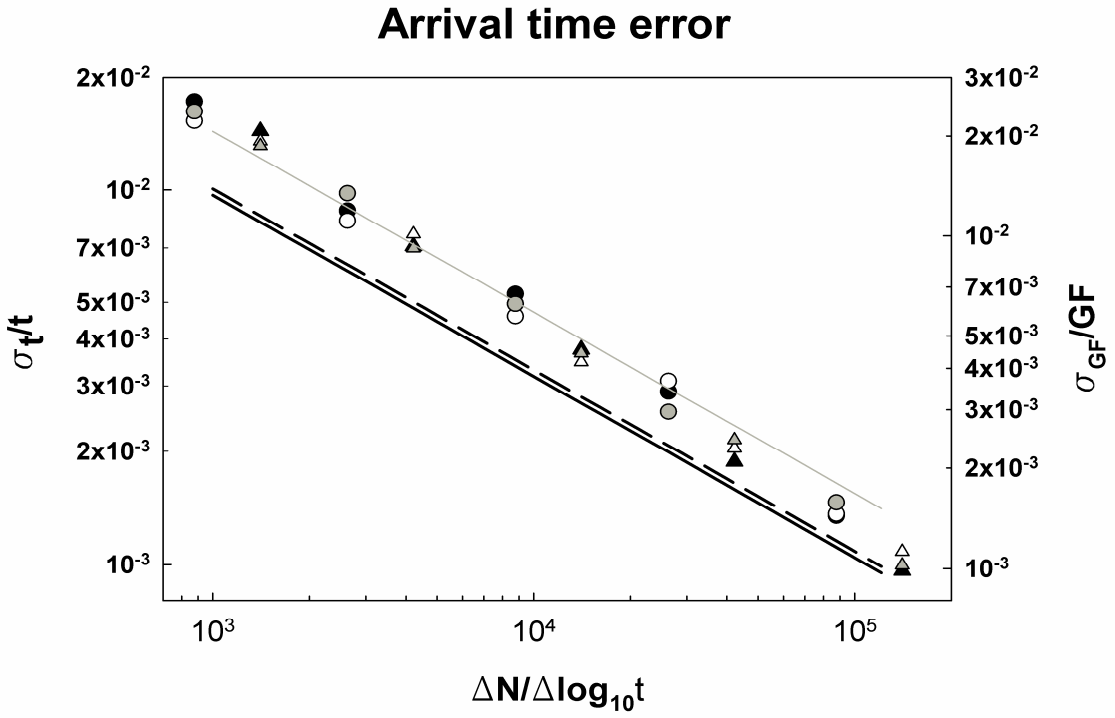

Figure 3.5: The arrival time standard error (symbols) for simulated DTIMS measurements and GF standard error (lines) as a function of $\Delta N_{peak}/\Delta log_{10}t$. Circles represent 150 bins per scan and triangles represent 240 bins/scan. Black symbols, peak arrival time of 1.5s; white: 2.5s; gray: 3.5s. The solid black line represents GF=1, the dashed line is GF=1.1, and the solid gray line is GF=2. For the GF error, the value used for t_0=2.5s.

3.4 Conclusions

A new measurement system for studying the heterogeneous uptake of vapor molecules by aerosol particles, composed of a differential mobility analyzer, drift tube ion mobility spectrometer, and condensation particle counter in series, has been described with demonstrative results. The DMA-DTIMS system facilitates examination of this phenomenon in a size range between 2-10 nm, which is difficult to probe via other existing techniques. A procedure to compare measurements to theoretical predictions of the extent of heterogeneous uptake has also been presented. Using this procedure, measurements reveal that in the relative humidity/saturation ratio range examined,

heterogeneous uptake occurs to a degree much larger than predicted by classical uptake theories. Analysis of simulated distributions shows that the error in the growth factors for the measured data is near 0.24% and that minimum detectable growth factor is a strong function of sample concentration. We propose that continued use of the DMA-DTIMS measurement system will enable greater insight into the heterogeneous uptake process for small particles, particularly by making measurements at variable drift tube temperature, enabling enthalpic and entropic influences on heterogeneous uptake to be distinguished from one another. Further, we propose that the DMA-DTIMS system constructed can be utilized not only in laboratory studies, but also in field environments to study 2-10 nm particles formed during new particle formation events.

Chapter 4 Analysis of Heterogeneous Vapor Uptake by Cluster Ions via Differential Mobility Analysis-Mass Spectrometry (DMA-MS)

4.1 Introduction

In gas phase systems, vapor molecule sorption (heterogeneous uptake) onto ions can, in certain circumstances, control completely the rates of formation and growth of condensed phase entities (molecular clusters and particles in aerosols) [96-98]. Measurement systems can also be developed in which heterogeneous uptake alters the size and structure of chemically distinct ions to varying degrees; this enables instruments which separate ions based upon structure (e.g. low field and high field ion mobility spectrometry) to discriminate between ions which are similar in structure in the absence of vapor molecules, but exhibit varying degrees of uptake [99-100]. To understand both cluster ion growth as well as sorption induced structural shifts, it is necessary to evaluate the equilibrium sorption coefficients (i.e. the ratios of the number concentration of ions with g vapor molecules sorbed to the number concentration with $g-1$ sorbed, at equilibrium, for all $g>0$). In prior studies of vapor molecule sorption onto ions, classical models of uptake, based on either the Kelvin-Thomson model[51, 54, 101], in which the condensed phase is treated as heterogenous bulk matter, or on the Köhler model[57, 61], wherein the ion is treated as a soluble core surounded by a shell of condensed vapor, are utilized to predict equilibrium sorption coefficients. In many instances, classical calculations agree qualitatively with experimental measurements of sorption in systems at equilibrium [53], as well as with measurements of condensed phase entity growth [51,

102-103]. However, there are a series of experimental observations of vapor molecule uptake that are not explained by these models, such as influences of ion chemical composition and polarity [26, 51] as well as quantitative differences in equilibrium sorption coefficients [52]. While modern computational chemistry based approaches can now be used to theoretically study sorption [104-105] without invoking the assumptions of classical approaches, experimental approaches are necessary to better test traditional predictions under a variety of conditions, and to better quantify observed differences between experiments and theory.

As noted, measurement systems have been developed in which ion size and structure alterations due to heterogeneous uptake are quantified. However, existing methods have not clearly established the link between structure/size shifts and equilibrium sorption coefficients for ions in the nanometer size range, under a wide range of vapor molecule concentrations. For example, heterogeneous uptake has been examined with tandem mobility analysis [69, 106] as well as with electrodynamic balances [71]. These methods are usually limited to ions in the > 10 nm size range, and are further insensitive to the addition or loss of a single vapor molecule from the surface of an ion. Conversely single vapor molecule sorption events are detectable in high pressure mass spectrometry (HPMS) systems [52-53]; however, HPMS is limited to vapor concentrations well below saturation, thereby limiting the number of attached vapor molecules that can be measured [53]. Finally, field assisted waveform ion mobility spectrometry-mass spectrometry systems (FAIMS-MS) often exploit differential amounts of heterogeneous uptake between ions migrating at low and high electrostatic field

strengths to distinguish isomers [99-100]. Unfortunately, as operated, existing FAIMS-MS technology does not provide quantitative information on the extent of heterogeneous uptake.

In this chapter we therefore describe a method in which the extent of vapor molecule sorption by chemically identified ions under controlled vapor molecule concentrations is linked to changes in ion size and structure. Specifically, this method involves measurement with a low field Differential Mobility Analyzer - Mass Spectrometer (DMA-MS a form of ion mobility spectrometry-mass spectrometry), wherein the DMA is used to separate and select ions based on their collision cross sections (CCSs). The DMA-MS method is applicable to ions in the ~1 nm size range, and can be used to examine vapor molecule uptake at any vapor molecule concentration up to saturation. In the subsequent sections, the DMA-MS measurement method is described and an equation linking the shift in CCSs inferred from measurements at varying vapor molecule concentrations and equilibrium sorption coefficients for successive vapor molecules is provided. The method is applied to measurements of water vapor molecule uptake by positively charged metal salt ions of the form $(XI)_nX^+$, where X = Cs, Rb, K, or Na and n = 1-13. The observed extents of heterogeneous uptake are compared to classical theory predictions.

4.2 Experimental Methods

4.2.1 *Differential Mobility Analysis-Mass Spectrometry*

To examine uptake, DMA model P5 (SEADM, Boecillo, Spain) was interfaced with a QSTAR XL mass spectrometer (Applied Biosystems) and operated as described

previously for DMA-MS measurements [78, 81], with the specific operational parameters in this study described by Ouyang et al [107]. A schematic of the DMA-MS system is shown in Figure 4.1. Also as in prior studies of cluster ions [32, 76, 108], positively charged cluster ions of cesium, rubidium, potassium, and sodium iodide were produced via positive mode electrospray ionization (ESI) of 10 mM salt solutions in HPLC grade methanol, and ions were directed into the DMA electrostatically against a counterflow of air. Unique from these prior studies, the DMA sheath flow (and correspondingly, the counterflow) was ultra-high purity "zero" air (Airgas) and a custom-made nebulizer was used to introduce controlled amounts of water vapor into the sheath flow. Details of the nebulizer design and a schematic of it are provided in Section 2.2. A chilled-mirror dewpoint hygrometer (General Eastern, Hygro M4) was attached to the chamber in which ESI was performed, and was used in calculating the total water content of the sheath and counterflow air. Finally, to determine the relative humidy/saturation ratio of water vapor in the sheath flow, the sheath flow temperature was measured at the DMA sheath flow inlet using a thermocouple. Using a fan cooled heat exchanger attached to the sheath flow recirculation tubing, the sheath flow was controllable in the 300 – 315 K. The combined water vapor content and temperature control system facilitated DMA based mobility measurements in the saturation ratio (S) range of 0.01 – 0.64, with higher values achievable at lower sheath flow temperatures.

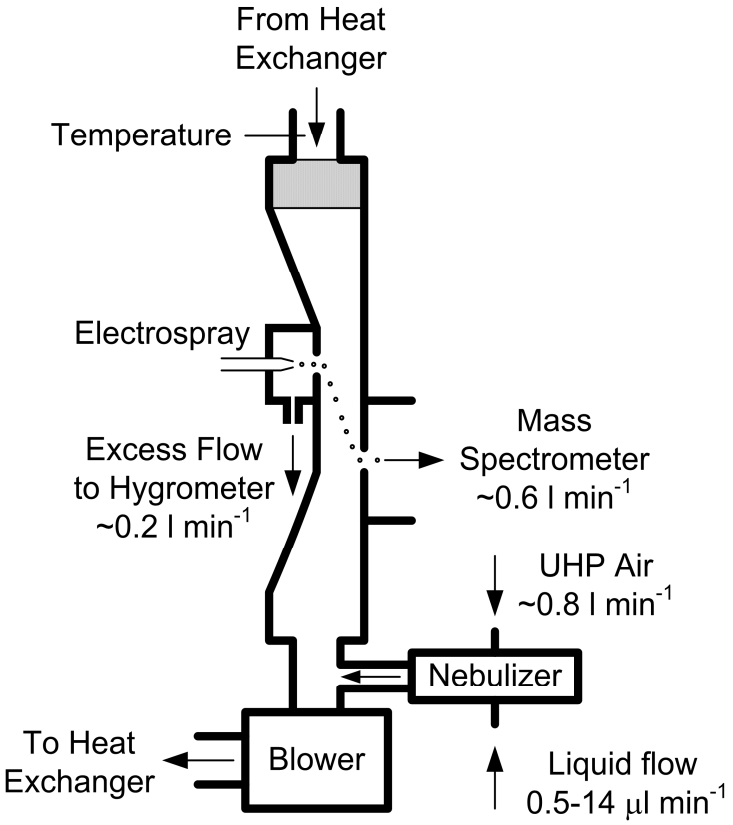

Figure 4.1: DMA-MS Experimental Comnfiguration.

The DMA was calibrated through measurement of a known mobility standard ion [20]. In most prior studies, the ion selected for this purpose was the tetraheptylammonium$^+$ ion. However, at the higher saturation ratios examined, we found that the mobility of the tetraheptylammonium$^+$ ion shifted noticeably, which was indicated by an increase the DMA voltage required to transmit the ion. Further, in the mass spectrometer, ions were detected not only at the expect m/z (410 Da), but also at the *m/z* corresponding to tetraheptylammonium$^+$-H_2O (428 Da) at higher saturation ratios. Therefore, heterogeneous uptake of water molecules may shift the mobility of tetraheptylammonium$^+$ ions, rendering them unsuitable for instrument calibration (1.2% shift in maximal transmission DMA voltage at a saturation ratio of 0.28). We instead

used the tetradodocylammonium$^+$ ion for calibration, in which negligible shift (0.37%) in the DMA voltage required for maximal transmission was observed, and for which water adduct ions were never observed in the mass spectrometer. The inverse mobility ($1/Z_p$) of tetradodecylammonium$^+$ ion at 293 K and near 101 kPa was measured to be 1.401 $cm^2\ V^{-1}\ s^{-1}$ by Ude & Fernandez de la Mora [20]. Its inverse mobility was adjusted to the measurement temperature by multiplying by the factor $(293K/T)^{1/2}$ assuming that it undergoes hard sphere interactions with the background gas molecules. For an ion of this inverse mobility, the influence of gas molecule polarization (the ion induced dipole potential between gas molecules and the cluster ion) is expected to be minimal [76, 107, 109-111].

4.2.2 *Measurement Analysis*

DMA-MS measurements were made by stepping the DMA voltage in 10 V increments from 0 V to 4000 V, and for each applied DMA voltage, a cumulative mass spectrum (over 2 – 10 seconds) was collected using the time-of-flight section of the QSTAR XL. An example of a 2-dimensional m/z – inverse mobility spectrum is shown in Figure 4.2a for CsI cluster ions, measured under zero water vapor (<1 ppm) conditions. Distinct line segments (inset of the Figure 4.2a) are detected at a narrow range of *m/z* values and with DMA resolution (> 50) defined lengths. These segments correspond to specific cluster ions, here we focus on those of the form: $(XI)_nX^+$ (the singly charged ions). Line segments for selected values of *n* are labeled in the plot, and are discernible *n* = 0 to 13 in most instances. Only values of *n = 1 to 13* are examined in this study since

adducts may have transiently associated with bare cations (*n=0*) during DMA measurement, shifting their inferred inverse mobilities (even under 'dry' conditions). Such transient association is evident in spectra from multiple line segments spanning identical inverse mobility ranges to the bare cation, but at multiple *m/z*. From dry condition measurements, the inverse mobility ($1/Z_{p,0}$, where the subscript "0" denotes dry conditions) of each cluster ion is inferred from the point of maximum signal intensity in the cluster ion's line segment. The inverse mobility is then converted to collision cross section (CCS), via the relationship [17]:

$$\frac{1}{Z_{p,0}} = \sqrt{\frac{8k_B T}{\pi m_{air}}} \frac{4\pi\rho}{3ze} \Omega_0 \tag{4.1}$$

where k_B is Boltzmann's constant, T is the temperature, m_{air} is the mass of background gas molecules, ρ is the gas mass density, z is the integer charge on the ion (+1 for all examined ions), e is the unit electron charge, and Ω_0 is the CCS. Under humidified conditions, line segments are also apparent for cluster ions, as evidenced in Figure 4.2b (CsI ions at a water vapor saturation ratio of 0.65). Line segments appear not only at the *m/z* values corresponding to dry cluster ions, but at m/z values for ions of the type $(XI)_n X^+ * (H_2O)_g$ (successive shifts in *g* corresponding to *m/z* shifts of 18 Da, shown in the Figure 4.2b inset). This is indicative of water sorption on cluster ion surfaces. However, the signal intensity distribution for ions of fixed *n* but varying *g* cannot reliably be used to quantify the degree of heterogeneous uptake. At the DMA outlet, ions are transmitted through a region of large pressure drop and high electrostatic gradient. In this region, ions are not in equilibrium with their surroundings [112], and water vapor molecules (also exiting the DMA and transmitted into the mass spectrometer) may condense onto or

evaporate from cluster ions upon exiting the DMA. Both condensation and evaporation of water vapor from cluster ions, facilitated by small changes in mass spectrometer inlet conditions, have been observed by Bush et al [113]. In the DMA, conversely, ions migrate from the upper to lower electrode at low Townsend (Td, the ratio of the electric field strength to the gas number density) levels [76, 78], and are approximately in equilibrium with the surrounding sheath gas. Due to heterogeneous uptake at equilibrium, the cluster ions grow to larger sizes, and the degree of heterogeneous uptake can be quantified through the shift in inverse mobility ($1/Z_{p,S}$) and corresponding CCS (Ω_S, linked to $1/Z_{p,S}$ through an identical relationship to Equation (4.1).

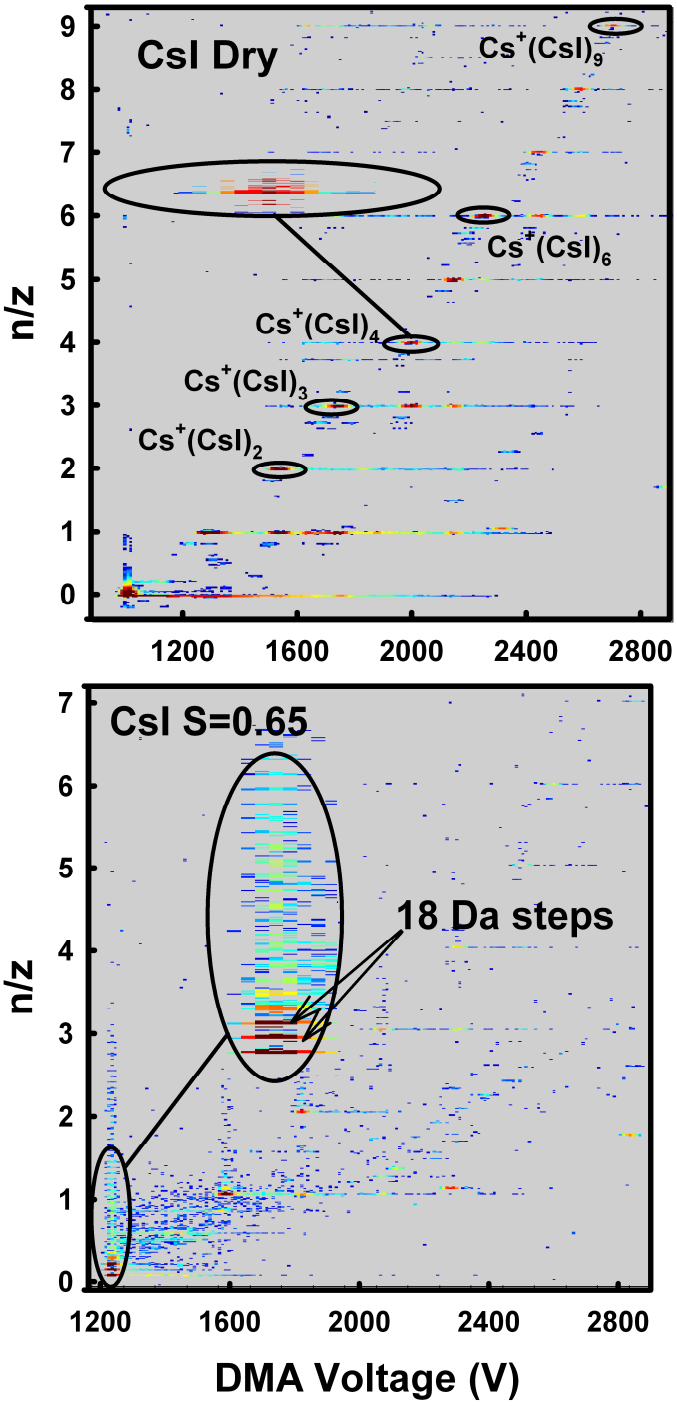

Figure 4.2:Contour plots showing DMA-MS spectra for a) dry conditions and b) at a saturation ratio of 0.65.

Referring again to Equation (3.17b), the ratio $Z_{p,S}/Z_{p,0}$, is expressed as:

$$\frac{Z_{p,S}}{Z_{p,0}} = \sum_{g=0}^{\infty} P_g \left(\frac{Z_{p,g}}{Z_{p,0}} \right) = \frac{1 + \sum_{g=1}^{\infty} \left(\frac{Z_{p,g}}{Z_{p,0}} \prod_{i=1}^{g} K'_i \right)}{1 + \sum_{j=1}^{\infty} \left(\prod_{i=1}^{j} K'_i \right)} \tag{4.2a}$$

Using Equation (4.1) to link mobility and CCS enables Equation (4.2a) to be rewritten as:

$$\frac{\Omega_S}{\Omega_0} = \frac{1 + \sum_{j=1}^{\infty} \left(\prod_{i=1}^{j} K'_i \right)}{1 + \sum_{g=1}^{\infty} \left(\frac{\Omega_g}{\Omega_0} \prod_{i=1}^{g} K'_i \right)} \tag{4.2b}$$

where Ω_g is the CCS of the cluster ion specifically with g vapor molecules bound. Equation (4.2b) therefore facilitates comparison between DMA-MS observed structural modifications to ions and predictions of equilibrium sorption coefficients (from any theoretical model), provided the ratio Ω_0/Ω_g can be estimated for all g.

4.2.3 *Cluster Ion Structure & Collision Cross Section Calculations*

In Chapter 2 we quantified the extent of vapor molecule sorption onto 2 – 7 nm nanoparticles (of LiI and NaI) through a relationship similar to Equation (4.2b). In this chapter we approximated all nanoparticles as spheres, linking the nanoparticle diameters to their mobilities in the manner utilized by Ku & Fernandez de la Mora [114] as well as Larriba et al [32]. While approximating nanoparticles composed of 10^2-10^3 cation-anion pairs as spherical entities is reasonable, the same cannot be stated for clusters where $n \leq 13$ [107]. Here, we instead modeled cluster ion structures using density functional theory (DFT) and subsequently calculated the CCSs of DFT inferred structures. Specifically,

structures for clusters of the type $(XI)_nX^+*(H_2O)_g$ (n = 1-3, g = 0-30) were generated using the Gaussian 09 software package (Gaussian Inc., Wallingford, CT), as described by Ouyang et al [107]. The B3LYP density functional [115] was employed, with the basis set LANL2DZ, which applies Los Alamos ECP (effective core potential) plus DZ (double zeta) [116-118]. Symmetry restrictions were not applied, and vibration frequencies were calculated. All structures evaluated had positive frequencies, indicating they are truly local minima structures rather than transition states.

Complete characterization of clusters requires the determination of the number of local minimum structures and their energy differences [119]. However, here we are only concerned with estimating Ω_g for clusters, as opposed to complete analysis of the entire cluster population. Except in rare circumstances where a cluster has both a linear and compact isomer (only found at $n < 5$), the CCSs calculated (using the procedure noted subsequently) for different isomers differ by only several percent. We therefore base CCS calculations for implementation in Equation (4.2b) on the lowest energy structure obtained.

For CCS calculation we first note that via DMA-MS measurements in air, Ouyang et al [107] found that the CCSs of iodide salt cluster ions are well described the relationship:

$$\Omega = L(\Psi_{pol})\xi PA \tag{4.3a}$$

where PA is the orientationally averaged projected area of a cluster-gas molecule complex, ξ is the momentum scattering coefficient, found to be 1.36 for NaI, 1.27 for KI, 1.23 for RbI, and 1.19 for CsI (depending upon the manner in which gas molecules

impinge and are reemitted from cluster structure surfaces [109-110, 120-121], in which CCSs are determined either through direct examination of the momentum transfer from impinging gas molecules (considering hard sphere interactions between gas molecules and structure atoms, as well as the ion induced dipole potential), and $L(\Psi_{pol})$ is a factor which accounts for the increase in the CCS due to attractive forces between the ion and an induced dipole in the surrounding gas,

$$L \approx 1 + \Psi_{pol}\left(0.322 + \frac{1}{\xi}\left(0.0625 + 0.1212\Psi_{pol}\right)\right), \tag{4.3b}$$

$$\Psi_{pol} = \frac{\pi \alpha_{pol} z^2 e^2}{8\varepsilon_0 P A^2}, \tag{4.3c}$$

where α_{pol} is the gas molecule polarizability. Depictions of DFT calculated structures for clusters with $n = 6$ and with varying numbers of bound water molecules are shown in Figure 4.3. All atoms are depicted as spheres with relative radii proportional to the radii used in CCS calculations: Na (blue): 1.16Å, K(gold): 1.52 Å, Rb (purple): 1.66 Å, Cs (yellow): 1.81 Å, I (green): 2.06 Å, H (white): 1.20 Å, O (red): 1.52 Å, which are in line with the ionic radii for the charged species (cations and anions) and the van der Waals radii for hydrogen and oxygen.

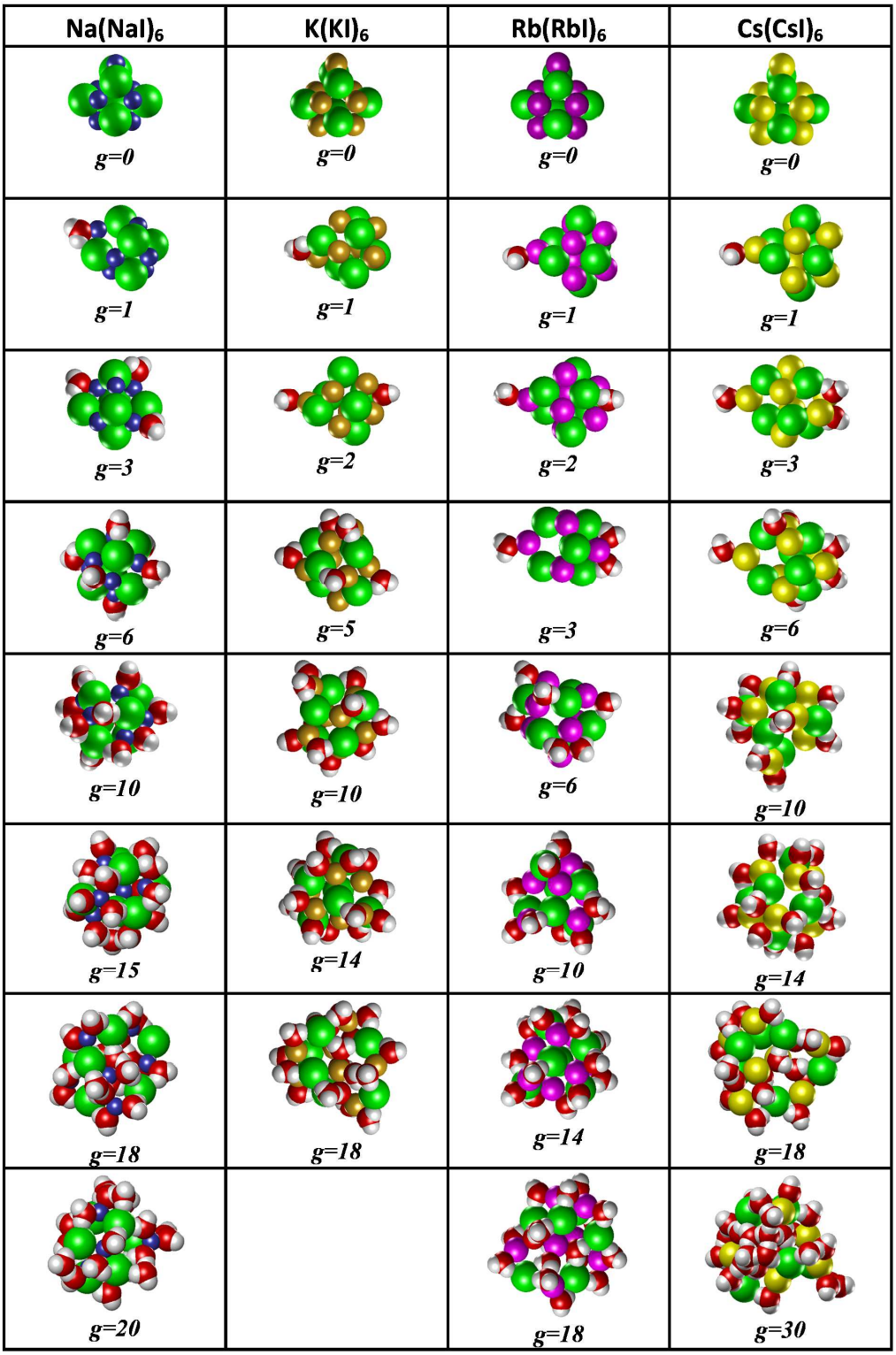

Figure 4.3: Cluster structures found via density functional theory calculations with g sorbed vapor molecules. Water molecules are represented by the red and white atoms and the Iodine is represented with green atoms.

The projected areas of the structures are calculated for the native structures as well as the structures with an added 'probe radius' to account for the size of the impinging molecules (1.5 Å for air and 1.69 Å for water vapor), where the water vapor radius was estimated using the same method employed to find the PAs of the clusters ($r_{Water}=(PA_{Water}/\pi)^{1/2}$). A summary of the calculated PA values is provided in Table 4.1, Table 4.2, and Table 4.3. Values for PAs used in determining Ω_g are found by linear interpolation of the calculated PA data up to the largest calculated cluster *g,max*. Beyond *g.max*, the PAs for successive *g* values are calculated assuming a spherical geometry.using

$$PA_g = \frac{\pi}{4}\left[\left(\frac{4PA_{g,\max}}{\pi}\right)^{3/2} + \frac{6}{\pi}(g-g,\max)v_w\right]^{2/3}, \tag{4.4}$$

where v_w is the volume of the condensed phase vapor molecule. Plots of Ω_g/Ω_0 for select clusters are shown in Figure 4.4, where the data points indicate the calculated values.

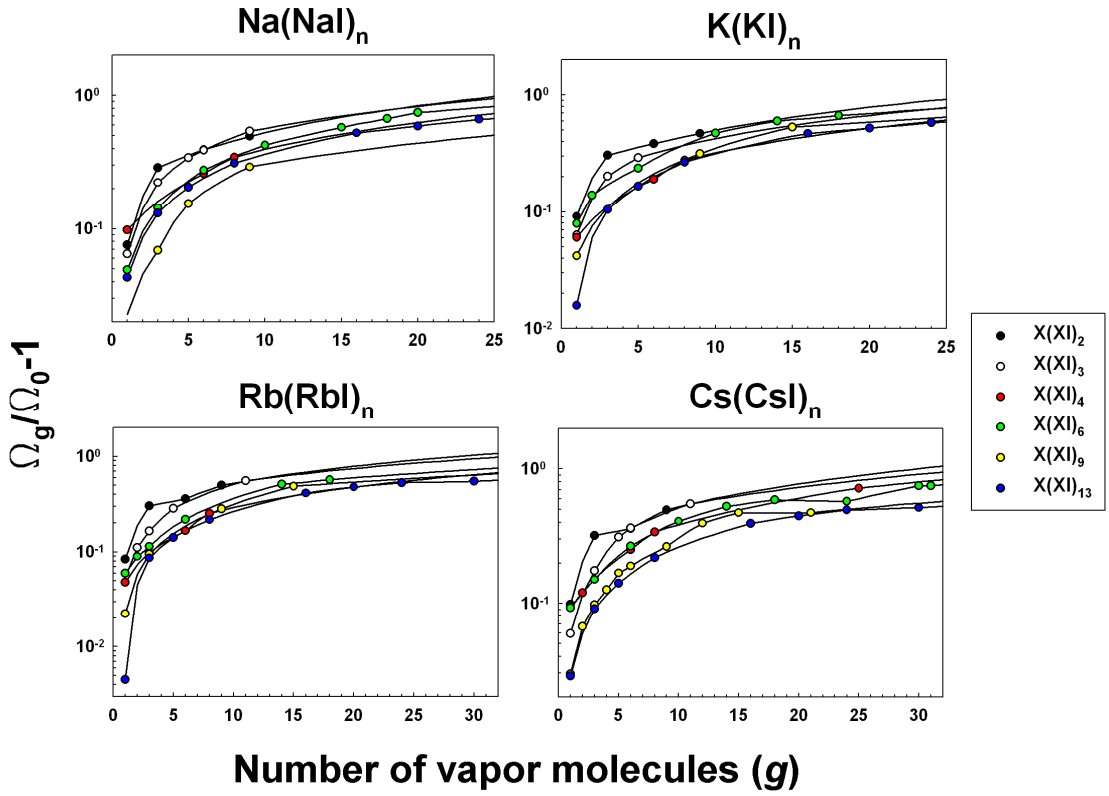

Figure 4.4: Ratio of collision cross sections found by orientation averaged projected area measurements of the simulated cluster structures. Circles represent simulated structures. Line segments between these structures are generated by linear interpolation. Beyond the largest modeled structure the CCS ratio is determined geometrically using the volume of a water molecule.

4.3 Results & Discussion

4.3.1 *Experimental Results*

Figure 4.5 shows the measured values for Ω_s/Ω_0 for select clusters. Values of Ω_s/Ω_0 for all of the clusters are provided in Table 4.4, Table 4.5, and Table 4.6. Evident in the figure, the growth of clusters varies with the number of neutral pairs although not monotonically. Additionally, the relative growth between clusters varies for the different core salts. For $Na^+(NaI)_{13}$ a rapid increase in vapor uptake is observed at a saturation ratio near S=0.1 which was similarily observed in measurements presented in Chapter 2.

This behavior for NaI compared to the other salts is likely due to its relatively low saturated water activity a_w. It is interesting to note that this behavior is not observed for the other clusters of NaI. For the other salts, the $X^+(XI)_{13}$ ions shown consistently less growth compared to the other clusters. This is possibly due to the rock salt crystal structure expected for 13 neutral pairs (3 molecule * 3 molecule cube) being more resistant to assimilating a water vapor molecule.

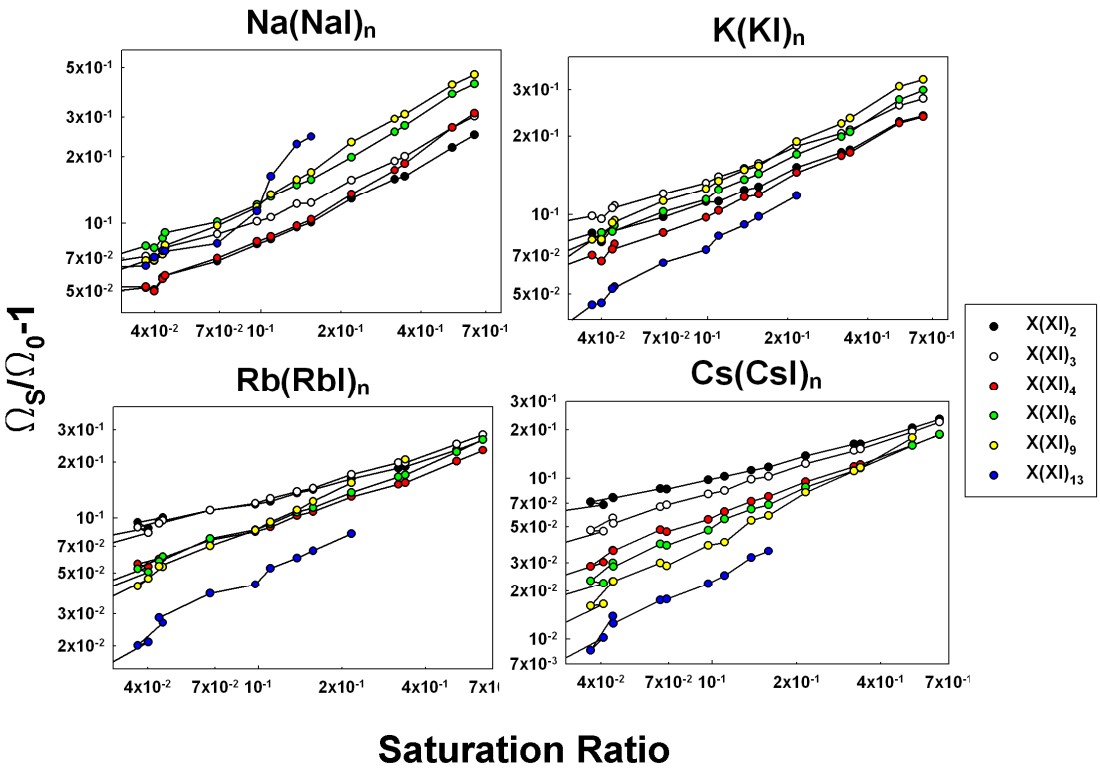

Figure 4.5: Raw measured data for select clusters with *n* neutral pairs of 2, 3, 4, 6, and 9. All data were taken at gas temperature of ~ 27°C. Ions with greater numbers of neutral pairs were not detected at the highest saturation ratios.

The peak CCS ratio for NaI was measured at Ω_S/Ω_0=1.25 at S=0.15. To compare this value to measurements made for NaI with the system described in Chapter 3 we approximate the CCS ratio as (Growth Factor)^2. For $Na(NaI_{13})$ with an approximate diameter of 1.2 nm, the measured growth factor using the HRDMA-MS was 1.12.

Comparatively for the 2.56 nm NaI particles measured with the HRDMA-DTIMS system, the growth factor was 1.05 at S=0.16.

4.3.2 *Comparison to Classical (KTR) Predictions*

Prior authors have created and tested heterogeneous uptake models which invariably treat the cluster as a sphere and apply bulk properties to determine its geometric and physical properties. Using Equation (4.2b) and calculated values for Ω_g/Ω_0, the predicted value for Ω_s/Ω_0 is solely dependent on the values used for the equilibrium parameter K'_g. This flexibility allows for application of computationally determined values as well as equilibrium constants calculated using bulk models. Recalling the derivation presented in Chapter 2, the values for K'_g can be estimated using

$$K'_g = \frac{\alpha_{g-1}}{\beta_g} = S \exp\left(\frac{\Delta E}{k_B T}\right)\frac{H_S}{H_D}\left[\frac{d_{g-1}+d_v}{d_g}\right]^3 \frac{\eta_{FM}^2}{\eta_C}, \tag{4.5}$$

where S is the saturation ratio (n_v/n_{sat}; RH/100), ΔE is the energy change upon sorption of one vapor molecule, H_S and H_D are the collision kernel constants for sorption and desorption, and η_{FM} and η_c are enhancement factors in the free molecular and continuum regimes. The values for $d_{g-1} + d_v$ and d_g are found using their respective calculated PAs with the appropriate probe radii. The value for ΔE can be estimated by applying bulk thermodynamic principles using the Kelvin-Thomson-Raoult model given by

$$\Delta E = -\gamma \frac{\delta A_g}{\delta g} - \frac{e^2}{4\pi\varepsilon_0}\left(1-\frac{1}{\varepsilon_r}\right)\frac{\delta\left(\frac{1}{d_g}\right)}{\delta g} - k_B T \ln a_w, \tag{4.6}$$

where γ is the surface tension of the liquid-air interface, A_g is the surface area of the particle, d_g is the particle diameter, g is the number of vapor molecules bound, ε_0 is the vacuum permittivity, ε_r is the relative permittivity of water, and a_w is the water activity on the surface of the particle where the values for water activity a_w were determined using the same technique described in Chapter 3 using $a_{w,sat}$ of 0.382 for NaI and 0.69 for KI and Cs and Rb clusters treated as ideal solutions. This approach is certainly flawed as it does not account for surface sorption energies for the first several vapor molecules. Additionally the model assumes that properties such as surface tension water activity are constant at nanoscale sizes. Despite these flaws we compare the predicted growth to the measured growth, shown in Figure 4.6, to illustrate the application of this technique. The model over predicts the onset of growth for the smallest clusters and under predicts it for the larger ones. In all cases the model over predicts the total growth. The measured growth as well as the predicted growth using the KTR model varies widely for the different cluster materials. For the measured data this variation increases with increasing numbers of neutral pairs. This is likely due to the varying water activities and solubility mass ratios for the different materials having a larger effect on the growth. Similar to the comparison made in Chapter 3, growth predictions using a fixed value for ΔE are also shown in Figure 4.6 for ΔE=*-1E-21* and *-10E-21J*. While the KTR model predicts a point of rapid vapor uptake for all of the ions, it is only observed for $Na(NaI)_{13}$. Alternately the predictions using a constant ΔE does not predict rapid uptake in the measurement range.

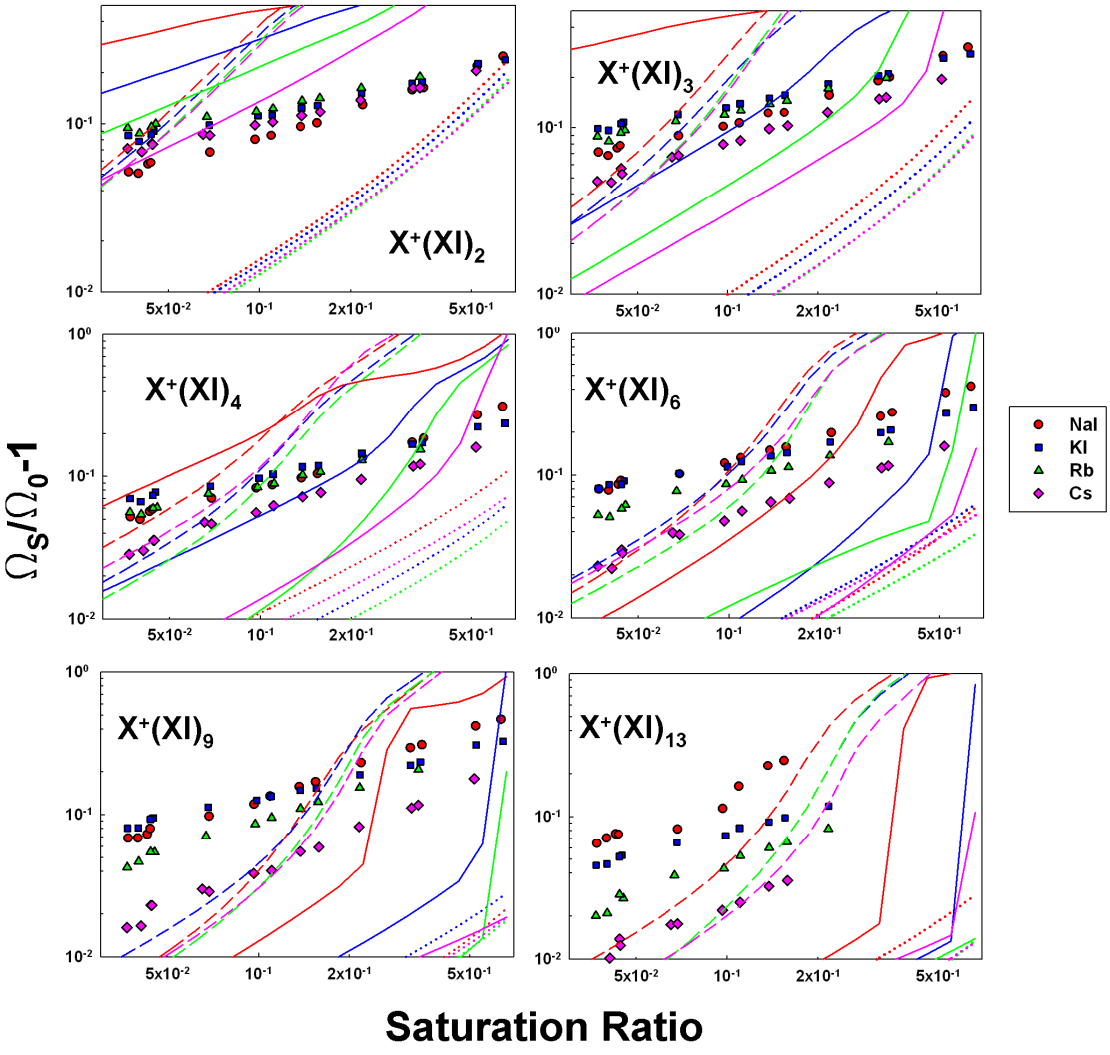

Figure 4.6:: Comparison of measurements to model results. Measured results are shown as data points, the KTR model results using the corresponding colored lines. The dotted lines represent ΔE = -1x10^{-21} and the dashed lines represent ΔE = -1x10^{-20}

4.4 Conclusions

We have presented a system for measuring heterogeneous vapor uptake by electrospray generated ions ranging in size from single molecules up to clusters containing 27 molecules (~1.5nm). We showed how molecular structures calculated using density functional theory can be used to calculate the collision cross section of a cluster upon

uptake of various numbers of vapor molecules where the values of these calculated CCSs can be inserted into a general model which predicts the proportional change in the collision cross section due to heterogeneous vapor uptake with increasing vapor concentration. We demonstrated this model using sorption and desorption rates based on collision rates between the ions and surrounding vapor molecules as well as the thermodynamic contributions estimated using both a Kelvin-Thomson-Raoult model and a constant value. Comparison of the measured data to the models shows how the commonly employed theoretical models are not appropriate for predicting vapor uptake by ions in this size range. In the future, values for ΔE determined using computational chemistry techniques will be used in the uptake model and the predicted change in collision cross section will be compared to the measured data presented in this chapter,

Table 4.1: PA values using air as a probe radius

Na(NaI)x

x=	0		1		2		3		4		5		6		7		8		9		10		11		12		13	
	# g	PA (Å²)	# g	PA (Å²)	# g	PA (Å²)	# g	PA (Å²)	# g	PA (Å²)	# g	PA (Å²)	# g	PA (Å²)	# g	PA (Å²)	# g	PA (Å²)	# g	PA (Å²)	# g	PA (Å²)	# g	PA (Å²)	# g	PA (Å²)	# g	PA (Å²)
	0	21.6	0	52.4	0	70.7	0	89.3	0	107.3	0	116.9	0	129.6	0	142.6	0	155.4	0	169.2	0	177.6	0	181.6	0	190.6	0	187.8
	2	56.4	1	69.9	1	84.6	1	99.1	1	122.0	1	126.6	1	137.6	1	153.5	1	161.5	3	182.4	1	184.9	1	191.5	1	198.5	1	196.8
	3	68.8	2	86.9	3	112.9	3	120.7	6	144.7	3	145.1	3	152.7	3	169.6	3	176.3	5	198.7	3	202.2	2	202.4	3	215.0	3	215.0
	5	88.5	3	96.9	6	125.4	5	135.9	8	156.7	5	161.6	6	173.1	5	183.8	4	184.2	9	224.6	5	216.4	3	208.0	5	231.3	5	230.3
	15	140.9	5	109.7	9	136.9	6	141.9			10	184.9	10	196.0	6	191.4	8	214.3			10	247.7	5	223.7	12	282.7	8	251.8
	25	177.0					9	160.2			15	195.3	15	218.9	8	203.0					16	276.2	8	246.4	15	298.2	16	294.9
													18	233.0													20	308.2
													20	243.6													24	322.9

K(KI)x

x=	0		1		2		3		4		5		6		7		8		9		10		11		12		13	
	# g	PA (Å²)	# g	PA (Å²)	# g	PA (Å²)	# g	PA (Å²)	# g	PA (Å²)	# g	PA (Å²)	# g	PA (Å²)	# g	PA (Å²)	# g	PA (Å²)	# g	PA (Å²)	# g	PA (Å²)	# g	PA (Å²)	# g	PA (Å²)	# g	PA (Å²)
	0	28.7	0	62.0	0	81.4	0	101.1	0	125.6	0	132.9	0	139.5	0	154.6	0	174.1	0	177.1	0	198.5	0	209.6	0	212.9	0	216.6
	1	44.4	1	79.2	1	95.8	1	110.7	1	135.3	1	142.2	1	152.9	1	162.5	1	182.5	1	185.4	1	207.7	1	217.4	1	224.1	1	220.2
	3	73.9			3	124.2	3	130.3	6	155.7	3	159.2	2	162.8	3	176.1	3	197.3	9	239.0	3	226.3	2	227.9	3	239.5	3	241.0
	5	94.9			6	133.6	5	142.5	8	168.9	5	173.6	5	179.0	12	219.2	4	204.8	15	280.5	5	239.4	3	235.3	5	256.8	5	255.3
	15	145.9			9	143.9					10	206.7	10	216.8			8	233.0			10	272.9	5	251.2	12	304.7	8	278.3
	25	178.9									15	209.6	14	236.9							16	301.8	8	271.4	15	320.4	16	325.0
													18	247.2											20	322.1	20	336.6

Rb(RbI)x

x=	0		1		2		3		4		5		6		7		8		9		10		11		12		13	
	# g	PA (Å²)	# g	PA (Å²)	# g	PA (Å²)	# g	PA (Å²)	# g	PA (Å²)	# g	PA (Å²)	# g	PA (Å²)	# g	PA (Å²)	# g	PA (Å²)	# g	PA (Å²)	# g	PA (Å²)	# g	PA (Å²)	# g	PA (Å²)	# g	PA (Å²)
	0	31.4	0	69.6	0	88.5	0	109.4	0	135.4	0	143.8	0	156.9	0	165.2	0	187.4	0	192.3	0	216.4	0	228.7	0	231.9	0	235.3
	1	47.1	1	82.7	1	101.4	2	126.2	1	143.4	1	155.7	1	167.7	1	172.1	24	313.6	1	197.1	1	222.0	17	322.3	1	239.3	1	236.5
	3	76.4	2	95.9	3	130.7	3	134.1	3	151.6	2	171.3	2	173.2	3	184.2			3	212.3	3	238.7			3	254.4	3	257.0
	5	99.4			6	137.7	5	151.1	6	162.7	5	190.8	3	177.6	12	229.8			9	251.3	5	253.4			5	269.9	5	270.7
	15	147.4			9	154.6	11	187.7	8	176.7	10	214.6	6	196.2					9	251.3	16	316.6			5	270.8	8	289.5
	25	181.5									15	216.7	14	247.2					15	293.8					12	320.2	16	337.9
											18	235.0	18	257.5											15	334.9	20	354.0
																									20	340.1	24	367.3
																									24	343.7	30	371.0
																									30	364.1		

Cs(CsI)x

x=	0		1		2		3		4		5		6		7		8		9		10		11		12		13	
	# g	PA (Å²)	# g	PA (Å²)	# g	PA (Å²)	# g	PA (Å²)	# g	PA (Å²)	# g	PA (Å²)	# g	PA (Å²)	# g	PA (Å²)	# g	PA (Å²)	# g	PA (Å²)	# g	PA (Å²)	# g	PA (Å²)	# g	PA (Å²)	# g	PA (Å²)
	0	37.8	0	73.2	0	93.7	0	116.7	0	131.5	0	154.4	0	163.7	0	178.8	0	201.8	0	206.4	0	231.6	0	243.3	0	249.7	0	253.3
	1	50.1	1	88.2	1	108.5	1	126.0	1	146.7	1	158.4	1	181.1	1	180.5	1	208.5	1	213.1	1	241.5	1	255.4	1	258.2	1	261.0
	2	65.3	2	101.4	3	138.4	3	143.5	2	151.1	2	183.3	3	191.8	3	194.5	24	328.7	2	221.4	3	254.9	2	260.3	3	273.4	3	277.6
	3	79.4			6	143.5	5	163.4	6	171.7	5	204.6	6	213.0	12	242.4	30	314.7	3	228.4	5	270.8	17	340.5	5	289.5	5	291.1
	5	103.4			9	160.8	6	170.7	8	185.7	10	227.5	10	238.8	21	282.2			4	234.8	6	278.0			12	341.3	8	311.5
	15	150.4					11	197.2	25	243.4	15	224.9	14	260.1					5	244.1	10	302.5			15	354.5	16	357.4
											18	243.4	18	271.4					6	248.9	16	332.8			20	361.0	20	372.4
											25	267.6	24	268.3					9	265.3					24	360.6	24	384.4
													30	299.9					12	294.0					30	380.2	30	389.8
													31	300.1					15	311.1								
																			21	311.1								

Table 4.2: PA values using water as a probe radius

Na(NaI)x

x=	0		1		2		3		4		5		6		7		8		9		10		11		12		13	
	#g	PA (Å²)	#g	PA (Å²)	#g	PA (Å²)	#g	PA (Å²)	#g	PA (Å²)	#g	PA (Å²)	#g	PA (Å²)	#g	PA (Å²)	#g	PA (Å²)	#g	PA (Å²)	#g	PA (Å²)	#g	PA (Å²)	#g	PA (Å²)	#g	PA (Å²)
	0	0.0	0	56.8	0	87.2	0	93.2	0	112.6	0	121.5	0	132.7	0	148.1	0	159.1	0	170.8	0	179.4	0	188.1	0	191.9	0	193.5
	2	61.2	1	75.6	1	90.8	1	104.7	1	128.2	1	134.4	1	143.6	1	159.3	1	167.6	3	191.2	1	190.9	1	198.4	1	206.4	1	204.2
	3	74.2	2	92.9	3	120.4	3	126.5	6	151.8	3	151.9	3	159.1	3	178.4	3	185.3	5	208.7	3	210.4	2	210.0	3	224.4	3	239.9
	5	95.4	3	103.7	6	133.4	5	143.0	8	164.7	5	169.5	6	183.3	5	192.7	4	193.8	9	236.3	5	227.8	3	217.3	5	241.4	5	265.5
	15	149.6	5	116.8	9	144.5	6	150.8			10	195.9	10	206.3	6	201.2	8	223.6			10	259.8	5	235.5	12	294.3	8	307.4
	25	185.6					9	168.8			15	205.1	15	229.3	8	213.2					16	291.0	8	257.9	15	309.8	16	321.0
													18	242.4													20	320.3
													20	256.4													24	337.9

K(KI)x

x=	0		1		2		3		4		5		6		7		8		9		10		11		12		13	
	#g	PA (Å²)	#g	PA (Å²)	#g	PA (Å²)	#g	PA (Å²)	#g	PA (Å²)	#g	PA (Å²)	#g	PA (Å²)	#g	PA (Å²)	#g	PA (Å²)	#g	PA (Å²)	#g	PA (Å²)	#g	PA (Å²)	#g	PA (Å²)	#g	PA (Å²)
	0	0.0	0	67.4	0	87.1	0	108.3	0	131.7	0	140.2	0	149.3	0	162.1	0	182.3	0	185.7	0	207.1	0	219.1	0	221.4	0	224.0
	1	48.8	1	84.9	1	102.4	1	117.3	1	142.3	1	149.9	1	161.9	1	170.5	1	190.3	1	193.0	1	216.9	1	226.9	1	232.9	1	230.1
	3	79.7			3	132.3	3	136.4	6	164.2	3	169.9	2	171.4	3	185.1	3	207.3	9	249.6	3	234.7	2	238.2	3	248.4	3	249.9
	5	102.6			6	141.4	5	153.2	8	178.3	5	183.6	5	187.7	12	230.3	4	215.8	15	292.5	5	251.3	3	246.0	5	267.6	5	267.1
	15	154.3			9	152.3					10	218.2	10	227.5			8	245.5			10	283.8	5	261.4	12	318.1	8	291.5
	25	189.7									15	220.9	14	248.2							16	315.2	8	282.7	15	332.4	16	339.0
													18	258.6											20	335.5	20	351.2

Rb(RbI)x

x=	0		1		2		3		4		5		6		7		8		9		10		11		12		13	
	#g	PA (Å²)	#g	PA (Å²)	#g	PA (Å²)	#g	PA (Å²)	#g	PA (Å²)	#g	PA (Å²)	#g	PA (Å²)	#g	PA (Å²)	#g	PA (Å²)	#g	PA (Å²)	#g	PA (Å²)	#g	PA (Å²)	#g	PA (Å²)	#g	PA (Å²)
	0	0.0	0	72.5	0	92.7	0	115.1	0	133.7	0	150.2	0	176.4	0	172.3	0	195.1	0	198.4	0	225.8	0	235.4	0	239.8	0	242.9
	1	51.4	1	89.9	1	108.3	2	134.0	1	151.3	1	164.9	1	182.4	1	180.4	24	324.4	1	206.7	1	231.6	17	337.2	1	247.8	1	246.7
	3	83.0	2	102.6	3	139.2	3	143.5	3	161.7	2	182.1	2	187.0	3	191.9			3	223.3	3	247.4			3	264.7	3	265.8
	5	106.8			6	146.1	5	160.8	6	171.5	5	202.8	3	206.4	12	240.8			9	263.6	5	265.0			5	283.4	5	282.9
	15	156.5			9	163.6	11	197.9	8	185.4	10	228.1	6	237.6					15	307.5	16	331.0			12	334.6	8	301.1
	25	191.5									15	226.8	14	259.3					0	0.0					15	349.6	16	351.5
											18	244.7	18	269.9											20	354.3	20	367.7
																									24	356.5	24	381.2
																									30	378.8	30	383.1
																									0	0.0		

Cs(CsI)x

x=	0		1		2		3		4		5		6		7		8		9		10		11		12		13	
	#g	PA (Å²)	#g	PA (Å²)	#g	PA (Å²)	#g	PA (Å²)	#g	PA (Å²)	#g	PA (Å²)	#g	PA (Å²)	#g	PA (Å²)	#g	PA (Å²)	#g	PA (Å²)	#g	PA (Å²)	#g	PA (Å²)	#g	PA (Å²)	#g	PA (Å²)
	0	0.0	0	79.5	0	100.0	0	124.6	0	139.7	0	161.9	0	176.0	0	188.9	0	209.3	0	214.9	0	244.4	0	254.6	0	260.3	0	262.5
	1	54.9	1	96.4	1	115.3	1	134.1	1	154.6	1	168.9	1	190.4	1	189.6	1	218.2	1	222.8	1	252.2	1	266.5	1	267.4	1	270.8
	2	71.1	2	108.0	3	147.4	3	149.4	2	159.4	2	192.5	3	200.0	3	203.6	0	0.0	2	230.8	3	268.8	2	269.3	3	286.3	3	286.8
	3	86.1			6	152.0	5	173.9	6	181.3	5	213.1	6	223.4	12	253.9	30	328.0	3	237.9	5	281.8	17	353.8	5	303.1	5	302.7
	5	110.4			9	168.7	6	179.9	8	196.4	10	237.3	10	248.8	21	294.2			4	246.1	6	289.2			12	352.4	8	324.5
	15	159.7					11	207.3	25	253.3	15	235.7	14	272.9					5	253.7	10	316.5			15	367.6	16	371.1
											18	254.2	18	283.8					6	260.0	16	344.7			20	377.0	20	386.8
											25	282.5	24	280.9					9	276.8					24	376.1	24	398.5
													30	313.2					12	307.0					30	394.0	30	406.0
													31	312.3					15	322.4								
																			21	322.9								

Table 4.3: PA values using a zero probe radius

Na(NaI)x

x=	0		1		2		3		4		5		6		7		8		9		10		11		12		13	
	#g	PA (Å²)	#g	PA (Å²)	#g	PA (Å²)	#g	PA (Å²)	#g	PA (Å²)	#g	PA (Å²)	#g	PA (Å²)	#g	PA (Å²)	#g	PA (Å²)	#g	PA (Å²)	#g	PA (Å²)	#g	PA (Å²)	#g	PA (Å²)	#g	PA (Å²)
	0	0.0	0	18.0	0	32.2	0	41.7	0	54.8	0	60.0	0	67.9	0	78.8	0	86.6	0	94.8	0	101.3	0	108.2	0	111.6	0	114.8
	2	19.6	1	25.8	1	36.9	1	46.4	1	58.0	1	66.3	1	73.9	1	85.5	1	91.4	3	106.2	1	107.0	1	115.3	1	119.0	1	120.6
	3	26.5	2	33.4	3	50.8	3	60.2	6	78.0	3	76.9	3	83.8	3	95.2	3	101.6	5	115.5	3	118.2	2	120.3	3	129.5	3	131.8
	5	37.6	3	40.5	6	63.5	5	70.5	8	86.1	5	87.5	6	98.2	5	104.4	4	106.9	9	134.6	5	129.7	3	125.3	5	140.3	5	142.0
	15	73.7	5	49.6	9	71.6	6	74.1			10	106.4	10	114.1	6	109.4	8	126.4			10	148.5	5	134.9	12	176.1	8	155.4
	25	101.8					9	87.6			15	115.1	15	131.4	8	117.5					16	172.9	8	147.9	15	186.5	16	187.0
													18	140.9													20	198.9
													20	150.5													24	212.2

K(KI)x

x=	0		1		2		3		4		5		6		7		8		9		10		11		12		13	
	#g	PA (Å²)	#g	PA (Å²)	#g	PA (Å²)	#g	PA (Å²)	#g	PA (Å²)	#g	PA (Å²)	#g	PA (Å²)	#g	PA (Å²)	#g	PA (Å²)	#g	PA (Å²)	#g	PA (Å²)	#g	PA (Å²)	#g	PA (Å²)	#g	PA (Å²)
	0	0.0	0	23.8	0	36.9	0	49.5	0	65.5	0	72.2	0	80.4	0	88.9	0	103.0	0	107.2	0	120.5	0	130.6	0	133.5	0	138.1
	1	14.5	1	31.3	1	43.8	1	55.6	1	67.9	1	77.4	1	87.4	1	93.9	1	108.0	1	111.8	1	126.3	1	134.5	1	140.2	1	141.3
	3	28.7			3	57.2	3	66.4	6	86.3	3	89.2	2	91.8	3	103.2	3	118.2	9	147.6	3	136.8	2	141.3	3	149.1	3	152.6
	5	40.8			6	68.8	5	76.6	8	95.2	5	97.2	5	103.5	12	134.0	4	123.6	15	175.2	5	146.4	3	145.6	5	160.4	5	162.6
	15	76.4			9	77.1					10	119.5	10	127.8			8	141.7			10	167.0	5	155.7	12	193.7	8	176.9
	25	104.3									15	125.8	14	143.0							16	189.9	8	168.1	15	204.0	16	209.8
													18	152.0											20	209.1	20	220.2

Rb(RbI)x

x=	0		1		2		3		4		5		6		7		8		9		10		11		12		13	
	#g	PA (Å²)	#g	PA (Å²)	#g	PA (Å²)	#g	PA (Å²)	#g	PA (Å²)	#g	PA (Å²)	#g	PA (Å²)	#g	PA (Å²)	#g	PA (Å²)	#g	PA (Å²)	#g	PA (Å²)	#g	PA (Å²)	#g	PA (Å²)	#g	PA (Å²)
	0	0.0	0	26.5	0	40.2	0	55.1	0	66.4	0	77.9	0	95.3	0	96.4	0	112.7	0	116.3	0	132.3	0	140.9	0	145.8	0	150.4
	1	15.9	1	34.1	1	47.3	2	65.6	1	73.6	1	85.1	1	99.0	1	101.4	24	200.8	1	121.9	1	136.7	17	206.0	1	152.4	1	154.0
	3	30.2	2	39.9	3	61.2	3	71.2	3	82.1	2	93.3	2	102.4	3	108.6			3	131.3	3	145.9			3	161.9	3	166.0
	5	42.4			6	71.8	5	81.7	6	91.0	5	106.2	3	115.8	12	141.3			9	157.3	5	156.9			5	171.8	5	175.7
	15	77.6			9	83.4	11	104.6	8	100.0	10	126.5	6	134.6					15	185.1	16	200.1			12	205.6	8	185.5
	25	105.5									15	130.2	14	150.2					0	0.0					15	216.9	16	221.1
											18	144.4	18	159.7											20	223.2	20	231.5
																									24	226.7	24	243.3
																									30	242.0	30	249.9
																									0	0.0		

Cs(CsI)x

x=	0		1		2		3		4		5		6		7		8		9		10		11		12		13	
	#g	PA (Å²)	#g	PA (Å²)	#g	PA (Å²)	#g	PA (Å²)	#g	PA (Å²)	#g	PA (Å²)	#g	PA (Å²)	#g	PA (Å²)	#g	PA (Å²)	#g	PA (Å²)	#g	PA (Å²)	#g	PA (Å²)	#g	PA (Å²)	#g	PA (Å²)
	0	0.0	0	29.6	0	44.6	0	60.7	0	71.2	0	86.0	0	97.9	0	106.9	0	121.9	0	128.8	0	144.9	0	157.0	0	160.7	0	167.4
	1	17.4	1	36.9	1	51.2	1	64.9	1	77.7	1	90.6	1	104.4	1	108.4	1	129.0	1	132.0	1	151.9	1	161.5	1	166.1	1	170.1
	2	24.8	2	43.4	3	65.7	3	75.8	2	82.0	2	99.8	3	111.1	3	116.7	0	0.0	2	138.9	3	160.3	2	164.3	3	177.7	3	179.9
	3	31.9			6	75.3	5	86.8	6	98.0	5	114.1	6	126.3	12	150.7	30	208.9	3	142.4	5	168.9	17	221.3	5	185.0	5	189.6
	5	44.3			9	87.1	6	92.2	8	106.8	10	132.9	10	144.2	21	180.1			4	146.6	6	173.1			12	219.3	8	203.3
	15	79.4					11	111.2	25	151.8	15	138.1	14	159.6					5	153.3	10	191.7			15	229.3	16	234.4
											18	152.1	18	166.3					6	156.2	16	213.4			20	239.3	20	247.3
											25	168.9	24	172.3					9	167.7					24	239.1	24	257.5
													30	193.1					12	184.6					30	256.7	30	264.8
													31	193.1					15	196.4								
																			21	201.3								

Table 4.4: Measured CCS ratios, temperature 1.

Na(NaI)x

	x=	0	1	2	3	4	5	6	7	8	9	10	11	12	13
T (°C)	S	Ω_w/Ω_0	Ω_w/Ω_0	Ω_w/Ω_0	Ω_w/Ω_0	Ω_w/Ω_0	Ω_w/Ω_0	Ω_w/Ω_0	Ω_w/Ω_0	Ω_w/Ω_0	Ω_w/Ω_0	Ω_w/Ω_0	Ω_w/Ω_0	Ω_w/Ω_0	Ω_w/Ω_0
26.5	0.037		0.060	0.052	0.071	0.052	0.066	0.080	0.085	0.089	0.068	0.062	0.063	0.068	0.065
26.6	0.040	0.067	0.055	0.051	0.068	0.050	0.066	0.078	0.084	0.088	0.069	0.062	0.067	0.069	0.071
26.65	0.043	0.072	0.062	0.058	0.076	0.057	0.070	0.086	0.095	0.097	0.073	0.070	0.076	0.079	0.076
26.2	0.044	0.080	0.065	0.059	0.078	0.059	0.075	0.091	0.098	0.104	0.080	0.076	0.079	0.084	0.075
27.15	0.069	0.090	0.077	0.068	0.090	0.070	0.084	0.102	0.113	0.117	0.098	0.091	0.101	0.111	0.082
26.7	0.097	0.107	0.088	0.081	0.102	0.083	0.097	0.121	0.132	0.138	0.119	0.113	0.126	0.145	0.114
27.55	0.109	0.112	0.092	0.085	0.107	0.087	0.104	0.132	0.143	0.149	0.135	0.128	0.141	0.167	0.164
26.15	0.137	0.127	0.104	0.096	0.122	0.098	0.117	0.149	0.161	0.167	0.157	0.153	0.170	0.202	0.227
27.6	0.155	0.132	0.108	0.101	0.124	0.104	0.124	0.157	0.170	0.177	0.170	0.165	0.186	0.214	0.246
26.85	0.219	0.172	0.137	0.130	0.157	0.136	0.160	0.199	0.216	0.225	0.232	0.227	0.246	0.271	
26.75	0.318	0.198	0.161	0.158	0.191	0.174	0.211	0.258	0.273	0.282	0.295	0.292	0.312		
27.3	0.348	0.197	0.165	0.163	0.201	0.186	0.225	0.276	0.286	0.298	0.310	0.308	0.333		
28.4	0.524	0.262	0.210	0.220	0.271	0.271	0.331	0.381	0.396	0.403	0.420	0.418			
26.85	0.636	0.295	0.233	0.251	0.303	0.312	0.370	0.423	0.440	0.448	0.466				

K(KI)x

	x=	0	1	2	3	4	5	6	7	8	9	10	11	12	13
T (°C)	S	Ω_w/Ω_0	Ω_w/Ω_0	Ω_w/Ω_0	Ω_w/Ω_0	Ω_w/Ω_0	Ω_w/Ω_0	Ω_w/Ω_0	Ω_w/Ω_0	Ω_w/Ω_0	Ω_w/Ω_0	Ω_w/Ω_0	Ω_w/Ω_0	Ω_w/Ω_0	Ω_w/Ω_0
26.5	0.037	0.075	0.110	0.085	0.099	0.070	0.077	0.080	0.075	0.072	0.080	0.056			0.046
26.7	0.040	0.085	0.100	0.079	0.096	0.067	0.075	0.086	0.072	0.070	0.081	0.058	0.067		0.046
26.05	0.045	0.096	0.113	0.091	0.108	0.077	0.087	0.091	0.087	0.084	0.095	0.068	0.074		0.053
26.55	0.044	0.092	0.111	0.087	0.106	0.074	0.081	0.086	0.084	0.080	0.093	0.066	0.078		0.052
27.05	0.068	0.106	0.123	0.098	0.120	0.086	0.099	0.103	0.103	0.099	0.113	0.079	0.091		0.066
26.65	0.099	0.116	0.135	0.112	0.132	0.098	0.112	0.114	0.119	0.115	0.126	0.093	0.109		0.073
27.75	0.110	0.121	0.139	0.112	0.140	0.104	0.119	0.124	0.127	0.126	0.135	0.100			0.083
26.25	0.137	0.140	0.153	0.124	0.151	0.117	0.128	0.136	0.142	0.137	0.149	0.113			0.092
27.65	0.155	0.141	0.157	0.128	0.157	0.120	0.135	0.144	0.147	0.145	0.154	0.119	0.138		0.098
26.95	0.217	0.174	0.183	0.152	0.184	0.145	0.161	0.170	0.180	0.178	0.190	0.156	0.175		0.118
26.75	0.318	0.201	0.203	0.173	0.205	0.168	0.184	0.199	0.215	0.208	0.223	0.186			
27.4	0.344	0.211	0.208	0.177	0.211	0.173	0.189	0.207	0.223	0.215	0.234	0.188			
28.25	0.525	0.266	0.250	0.227	0.261	0.224	0.246	0.275	0.286	0.281	0.309				
26.85	0.646	0.300	0.271	0.239	0.277	0.237	0.257	0.299	0.303	0.294	0.327				

Rb(RbI)x

	x=	0	1	2	3	4	5	6	7	8	9	10	11	12	13
T (°C)	S	Ω_w/Ω_0	Ω_w/Ω_0	Ω_w/Ω_0	Ω_w/Ω_0	Ω_w/Ω_0	Ω_w/Ω_0	Ω_w/Ω_0	Ω_w/Ω_0	Ω_w/Ω_0	Ω_w/Ω_0	Ω_w/Ω_0	Ω_w/Ω_0	Ω_w/Ω_0	Ω_w/Ω_0
26.65	0.040	0.085	0.113	0.088	0.083	0.054	0.060	0.051	0.050	0.040	0.047	0.059			0.021
26.45	0.037	0.074	0.130	0.095	0.089	0.056	0.064	0.053	0.048	0.038	0.042				0.020
26	0.045	0.091	0.125	0.100	0.097	0.061	0.070	0.062	0.061	0.047	0.054	0.068			0.027
26.6	0.044	0.089	0.122	0.096	0.093	0.060	0.065	0.058	0.058	0.048	0.055	0.063			0.029
27.1	0.067	0.104	0.143	0.110	0.110	0.076	0.085	0.077	0.077	0.068	0.071	0.078			0.039
26.7	0.098	0.114	0.152	0.118	0.120	0.084	0.095	0.086	0.089	0.078	0.086	0.082			0.043
27.65	0.111	0.120	0.158	0.123	0.128	0.089	0.101	0.093	0.097	0.087	0.095	0.098			0.053
26.2	0.138	0.139	0.172	0.136	0.139	0.103	0.114	0.107	0.113	0.103	0.110	0.109			0.061
27.55	0.158	0.137	0.177	0.142	0.145	0.108	0.122	0.114	0.119	0.114	0.123	0.113			0.066
26.9	0.216	0.167	0.202	0.163	0.172	0.130	0.144	0.137	0.147	0.141	0.155				0.082
26.65	0.320	0.196	0.226	0.186	0.199	0.152	0.172	0.167	0.181	0.180					
27.6	0.338	0.197	0.230	0.190	0.199	0.155	0.172	0.171	0.186	0.182	0.207				
28.3	0.519	0.248	0.274	0.234	0.251	0.203	0.221	0.228	0.246	0.249					
27	0.644	0.298	0.313	0.265	0.283	0.233	0.254	0.265	0.284	0.278					

Cs(CsI)x

	x=	0	1	2	3	4	5	6	7	8	9	10	11	12	13
T (°C)	S	Ω_w/Ω_0	Ω_w/Ω_0	Ω_w/Ω_0	Ω_w/Ω_0	Ω_w/Ω_0	Ω_w/Ω_0	Ω_w/Ω_0	Ω_w/Ω_0	Ω_w/Ω_0	Ω_w/Ω_0	Ω_w/Ω_0	Ω_w/Ω_0	Ω_w/Ω_0	Ω_w/Ω_0
26.85	0.022	0.072	0.081	0.059	0.035	0.021	0.024	0.016	0.013	0.013	0.010				0.006
26.65	0.041	0.095	0.090	0.069	0.047	0.030	0.033	0.022	0.022	0.020	0.016				0.010
26.4	0.037	0.093	0.093	0.071	0.048	0.028	0.033	0.023	0.021	0.020	0.016				0.008
26	0.044	0.099	0.100	0.076	0.057	0.036	0.041	0.030	0.027	0.022	0.023	0.029			0.014
26.6	0.044	0.098	0.098	0.076	0.053	0.036	0.040	0.028	0.027	0.025	0.023				0.013
27.05	0.065	0.112	0.113	0.087	0.067	0.048	0.052	0.039	0.038	0.033	0.030				0.018
27.3	0.069	0.107	0.113	0.086	0.069	0.047	0.049	0.038	0.033	0.032	0.029	0.036			0.018
26.8	0.097	0.125	0.123	0.098	0.080	0.056	0.062	0.048	0.046	0.040	0.038	0.049			0.022
27.8	0.111	0.131	0.129	0.103	0.084	0.062	0.066	0.056	0.053	0.045	0.040	0.053			0.025
26.3	0.138	0.141	0.142	0.112	0.099	0.072	0.078	0.065	0.064	0.058	0.055				0.032
27.45	0.159	0.147	0.149	0.118	0.103	0.077	0.083	0.069	0.069	0.062	0.059	0.068			0.035
26.8	0.215	0.174	0.171	0.138	0.124	0.095	0.104	0.088	0.087	0.082	0.082	0.089			
26.65	0.321	0.202	0.200	0.163	0.149	0.118	0.129	0.112	0.119	0.111	0.111				
27.6	0.338	0.201	0.202	0.163	0.152	0.122	0.130	0.116	0.117	0.121	0.117				

Table 4.5: Measured CCS ratios, temperature 2.

Na(NaI)x

	x=	0	1	2	3	4	5	6	7	8	9	10	11	12	13
T (°C)	S	Ω_w/Ω_0	Ω_w/Ω_0	Ω_w/Ω_0	Ω_w/Ω_0	Ω_w/Ω_0	Ω_w/Ω_0	Ω_w/Ω_0	Ω_w/Ω_0	Ω_w/Ω_0	Ω_w/Ω_0	Ω_w/Ω_0	Ω_w/Ω_0	Ω_w/Ω_0	Ω_w/Ω_0
35.05	0.025	0.065	0.054	0.054	0.066	0.050	0.061	0.076	0.082	0.082	0.064	0.060	0.061	0.071	0.062
34.5	0.030	0.069	0.054	0.053	0.068	0.071	0.063	0.076	0.082	0.085	0.066	0.063	0.062	0.070	0.060
34.7	0.030	0.074	0.058	0.056	0.067	0.053	0.064	0.080	0.085	0.086	0.068	0.064	0.066	0.074	0.067
35.5	0.041	0.084	0.066	0.065	0.075	0.063	0.073	0.094	0.092	0.102	0.077	0.072	0.075	0.088	0.078
35.05	0.075	0.107	0.082	0.082	0.094	0.079	0.091	0.116	0.121	0.126	0.107	0.102	0.107	0.123	0.088
35	0.086	0.115	0.089	0.086	0.102	0.085	0.098	0.124	0.132	0.136	0.116	0.110	0.118	0.139	0.100
35	0.106	0.125	0.099	0.095	0.111	0.095	0.106	0.134	0.141	0.147	0.130	0.127	0.136	0.163	0.123
34.8	0.143	0.158	0.124	0.121	0.134	0.116	0.130	0.163	0.176	0.184	0.174	0.169	0.180	0.222	0.231
35	0.196	0.185	0.141	0.139	0.157	0.140	0.156	0.197	0.211	0.217	0.215	0.214	0.225	0.268	
34.65	0.227	0.187	0.151	0.146	0.165	0.149	0.170	0.213	0.223	0.231	0.234	0.236	0.249	0.288	
35.4	0.350	0.242	0.194	0.193	0.223	0.208	0.244	0.296	0.307	0.313	0.326	0.326	0.335		
34.35	0.427	0.266	0.210	0.216	0.246	0.241	0.285	0.341	0.356	0.357	0.371	0.374			

K(KI)x

	x=	0	1	2	3	4	5	6	7	8	9	10	11	12	13
T (°C)	S	Ω_w/Ω_0	Ω_w/Ω_0	Ω_w/Ω_0	Ω_w/Ω_0	Ω_w/Ω_0	Ω_w/Ω_0	Ω_w/Ω_0	Ω_w/Ω_0	Ω_w/Ω_0	Ω_w/Ω_0	Ω_w/Ω_0	Ω_w/Ω_0	Ω_w/Ω_0	Ω_w/Ω_0
34.9	0.025	0.077	0.090	0.074	0.086	0.059	0.063	0.066	0.064	0.058	0.072	0.049	0.053	0.038	0.038
34.9	0.029	0.077	0.095	0.078	0.092	0.064	0.071	0.072	0.073	0.065	0.075	0.053	0.062	0.038	0.042
34.55	0.030	0.074	0.093	0.072	0.090	0.061	0.068	0.068	0.070	0.061	0.071	0.048			0.001
35.45	0.042	0.088	0.105	0.086	0.104	0.076	0.084	0.084	0.085	0.078	0.093	0.061	0.075	0.050	0.049
35.1	0.075	0.112	0.125	0.101	0.123	0.091	0.101	0.103	0.111	0.102	0.116	0.080	0.095	0.063	0.066
35	0.086	0.117	0.134	0.108	0.132	0.096	0.108	0.110	0.115	0.109	0.123	0.087	0.104	0.071	0.071
34.95	0.107	0.124	0.140	0.116	0.141	0.107	0.119	0.122	0.130	0.122	0.135	0.099	0.113	0.083	0.081
34.8	0.142	0.153	0.162	0.136	0.161	0.125	0.141	0.144	0.153	0.141	0.158	0.124	0.139	0.098	0.094
34.85	0.196	0.175	0.183	0.155	0.183	0.146	0.159	0.164	0.181	0.172	0.185	0.139			0.109
34.55	0.229	0.186	0.189	0.160	0.190	0.151	0.168	0.174	0.191	0.184	0.196	0.155	0.166		
35.3	0.353	0.236	0.230	0.200	0.230	0.191	0.204	0.223	0.243	0.227	0.251	0.205			
34.3	0.427	0.257	0.247	0.216	0.250	0.208	0.225	0.245	0.268	0.252	0.286				

Rb(RbI)x

	x=	0	1	2	3	4	5	6	7	8	9	10	11	12	13
T (°C)	S	Ω_w/Ω_0	Ω_w/Ω_0	Ω_w/Ω_0	Ω_w/Ω_0	Ω_w/Ω_0	Ω_w/Ω_0	Ω_w/Ω_0	Ω_w/Ω_0	Ω_w/Ω_0	Ω_w/Ω_0	Ω_w/Ω_0	Ω_w/Ω_0	Ω_w/Ω_0	Ω_w/Ω_0
35	0.025	0.072	0.100	0.077	0.070	0.046	0.049	0.038	0.040	0.029	0.033	0.043			0.018
35	0.028	0.071	0.107	0.084	0.076	0.051	0.049	0.043	0.042	0.034	0.035	0.044			0.017
34.45	0.030	0.081	0.109	0.086	0.078	0.052	0.056	0.048	0.045	0.035	0.039	0.047			0.022
35.35	0.043	0.091	0.122	0.094	0.091	0.061	0.065	0.060	0.057	0.045	0.053	0.057			0.028
35.15	0.075	0.109	0.142	0.111	0.111	0.078	0.083	0.076	0.077	0.068	0.071	0.077			0.041
34.95	0.087	0.116	0.148	0.117	0.119	0.084	0.090	0.084	0.085	0.074	0.083	0.080			0.044
34.9	0.106	0.124	0.157	0.125	0.127	0.092	0.099	0.092	0.094	0.084	0.092	0.087			0.049
34.9	0.141	0.147	0.181	0.146	0.150	0.112	0.122	0.116	0.118	0.110	0.118	0.109			0.064
34.85	0.198	0.173	0.203	0.166	0.173	0.132	0.146	0.137	0.144	0.138	0.147	0.134			0.081
34.5	0.231	0.179	0.213	0.176	0.184	0.141	0.154	0.149	0.158	0.151	0.163	0.148			
35.25	0.356	0.228	0.255	0.210	0.220	0.176	0.192	0.190	0.204	0.196	0.223				
34.35	0.423	0.243	0.265	0.222	0.236	0.192	0.204	0.208	0.223	0.220	0.240				

Cs(CsI)x

	x=	0	1	2	3	4	5	6	7	8	9	10	11	12	13
T (°C)	S	Ω_w/Ω_0	Ω_w/Ω_0	Ω_w/Ω_0	Ω_w/Ω_0	Ω_w/Ω_0	Ω_w/Ω_0	Ω_w/Ω_0	Ω_w/Ω_0	Ω_w/Ω_0	Ω_w/Ω_0	Ω_w/Ω_0	Ω_w/Ω_0	Ω_w/Ω_0	Ω_w/Ω_0
35	0.025	0.076	0.074	0.058	0.037	0.025	0.027	0.016	0.018	0.013	0.016	0.026			0.008
34.6	0.030	0.078	0.081	0.061	0.043	0.027	0.030	0.018	0.022	0.013	0.017	0.020			0.007
35	0.028	0.076	0.077	0.059	0.039	0.025	0.029	0.018	0.020	0.015	0.014				0.006
35.35	0.043	0.091	0.092	0.074	0.054	0.037	0.040	0.026	0.032	0.022	0.021	0.031			0.016
35.05	0.076	0.105	0.113	0.089	0.072	0.050	0.057	0.039	0.042	0.031	0.033	0.044			0.021
34.85	0.087	0.115	0.121	0.094	0.079	0.055	0.060	0.042	0.047	0.035	0.038	0.041			0.019
34.85	0.108	0.125	0.129	0.103	0.086	0.063	0.067	0.051	0.055	0.042	0.043	0.055			0.024
34.9	0.141	0.145	0.149	0.121	0.105	0.078	0.085	0.066	0.071	0.059	0.059	0.069			0.037
34.85	0.197	0.170	0.174	0.141	0.126	0.096	0.104	0.085	0.090	0.079	0.081				
34.6	0.230	0.179	0.183	0.147	0.134	0.106	0.112	0.096	0.101	0.087	0.090				0.046
35.25	0.358	0.225	0.219	0.182	0.170	0.137	0.149	0.131	0.139	0.131	0.143				
34.45	0.419	0.242	0.233	0.194	0.183	0.149	0.158	0.144	0.150	0.147					

Table 4.6: Measured CCS ratios, temperature 3.

Na(NaI)x

	x=	0	1	2	3	4	5	6	7	8	9	10	11	12	13
T (°C)	S	Ω_w/Ω_0	Ω_w/Ω_0	Ω_w/Ω_0	Ω_w/Ω_0	Ω_w/Ω_0	Ω_w/Ω_0	Ω_w/Ω_0	Ω_w/Ω_0	Ω_w/Ω_0	Ω_w/Ω_0	Ω_w/Ω_0	Ω_w/Ω_0	Ω_w/Ω_0	Ω_w/Ω_0
41.55	0.020	0.052	0.049	0.041	0.050	0.043	0.049	0.053	0.058	0.058	0.049	0.046	0.046	0.048	0.048
42.05	0.030	0.063	0.058	0.051	0.061	0.051	0.061	0.068	0.066	0.071	0.057	0.056	0.058	0.057	0.053
42.5	0.052	0.086	0.075	0.065	0.077	0.067	0.074	0.083	0.085	0.091	0.079	0.075	0.077	0.082	0.063
42.05	0.074	0.106	0.087	0.077	0.087	0.079	0.084	0.098	0.103	0.108	0.097	0.093	0.098	0.108	0.077
41.3	0.100	0.130	0.106	0.095	0.109	0.092	0.103	0.122	0.129	0.137	0.129	0.123	0.130	0.152	0.134
41.65	0.156	0.167	0.135	0.122	0.136	0.124	0.135	0.162	0.173	0.176	0.183	0.178	0.190	0.217	0.241
42.5	0.242	0.213	0.177	0.164	0.182	0.170	0.189	0.224	0.235	0.242	0.258	0.254	0.266	0.299	0.328
41.95	0.285	0.242	0.195	0.182	0.203	0.195	0.219	0.257	0.265	0.271	0.287	0.291	0.304		

K(KI)x

	x=	0	1	2	3	4	5	6	7	8	9	10	11	12	13
T (°C)	S	Ω_w/Ω_0	Ω_w/Ω_0	Ω_w/Ω_0	Ω_w/Ω_0	Ω_w/Ω_0	Ω_w/Ω_0	Ω_w/Ω_0	Ω_w/Ω_0	Ω_w/Ω_0	Ω_w/Ω_0	Ω_w/Ω_0	Ω_w/Ω_0	Ω_w/Ω_0	Ω_w/Ω_0
41.55	0.021	0.059	0.074	0.056	0.074	0.046	0.056	0.061	0.059	0.054	0.060	0.042	0.042	0.038	0.034
42.15	0.030	0.073	0.084	0.067	0.090	0.056	0.070	0.070	0.069	0.070	0.078	0.060	0.064	0.054	0.046
42.7	0.051	0.089	0.101	0.080	0.104	0.072	0.084	0.090	0.093	0.086	0.100	0.069	0.072	0.059	0.056
42.15	0.073	0.102	0.116	0.092	0.120	0.085	0.099	0.104	0.110	0.104	0.118	0.084	0.089	0.081	0.071
41.5	0.099	0.131	0.137	0.110	0.140	0.104	0.121	0.128	0.128	0.125	0.138	0.102	0.115	0.098	0.092
41.55	0.157	0.163	0.163	0.135	0.167	0.131	0.147	0.155	0.167	0.162	0.174	0.132	0.145	0.127	0.108
42.55	0.241	0.213	0.203	0.172	0.208	0.163	0.181	0.194	0.213	0.203	0.221	0.174			
42	0.280	0.226	0.212	0.183	0.219	0.175	0.196	0.211	0.226	0.217	0.238	0.192			

Rb(RbI)x

	x=	0	1	2	3	4	5	6	7	8	9	10	11	12	13
T (°C)	S	Ω_w/Ω_0	Ω_w/Ω_0	Ω_w/Ω_0	Ω_w/Ω_0	Ω_w/Ω_0	Ω_w/Ω_0	Ω_w/Ω_0	Ω_w/Ω_0	Ω_w/Ω_0	Ω_w/Ω_0	Ω_w/Ω_0	Ω_w/Ω_0	Ω_w/Ω_0	Ω_w/Ω_0
41.6	0.021	0.064	0.083	0.068	0.070	0.041	0.045	0.039	0.037	0.028	0.032	0.039	0.030		0.021
42.2	0.029	0.073	0.096	0.077	0.083	0.054	0.057	0.052	0.047	0.037	0.046	0.049	0.054		0.026
42.65	0.052	0.088	0.110	0.090	0.101	0.065	0.072	0.066	0.065	0.055	0.061	0.076			0.036
42.2	0.073	0.104	0.128	0.106	0.118	0.081	0.091	0.083	0.084	0.072	0.079	0.080	0.075		0.048
41.5	0.100	0.128	0.147	0.121	0.138	0.097	0.108	0.099	0.102	0.090	0.106	0.102	0.095		0.056
41.65	0.155	0.154	0.176	0.149	0.167	0.121	0.135	0.128	0.132	0.122	0.131	0.121			0.074
42.45	0.241	0.206	0.223	0.190	0.208	0.159	0.176	0.171	0.179	0.171	0.191	0.175			
41.9	0.284	0.215	0.231	0.199	0.218	0.172	0.187	0.182	0.194	0.190	0.206	0.188			

Cs(CsI)x

	x=	0	1	2	3	4	5	6	7	8	9	10	11	12	13
T (°C)	S	Ω_w/Ω_0	Ω_w/Ω_0	Ω_w/Ω_0	Ω_w/Ω_0	Ω_w/Ω_0	Ω_w/Ω_0	Ω_w/Ω_0	Ω_w/Ω_0	Ω_w/Ω_0	Ω_w/Ω_0	Ω_w/Ω_0	Ω_w/Ω_0	Ω_w/Ω_0	Ω_w/Ω_0
41.5	0.021	0.068	0.069	0.054	0.039	0.026	0.028	0.020	0.021	0.020	0.017	0.014			0.011
42.15	0.029	0.077	0.075	0.060	0.044	0.030	0.033	0.026	0.028	0.025	0.019	0.021			0.014
42.55	0.051	0.092	0.094	0.074	0.060	0.041	0.046	0.034	0.038	0.032	0.028	0.029			0.019
42.2	0.073	0.102	0.110	0.089	0.077	0.054	0.058	0.046	0.049	0.043	0.043	0.037			0.025
41.45	0.100	0.128	0.132	0.104	0.093	0.068	0.073	0.061	0.062	0.059	0.058	0.063			0.033
41.65	0.153	0.153	0.158	0.129	0.118	0.090	0.096	0.081	0.085	0.077	0.074	0.075			0.046
42.45	0.244	0.198	0.199	0.165	0.154	0.119	0.131	0.114	0.119	0.115	0.113				0.081
41.8	0.285	0.213	0.212	0.176	0.171	0.134	0.142	0.126	0.133	0.133	0.139				

Chapter 5 Conclusions and Future Work

5.1 Conclusions

This dissertation describes two new systems for studying vapor uptake by aerosol particles in the size range of one molecule to several nanometers as well as a theoretical approach for compaing measurements with model predictions. A summary of the work is as follows:

1) For the measurement of vapor uptake for particles in the size range of 2-20 nanometers we first developed a drift tube type ion mobility spectrometer specifically designed for measurement of charged aerosol particles. The instrument showed a near mobility independent resolution of around 5. The peak arrival time and transmission efficiency through the device was shown to be a function of the ratio of an electrostatic and advective Peclet number.

2) We developed a system utilizing a High Resolution DMA in tandem with the DTIMS. The system was used to measure the uptake of water vapor by hygroscopic salts with dry diameters ranging from 2.85 to 7.6 nm. We also show how measurements of the mobility shifts due to vapor uptake can be compared to theoretical models by applying the change in Gibbs free energy upon sorption of a given number of vapor molecules. Comparison of measurements to classical Kelvin-Thomson-Raoult theory highlighted the stark disagreement that classical theory has with observations of uptake by small particles. The precision of this system was determined by simulated

arrival time distributions and for the measurements shown the growth factor precision *(σGF/GF)* was shown to be ~0.24%.

3) We described a system for measuring the uptake of vapors by molecular clusters ranging in size from one molecule to near 2nm. We show how density functional theory calculations coupled with orientationally averaged projected area measurements can be used to estimate the predicted collision cross sections for the clusters. These CCSs can then be used to correlate the measured changes in collision cross sections to the equivalent changes predicted using the previously described model. Again, comparisons of classical vapor uptake theory to the measurements are in stark disagreement.

5.2 Recommendations for Future Work

Enhancements to the DTIMS device performance

One principle advantage of using the DTIMS for vapor uptake by small particles is the potential for high resolving power. Simulated arrival time distributions predict higher values of resolving power than were measured with the prototype device. It is important to find the cause of this disparity and possibly design a means to improve the device performance. Further work can also be done to improve the resolving power and transmission efficiency using time varying and or spatially varying electrostatic fields. In addition, the current hardware will occasionally reset when applying high voltages which also needs to be addresed.

Work related to applying the DTIMS for Heterogenous Uptake Measurements

The prototype instrument is limited to relative humidities less than 25% due to anomalous observations of arrival time distributions of non-hygroscopic aerosols at higher relative humidities. Although these anomalies were not observed in recent uptake measurements the cause should be investigated. Additionally, measurements made using the HRDMA-DTIMS should be compared to a TDMA system.

Comparison between HRDMA-MS measurements and theoretical calculations

Changes in Gibbs free energies upon vapor sorption can be predicted using molecular dynamics simulations for known cluster and vapor composition. Comparison to the DMA-MS measurement results using these calculated energy values to estimate the collision cross section ratios can provide insight into the models used to calculate these energies.

Bibliography

[1] W. F. Siems, C. Wu, E. E. Tarver, H. H. Hill, P. R. Larsen, and D. G. Mcminn, "Measuring the Resolving Power of Ion Mobility Spectrometers," *Analytical Chemistry,* vol. 66, pp. 4195-4201, Dec 1 1994.

[2] S. Rosser and J. F. de la Mora, "Vienna-type DMA of high resolution and high flow rate," *Aerosol Science and Technology,* vol. 39, pp. 1191-1200, Dec 2005.

[3] E. O. Knutson and K. T. Whitby, "Aerosol Classification By Electric Mobility: Apparatus, Theory, and Applications," *Journal of Aerosol Science,* vol. 6, pp. 443-451, 1975.

[4] J. Fernandez de la Mora and J. Kozlowski, "Hand-held differential mobility analyzers of high resolution for 1-30 nm particles: Design and fabrication considerations," *Journal of Aerosol Science,* vol. 57, pp. 45-53, Mar 2013.

[5] D. R. Chen, D. Y. H. Pui, D. Hummes, H. Fissan, F. R. Quant, and G. J. Sem, "Design and evaluation of a nanometer aerosol differential mobility analyzer (Nano-DMA)," *Journal of Aerosol Science,* vol. 29, pp. 497-509, JUN-JUL 1998.

[6] R. C. Flagan, "Opposed Migration Aerosol Classifier (OMAC)," *Aerosol Science and Technology,* vol. 38, pp. 890-899, 2004.

[7] P. Kulkarni and J. Wang, "New fast integrated mobility spectrometer for real-time measurement of aerosol size distribution - I: Concept and theory," *Journal of Aerosol Science,* vol. 37, pp. 1303-1325, Oct 2006.

[8] D. K. Song and S. Dhaniyala, "Nanoparticle cross-flow differential mobility analyzer (NCDMA): Theory and design," *Journal of Aerosol Science,* vol. 38, pp. 964-979, Sep 2007.

[9] G. Vidal-de-Miguel, M. Macía, and J. Cuevas, "Transversal Modulation Ion Mobility Spectrometry (TM-IMS), A New Mobility Filter Overcoming Turbulence Related Limitations," *Analytical Chemistry,* vol. 84, pp. 7831-7837, 2012/09/18 2012.

[10] M. Zhang and A. S. Wexler, "Cross flow ion mobility spectrometry: Theory and initial prototype testing," *International Journal of Mass Spectrometry,* vol. 258, pp. 13-20, Dec 2006.

[11] A. J. Downard, J. F. Dama, and R. C. Flagan, "An Asymptotic Analysis of Differential Electrical Mobility Classifiers," *Aerosol Science and Technology,* vol. 45, pp. 727-739, 2011.

[12] M. R. Stolzenburg and P. H. McMurry, "Equations governing single and tandem DMA configurations and a new lognormal approximation to the transfer function," *Aerosol Science and Technology,* vol. 42, pp. 421-432, 2008.

[13] M. R. Stolzenburg, "An Ultrafine Aerosol Size Distribution Measuring System," Mechanical Engineering, University of Minnesota, Minneapolis, MN, 1988.

[14] S. C. Wang and R. C. Flagan, "Scanning Electrical Mobility Spectrometer," *Aerosol Science and Technology,* vol. 13, pp. 230-240, 1990.

[15] R. H. St. Louis and H. H. Hill, "Ion Mobility Spectrometry in Analytical-Chemistry," *Critical Reviews in Analytical Chemistry,* vol. 21, pp. 321-355, 1990.

[16] H. Borsdorf and G. A. Eiceman, "Ion mobility spectrometry: Principles and applications," *Applied Spectroscopy Reviews,* vol. 41, pp. 323-375, 2006.
[17] E. A. Mason and E. W. McDaniel, *Transport Properties of Ions in Gases*. New York: Wiley, 1988.
[18] H. E. Revercomb and E. A. Mason, "Theory of Plasma Chromatography Gaseous Electrophoresis - Review," *Analytical Chemistry,* vol. 47, pp. 970-983, 1975.
[19] S. Rosser and J. Fernandez de la Mora, "Vienna-type DMA of high resolution and high flow rate," *Aerosol Science and Technology,* vol. 39, pp. 1191-1200, DEC 2005.
[20] S. Ude and J. Fernandez de la Mora, "Molecular monodisperse mobility and mass standards from electrosprays of tetra-alkyl ammonium halides," *Journal of Aerosol Science,* vol. 36, pp. 1224-1237, OCT 2005.
[21] M. Attoui, M. Paragano, J. Cuevas, and J. Fernandez de la Mora, "Tandem DMA Generation of Strictly Monomobile 1-3.5 nm Particle Standards," *Aerosol Science and Technology,* vol. 47, pp. 499-511, May 2013.
[22] P. Martinez-Lozano and J. Fernandez de la Mora, "Resolution improvements of a nano-DMA operating transonically," *Journal of Aerosol Science,* vol. 37, pp. 500-512, APR 2006.
[23] S. I. Merenbloom, R. S. Glaskin, Z. B. Henson, and D. E. Clemmer, "High-Resolution Ion Cyclotron Mobility Spectrometry," *Analytical Chemistry,* vol. 81, pp. 1482-1487, Feb 2009.
[24] J. Wang, V. F. McNeill, D. R. Collins, and R. C. Flagan, "Fast mixing condensation nucleus counter: Application to rapid scanning differential mobility analyzer measurements," *Aerosol Science and Technology,* vol. 36, pp. 678-689, JUN 2002.
[25] P. Dugourd, R. R. Hudgins, D. E. Clemmer, and M. F. Jarrold, "High-resolution ion mobility measurements," *Review of Scientific Instruments,* vol. 68, pp. 1122-1129, Feb 1997.
[26] S. V. Hering and M. R. Stolzenburg, "A method for particle size amplification by water condensation in a laminar, thermally diffusive flow," *Aerosol Science and Technology,* vol. 39, pp. 428-436, May 2005.
[27] S. V. Hering, M. R. Stolzenburg, F. R. Quant, D. R. Oberreit, and P. B. Keady, "A laminar-flow, water-based condensation particle counter (WCPC)," *Aerosol Science and Technology,* vol. 39, pp. 659-672, Jul 2005.
[28] K. Iida, M. R. Stolzenburg, P. H. McMurry, J. N. Smith, F. R. Quant, D. R. Oberreit, P. B. Keady, A. Eiguren-Fernandez, G. S. Lewis, N. M. Kreisberg, and S. V. Hering, "An ultrafine, water-based condensation particle counter and its evaluation under field conditions," *Aerosol Science and Technology,* vol. 42, pp. 862-871, 2008.
[29] H. G. Scheibel and J. Porstendorfer, "Generation of monodisperse Ag-aerosol and NaCl-aerosol with particle diameters between 2-nm and 300-nm," *Journal of Aerosol Science,* vol. 14, pp. 113-&, 1983.
[30] R. Gopalakrishnan, M. R. Meredith, C. Larriba-Andaluz, and C. J. Hogan, "Brownian Dynamics Determination of the Bipolar Steady State Charge

Distribution on Spheres and Non-spheres in the Transition Regime," *Journal of Aerosol Science,* vol. 63, pp. 126-145, 2013.
[31] A. Wiedensohler, "An Approximation of the Bipolar Charge-Distribution for Particles in the Sub-Micron Size Range," *Journal of Aerosol Science,* vol. 19, pp. 387-389, JUN 1988.
[32] C. Larriba, C. J. Hogan, M. Attoui, R. Borrajo, J. Fernandez-Garcia, and J. Fernandez de la Mora, "The Mobility-Volume Relationship below 3.0 nm examined by Tandem Mobility-Mass Measurement," *Aerosol Science and Technology,* vol. 45, pp. 453-467, 2011.
[33] Y. S. Cheng and H. C. Yeh, "Theory of a screen-type diffusion battery," *Journal of Aerosol Science,* vol. 11, pp. 313-320, 1980.
[34] P. G. Gormley and M. Kennedy, "Diffusion from a stream flowing through a cylindrical tube," *Proceedings of the Irish Royal Academy,* vol. 52A, pp. 163-169, 1949.
[35] R. Gopalakrishnan and C. J. Hogan, "Coulomb-Influenced Collisions in Aerosols and Dusty Plasmas," *Physical Review E,* vol. 85, p. 026410, 2012.
[36] R. C. Flagan, "On differential mobility analyzer resolution," *Aerosol Science and Technology,* vol. 30, pp. 556-570, Jun 1999.
[37] K. E. G. Wieighardt, "On the resistance of screens," *Aeronautical Quarterly,* vol. IV, pp. 186-192, 1953.
[38] D. L. Ermak and H. Buckholz, "Numerical-Integration of the Langevin Equation - Monte-Carlo Simulation," *Journal of Computational Physics,* vol. 35, pp. 169-182, 1980.
[39] D. R. Oberreit, "A Device and Methods to Investigate the Uptake of Vapor Molecules by Cluster Ions and Aerosol Particles," Mechanical Engineering, University of Minnesota, Minneapolis, MN, 2013.
[40] G. Kemmer and S. Keller, "Nonlinear least-squares data fitting in Excel Spreadsheets," *Nature Protocols,* vol. 5, pp. 267-281, 2010.
[41] S. L. Kaufman, J. W. Skogen, F. D. Dorman, F. Zarrin, and K. C. Lewis, "Macromolecule analysis based on electrophoretic mobility in air: Globular proteins," *Analytical Chemistry,* vol. 68, pp. 1895-1904, JUN 1 1996.
[42] A. Maiβer, V. Premnath, A. Ghosh, T. A. Nguyen, M. Attoui, and C. J. Hogan, "Determination of gas phase protein ion densities via ion mobility analysis with charge reduction," *Physical Chemistry Chemical Physics,* vol. 13, pp. 21630-21641, 2011.
[43] C. Laschober, C. S. Kaddis, G. P. Reischl, J. A. Loo, G. Allmaier, and W. W. Szymanski, "Comparison of various nano-differential mobility analysers (nDMAs) applying globular proteins," *Journal of Experimental Nanoscience,* vol. 2, pp. 291-301, 2007.
[44] C. J. Hogan and J. Fernandez de la Mora, "Ion Mobility Measurements of Non-Denatured 12 - 150 kDa Proteins and Protein Multimers by Tandem Differential Mobility Analysis - Mass Spectrometry (DMA-MS)," *Journal of the American Society for Mass Spectrometry,* vol. 22, pp. 158-172, 2011.

[45] C. Orr, F. K. Hurd, and W. J. Corbett, "Aerosol size and relative humidity," *Journal of Colloid Science,* vol. 13, pp. 472-482, 1958.
[46] R. J. Weber, J. J. Marti, P. H. McMurry, F. L. Eisele, D. J. Tanner, and A. Jefferson, "Measurements of new particle formation and ultrafine particle growth rates at a clean continental site," *Journal of Geophysical Research-Atmospheres,* vol. 102, pp. 4375-4385, Feb 27 1997.
[47] H. V. Nguyen and R. C. Flagan, "Particle Formation and Growth in Single-Stage Aerosol Reactors," *Langmuir,* vol. 7, pp. 1807-1814, Aug 1991.
[48] S. T. Martin, G. Biskos, and P. R. Buseck, "Hygroscopic growth of nucleation-mode acidic sulfate particles," *Journal of Aerosol Science,* vol. 40, pp. 338-347, Apr 2009.
[49] J. J. Thomson, *Conduction of electricity through gases*. New York,: Dover Publications, 1906.
[50] W. Thomson, "On the Equilibrium of Vapor at a Curved Surface of Liquid," *Proceedings of the Royal Society of Edinburgh,* vol. 7, 1870.
[51] P. M. Winkler, G. Steiner, A. Vrtala, H. Vehkamaki, M. Noppel, K. E. J. Lehtinen, G. P. Reischl, P. E. Wagner, and M. Kulmala, "Heterogeneous nucleation experiments bridging the scale from molecular ion clusters to nanoparticles," *Science,* vol. 319, pp. 1374-1377, Mar 7 2008.
[52] A. W. Castleman, P. M. Holland, and R. G. Keesee, "Properties of Ion Clusters and Their Relationship to Hetero-Molecular Nucleation," *Journal of Chemical Physics,* vol. 68, pp. 1760-1767, 1978.
[53] I. Dzidic and P. Kebarle, "Hydration of the alkali ions in the gas phase. Enthalpies and entropies of reactions M+(H2O)n-1 + H2O = M+(H2O)n," *The Journal of Physical Chemistry,* vol. 74, pp. 1466-1474, 1970/04/01 1970.
[54] P. M. Winkler, A. Vrtala, G. Steiner, D. Wimmer, H. Vehkamaki, K. E. J. Lehtinen, G. P. Reischl, M. Kulmala, and P. E. Wagner, "Quantitative Characterization of Critical Nanoclusters Nucleated on Large Single Molecules," *Physical Review Letters,* vol. 108, Feb 23 2012.
[55] P. Mirabel, H. Reiss, and R. K. Bowles, "A theory for the deliquescence of small particles," *Journal of Chemical Physics,* vol. 113, pp. 8200-8205, Nov 8 2000.
[56] G. Biskos, A. Malinowski, L. M. Russell, P. R. Buseck, and S. T. Martin, "Nanosize effect on the deliquescence and the efflorescence of sodium chloride particles," *Aerosol Science and Technology,* vol. 40, pp. 97-106, Feb 2006.
[57] H. Kohler, "The nucleus in and the growth of hygroscopic droplets," *Transactions of the Faraday Society,* vol. 32, pp. 1152-1161, 1936.
[58] P. Hamill, R. P. Turco, C. S. Kiang, O. B. Toon, and R. C. Whitten, "An Analysis of Various Nucleation Mechanisms for Sulfate Particles in the Stratosphere," *Journal of Aerosol Science,* vol. 13, pp. 561-585, 1982.
[59] S. M. Thompson, K. E. Gubbins, J. P. R. B. Walton, R. A. R. Chantry, and J. S. Rowlinson, "A Molecular-Dynamics Study of Liquid-Drops," *Journal of Chemical Physics,* vol. 81, pp. 530-542, 1984.
[60] R. McGraw and E. R. Lewis, "Deliquescence and efflorescence of small particles," *Journal of Chemical Physics,* vol. 131, Nov 21 2009.

[61] A. K. Shchekin and A. I. Rusanov, "Generalization of the Gibbs-Kelvin-Kohler and Ostwald-Freundlich equations for a liquid film on a soluble nanoparticle," *Journal of Chemical Physics,* vol. 129, Oct 21 2008.
[62] Y. S. Djikaev, R. Bowles, H. Reiss, K. Hameri, A. Laaksonen, and M. Vakeva, "Theory of size dependent deliquescence of nanoparticles: Relation to heterogeneous nucleation and comparison with experiments," *Journal of Physical Chemistry B,* vol. 105, pp. 7708-7722, Aug 16 2001.
[63] N. H. Fletcher, "Size Effect in Heterogeneous Nucleation," *The Journal of Chemical Physics,* vol. 29, pp. 572-576, 1958.
[64] C. S. Dutcher, X. L. Ge, A. S. Wexler, and S. L. Clegg, "An Isotherm-Based Thermodynamic Model of Multicomponent Aqueous Solutions, Applicable Over the Entire Concentration Range," *Journal of Physical Chemistry A,* vol. 117, pp. 3198-3213, Apr 2013.
[65] P. H. McMurry, "The history of condensation nucleus counters," *Aerosol Science and Technology,* vol. 33, pp. 297-322, Oct 2000.
[66] A. Laaksonen, V. Talanquer, and D. W. Oxtoby, "Nucleation - Measurements, Theory, and Atmospheric Applications," *Annual Review of Physical Chemistry,* vol. 46, pp. 489-524, 1995.
[67] P. E. Wagner, D. Kaller, A. Vrtala, A. Lauri, M. Kulmala, and A. Laaksonen, "Nucleation probability in binary heterogeneous nucleation of water-n-propanol vapor mixtures on insoluble and soluble nanoparticles," *Physical Review E,* vol. 67, Feb 2003.
[68] I. J. Ford, "Nucleation theorems, the statistical mechanics of molecular clusters, and a revision of classical nucleation theory," *Physical Review E,* vol. 56, pp. 5615-5629, Nov 1997.
[69] D. J. Rader and P. H. Mcmurry, "Application of the Tandem Differential Mobility Analyzer to Studies of Droplet Growth or Evaporation," *Journal of Aerosol Science,* vol. 17, pp. 771-787, Oct 1986.
[70] E. Swietlicki, H. C. Hansson, K. HÄMeri, B. Svenningsson, A. Massling, G. McFiggans, P. H. McMurry, T. PetÄJÄ, P. Tunved, M. Gysel, D. Topping, E. Weingartner, U. Baltensperger, J. Rissler, A. Wiedensohler, and M. Kulmala, "Hygroscopic properties of submicrometer atmospheric aerosol particles measured with H-TDMA instruments in various environments—a review," *Tellus B,* vol. 60, pp. 432-469, 2008.
[71] I. N. Tang and H. R. Munkelwitz, "An Investigation of Solute Nucleation in Levitated Solution Droplets," *Journal of Colloid and Interface Science,* vol. 98, pp. 430-438, 1984.
[72] I. N. Tang, "Phase transformation and growth of aerosol particles composed of mixed salts," *Journal of Aerosol Science,* vol. 7, pp. 361-371, 1976.
[73] E. J. Davis and A. K. Ray, "Single Aerosol-Particle Size and Mass Measurements using an Electrodynamic Balance," *Journal of Colloid and Interface Science,* vol. 75, pp. 566-576, 1980.
[74] A. E. Haddrell, J. F. Davies, A. Yabushita, and J. P. Reid, "Accounting for Changes in Particle Charge, Dry Mass and Composition Occurring During

Studies of Single Levitated Particles," *Journal of Physical Chemistry A,* vol. 116, pp. 9941-9953, Oct 2012.

[75] J. Fernandez de la Mora, L. de Juan, T. Eichler, and J. Rosell, "Differential mobility analysis of molecular ions and nanometer particles," *Trac-Trends in Analytical Chemistry,* vol. 17, pp. 328-339, JUN-JUL 1998.

[76] J. Fernandez-Garcia and J. Fernandez de la Mora, "Measuring the Effect of Ion-Induced Drift-Gas Polarization on the Electrical Mobilities of Multiply-Charged Ionic Liquid Nanodrops in Air," *Journal of the American Society for Mass Spectrometry,* vol. In Press, 2013.

[77] C. Larriba and C. J. Hogan, " Momentum Transfer Collision Cross Sections and Ion Mobilities in Diatomic Gases: Measurement vs. Prediction with Non-Specular Scattering Models. ," *Journal of Physical Chemistry A,* vol. 117, pp. 3887-3901, 2013.

[78] C. J. Hogan and J. Fernandez de la Mora, "Tandem ion mobility-mass spectrometry (IMS-MS) study of ion evaporation from ionic liquid-acetonitrile nanodrops," *Physical Chemistry Chemical Physics,* vol. 11, pp. 8079-8090, 2009.

[79] D. R. Oberreit, P. H. McMurry, and C. J. Hogan, "Mobility Analysis of 2 nm to 11 nm Aerosol Particles with an Aspirating Drift Tube Ion Mobility Spectrometer," *Aerosol Science & Technology,* vol. Submitted, 2013.

[80] L. Greenspan, "Humidity fixed points of binary saturated aqueous solutions," *Journal of Research, National Bureau of Standards (US), Series A, Physics and Chemistry,* vol. 81, pp. 89-96, 1977.

[81] J. Rus, D. Moro, J. A. Sillero, J. Royuela, A. Casado, F. Estevez-Molinero, and J. Fernandez de la Mora, "IMS–MS studies based on coupling a differential mobility analyzer (DMA) to commercial API–MS systems," *International Journal of Mass Spectrometry,* vol. 298, pp. 30-40, 2010.

[82] M. Gamero-Castano and J. Fernandez de la Mora, "Mechanisms of electrospray ionization of singly and multiply charged salt clusters," *Analytica Chimica Acta,* vol. 406, pp. 67-91, FEB 1 2000.

[83] C. J. Hogan, K. M. Yun, D. R. Chen, I. W. Lenggoro, P. Biswas, and K. Okuyama, "Controlled size polymer particle production via electrohydrodynamic atomization," *Colloids and Surfaces a-Physicochemical and Engineering Aspects,* vol. 311, pp. 67-76, Dec 1 2007.

[84] A. C. MacMillan, T. M. McIntire, J. A. Freites, D. J. Tobias, and S. A. Nizkorodov, "Interaction of Water Vapor with the Surfaces of Imidazolium-Based Ionic Liquid Nanoparticles and Thin Films," *Journal of Physical Chemistry B,* vol. 116, pp. 11255-11265, Sep 2012.

[85] R. Gopalakrishnan and C. J. Hogan, "Determination of the Transition Regime Collision Kernel from Mean First Passage Times," *Aerosol Science and Technology,* vol. 45, pp. 1499-1509, 2011.

[86] R. Gopalakrishnan, T. Thajudeen, and C. J. Hogan, "Collision Limited Reaction Rates for Arbitrarily Shaped Particles across the Entire Diffusive Knudsen Number Range," *Journal of Chemical Physics,* vol. 135, p. 054302, 2011.

[87] H. Ouyang, R. Gopalakrishnan, and C. J. Hogan, "Nanoparticle collisions in the gas phase in the presence of singular contact potentials," *The Journal of Chemical Physics,* vol. 137, p. 064316, 2012.
[88] B. E. Dahneke, "Simple Kinetic Theory of Brownian Diffusion in Vapors and Aerosols," in *Theory of Dispersed Multiphase Flow*, R. E. Meyer, Ed., ed New York: Academic Press, 1983.
[89] N. A. Fuchs, "On the Stationary Charge Distribution on Aerosol Particles in a Bipolar Ionic Atmosphere," *Geofis. Pura Appl.,* vol. 51, pp. 185-193, 1963.
[90] J. E. Allen, "Probe Theory - The Orbital Motion Approach," *Physica Scripta,* vol. 45, pp. 497-503, May 1992.
[91] T. Su and M. T. Bowers, "Ion-Polar Molecule Collisions - Effect of Molecular-Size on Ion-Polar Molecule Rate Constants," *Journal of the American Chemical Society,* vol. 95, pp. 7609-7610, 1973.
[92] L. M. Russell and Y. Ming, "Deliquescence of small particles," *Journal of Chemical Physics,* vol. 116, pp. 311-321, Jan 1 2002.
[93] J. L. Katz and M. D. Donohue, "A Kinetic Approach to Homogeneous Nucleation Theory," in *Advances in Chemical Physics*, ed: John Wiley & Sons, Inc., 2007, pp. 137-155.
[94] D. B. Curtis, C. D. Hatch, C. A. Hasenkopf, O. B. Toon, M. A. Tolbert, C. P. McKay, and B. N. Khare, "Laboratory studies of methane and ethane adsorption and nucleation onto organic particles: Application to Titan's clouds," *Icarus,* vol. 195, pp. 792-801, Jun 2008.
[95] M. E. Wise, S. T. Martin, L. M. Russell, and P. R. Buseck, "Water uptake by NaCl particles prior to deliquescence and the phase rule," *Aerosol Science and Technology,* vol. 42, pp. 281-294, 2008.
[96] S. L. Girshick, N. P. Rao, and M. Kelkar, "Model for ion-induced nucleation based on properties of small ionic clusters," *Journal of Vacuum Science & Technology a-Vacuum Surfaces and Films,* vol. 14, pp. 529-534, MAR-APR 1996.
[97] I. Kusaka, Z. G. Wang, and J. H. Seinfeld, "Ion-induced nucleation: A density functional approach," *The Journal of Chemical Physics,* vol. 102, pp. 913-924, 1995.
[98] I. Kusaka, Z. G. Wang, and J. H. Seinfeld, "Ion-induced nucleation. II. Polarizable multipolar molecules," *The Journal of Chemical Physics,* vol. 103, pp. 8993-9009, 1995.
[99] L. C. Rorrer and R. A. Yost, "Solvent vapor effects on planar high-field asymmetric waveform ion mobility spectrometry," *International Journal of Mass Spectrometry,* vol. 300, pp. 173-181, Mar 2011.
[100] C. W. Tsai, R. A. Yost, and T. J. Garrett, "High-field asymmetric waveform ion mobility spectrometry with solvent vapor addition: a potential greener bioanalytical technique," *Bioanalysis,* vol. 4, pp. 1363-1375, Jun 2012.
[101] J. Fernandez de la Mora, "Heterogeneous Nucleation with Finite Activation Energy and Perfect Wetting: Capillary Theory Versus Experiments with

Nanometer Particles, and Extrapolations on the Smallest Detectable Nucleus," *Aerosol Science and Technology,* vol. 45, pp. 543-554, 2011/03/10 2011.
[102] T. Seto, K. Okuyama, L. deJuan, and J. Fernandez de la Mora, "Condensation of supersaturated vapors on monovalent and divalent ions on varying size," *Journal of Chemical Physics,* vol. 107, pp. 1576-1585, AUG 1 1997.
[103] A. G. Nasibulin, J. Fernandez de la Mora, and E. I. Kauppinen, "Ion-Induced Nucleation of Dibutyl Phthalate Vapors on Spherical and Nonspherical Singly and Multiply Charged Polyethylene Glycol Ions," *The Journal of Physical Chemistry A,* vol. 112, pp. 1133-1138, 2008/02/01 2008.
[104] R. Bahadur and L. M. Russell, "Water uptake coefficients and deliquescence of NaCl nanoparticles at atmospheric relative humidities from molecular dynamics simulations," *Journal of Chemical Physics,* vol. 129, Sep 7 2008.
[105] V. Talanquer and D. W. Oxtoby, "Formation of droplets on nonvolatile soluble particles," *Journal of Chemical Physics,* vol. 119, pp. 9121-9128, Nov 2003.
[106] D. R. Oberreit, P. H. McMurry, and C. J. Hogan, "Analysis of Heterogeneous Vapor Uptake by Nanoparticles via Differential Mobility Analysis-Drift Tube Ion Mobility Spectrometry (DMA-DTIMS)," *Submitted,* 2013.
[107] H. Ouyang, C. Larriba-Andaluz, D. R. Oberreit, and C. J. Hogan, "The Collision Cross Sections of Iodide Salt Cluster Ions in Air via Differential Mobility Analysis-Mass Spectrometry " *Journal of the American Society for Mass Spectrometry,* vol. In Press, pp. 10.1007/s13361-013-0724-8, 2013.
[108] C. J. Hogan and J. Fernandez de la Mora, "Ion-Pair Evaporation from Ionic Liquid Clusters," *Journal of the American Society for Mass Spectrometry,* vol. 21, pp. 1382-1386, Aug 2010.
[109] C. Larriba and C. J. Hogan, "Free Molecular Collision Cross Section Calculation Methods for Nanoparticles and Complex Ions with Energy Accommodation," *Journal of Computational Physics,* vol. 251, pp. 344-363, 2013.
[110] C. Larriba and C. J. Hogan, "Ion Mobilities in Diatomic Gases: Measurement vs. Prediction with Non-Specular Scattering Models," *The Journal of Physical Chemistry A,* vol. 117, pp. 3887-3901, 2013.
[111] H. Tammet, "Size and Mobility of Nanometer Particles, Clusters and Ions," *Journal of Aerosol Science,* vol. 26, pp. 459-475, APR 1995.
[112] J. B. Fenn, "Mass spectrometric implications of high-pressure ion sources," *International Journal of Mass Spectrometry,* vol. 200, pp. 459-478, 2000.
[113] M. F. Bush, R. J. Saykally, and E. R. Williams, "Formation of hydrated triply charged metal ions from aqueous solutions using nanodrop mass spectrometry," *International Journal of Mass Spectrometry,* vol. 253, pp. 256-262, 2006.
[114] B. K. Ku and J. Fernandez de la Mora, "Relation between Electrical Mobility, Mass, and Size for Nanodrops 1-6.5 nm in Diameter in Air," *Aerosol Science and Technology,* vol. 43, pp. 241-249, 2009.
[115] A. D. Becke, "Density-Functional Thermochemistry .3. The Role of Exact Exchange," *Journal of Chemical Physics,* vol. 98, pp. 5648-5652, Apr 1993.

[116] P. J. Hay and W. R. Wadt, "Ab initio Effective Core Potentials for Molecular Calculations - Potentials for the Transition-Metal Atoms Sc to Hg," *Journal of Chemical Physics*, vol. 82, pp. 270-283, 1985.
[117] P. J. Hay and W. R. Wadt, "Ab initio Effective Core Potentials for Molecular Calculations - Potentials from K to AU including the Outermost Core Orbitals," *Journal of Chemical Physics*, vol. 82, pp. 299-310, 1985.
[118] W. R. Wadt and P. J. Hay, "Ab initio Effective Core Potentials for Molecular Calcualtions - Potentials for Main Group Elements Na to Bi," *Journal of Chemical Physics*, vol. 82, pp. 284-298, 1985.
[119] Z. H. Li and D. G. Truhlar, "Nanosolids, slushes, and nanoliquids: Characterization of nanophases in metal clusters and nanoparticles," *Journal of the American Chemical Society*, vol. 130, pp. 12698-12711, Sep 2008.
[120] H. Ambaye and J. R. Manson, "Calculations of accommodation coefficients for diatomic molecular gases," *Physical Review E*, vol. 73, p. 031202, 2006.
[121] H. Ambaye and J. R. Manson, "Translational to rotational energy transfer in molecule-surface collisions," *The Journal of Chemical Physics*, vol. 125, pp. 084717-8, 2006.

Appendix A Particle Trajectory Simulation

This chapter describes a technique for modeling particle trajectories within a system using a combination of a commercially available computational fluid dynamics (CFD) package (*Ansys Fluent*) and two custom programs written in FORTRAN language. Ansys Fluent is used to calculate both the fluid flow field and any electrostatic gradients (if they are considered) within the system. Although Fluent has built in capability for particle trajectory simulations, it is not suited for large numbers of sampled particles. Therefore, the CFD results are exported from the program and used in a custom program (ParticleTrajectory.exe) to simulate particle trajectories. A second program (MovieMaker.exe) can then be used to visualize these trajectories. The following sections provide descriptions of the programs as well as instructions for using them..

A.1 Instructions for using Fluent User Defined Functions

These instructions outline how to create a model and use a user defined function to determine electrostatic field gradients. The user defined function file also includes enhancements to particle trajectory calculations done within Fluent. As they are not used extensively in the work presented here, these features will not be discussed in great detail. The instructions assume that the user is familiar with Ansys Fluent. For new users, tutorials on basic modeling, meshing and analysis are available through the Minnesota Super Computing Center.

A.1.1 Setting up a UDF Within Fluent

- Start a new project in Ansys Workbench.
- Drag the Fluid Flow (Fluent) icon to the Project Schematic window.
- On the right side pane check the Named Selections box and select 2D or 3D for the analysis type.
- Several tutorials are available for learning geometry and mesh formation in Ansys. To create a 2D surface select *concept-Surfaces From Sketches*. When creating 2D geometry the XY plane must be used and X axis is assumed to be the axis of symmetry for 2D axisymmetric problems.
- In the Ansys mesher create named edges or surfaces to indicate voltages in 2D or 3D models respectively.
- After opening the project in Fluent the model must be set up to use the UDFs.
    - First move the UDF source file into the Fluent directory that contains both the .cas and .dat files.
    - Select *Define-UserDefined-Functions-Compiled*. Under source files select add and pick the UDF source file. Select build to create a file for Fluent to use.
    - Select *Define-UserDefined-Function-Hooks*. Select edit next to adjust and add the *PotentialToGradient* option.
    - Select *Define-UserDefined-Scalars*, increase the number to 1, and select *PotentialField* under the Flux Function option. This creates a user defined scalar for solving the voltage field.

- Select *Define-UserDefined-Memory* and increase the number to 3. This provides locations for Fluent to store the voltage gradient fields in the three coordinates.

- When defining boundary conditions select the UDS tab, select specified value, and enter voltages. Keep inlets and insulators at 0 specified flux.

A.1.2 Using UDFs For Particle Tracking Within Fluent

- The particle tracking UDFs can be activated in the Model-Discrete Phase window. Note that to model Brownian motion the energy equation must be activated. The drag force model can be selected under the Tracking tab. The Brownian, Electrostatic, or a combination of both can be selected under the UDF tab in the Body Force section.
- Note: each time the model is opened, at least one iteration is required prior to tracking Discrete Phase Material (DPM).
- When tracking DPM with Brownian forces the number of tracks must often be increased to >1e7. It is recommended to increase the Coarsen option to ~1000 to reduce display rendering time.
- If the slip correction is constant the built in Brownian motion and drag models may be used. Note that it is necessary to select the Stokes-Cunningham drag law so the option of entering the correct slip correction for the modeled particle is available.

A.2 Modeling Porous Jump Surfaces in Fluent

Flow over porous surfaces such as screens can be modeled within Fluent using a 'porous jump'. The Fluent documentation outlines the method for calculating the porous jump pressure drop and the equation used to determine the required values is in Chapter 2. This section outlines the steps required to create the porous jump surface and to assign voltage values to it.

Modeling a Two Dimensional Porous Jump Surface

- Within modeler create a surface for one side of the mesh
- Create a second surface for the other side of the mesh and select 'add frozen' when creating the surface
- Select both surfaces and select *create new part*
- In the meshing module name the surface porous_jump_description
- In Fluent verify the boundary condition for the porous jump is correct

Modeling a potential at the Porous Jump

- In mesher create a narrow inflation layer (10 μm) at the porous jump surface
- In Fluent select *Adapt-Boundary*
- Select the porous jump surface and then select *Mark*
- Select *Mesh-Separate-Cells*
- In the cell zone conditions dialogue box a new zone will appear for the area near the porous jump. Select the cell zone and then select *Edit.*

- In the dialogue box select the *Fixed Values* box
- Select the *Fixed Values Tab* and scroll down to *User Scalar* and set the desired potential (note: if user scalar is not present select *Define-UserDefined-Scalars* and change it to 0. Select OK and then reset it to 1)

A.3 Using ParticleTracker.exe

The program *ParticleTracker.exe* simulates the trajectories of particles within a system using flow and electrostatic gradient Fields exported from Fluent. This section provides a brief overview of the algorithms used in the software and step by step instructions for using it.

ParticleTracker.exe Program Description

The trajectory of a particle in a system where forces due to Brownian motion are not negligible can be solved using the Langevin equation, given by[38]:

$$m_p\vec{v} = \vec{F} - m\beta(\vec{v} - \vec{u}) + \vec{X}$$

where m_p is the particle mass, v is the particle velocity, F is an outside acting force (such as electrostatic), β is the friction factor/particle mass, u is the gas velocity, and X is the random force. ParticleTracker uses the algorithm for solving the Langevin equation outlined by Ermak and Buckholz[38]:

$$\vec{v}_{n+1} = \vec{v}_n e^{-\beta\Delta t} + \frac{(f\vec{u}_n + \vec{F}_n)}{m_p \beta}(1 - e^{-\beta\Delta t}) + \vec{a}_1$$

$$\vec{a}_1 = \sqrt{\frac{k_B T}{m_p}\left(1 - e^{-2\beta\Delta t}\right)} X$$

$$x_{n+1} = \vec{x} + \frac{1}{\beta}\left(\vec{v}_{n+1} + \vec{v}_n - 2\frac{(f\vec{u}_n + \vec{F}_n)}{m_p \beta}\right)\frac{(1 - e^{-\beta\Delta t})}{\left(1 + e^{-\beta\Delta t}\right)} + \frac{(f\vec{u}_n + \vec{F}_n)}{m_p \beta}\Delta t + \vec{a}_2,$$

$$\vec{a}_2 = \frac{2k_B T}{m_p \beta^2}\left(\beta\Delta t - 2\frac{\left(1 - e^{-\beta\Delta t}\right)}{\left(1 + e^{-\beta\Delta t}\right)}\right)\left(1 - e^{-2\beta\Delta t}\right) X$$

where X is a Gaussian distributed random variable. At the start of the simulation a particle mobility is randomly sampled from an input distribution and is then assigned a random time during an initial seeding period. As a particle trajectory is tracked, the flow and electrostatic fields are determined by a weighted average of the three nearest neighbor cells. The program breaks up the input field data into sections so that for a given particle location, fewer nodes must be searched to find the nearest neighbor. At each time step the program also evaluates the particles proximity to a wall. If the particle is within a set distance from a wall, the timesteps begin to lower. Once the particle is within a capture distance it is considered as lost and the simulation ends. If the particle passes past a defined axial distance then it is considered as measured. The drift time is recorded and then assigned into a time bin. The program then assigns a random weighted detection time for each of the detectors in the input files. Throughout the simulation, several arrays are created which correspond to all of the particle locations at set time intervals. The number of these ‘frames’ is set by the input file and the time interval is equal to (seeding

time + total analysis time) / #frames. At the end of the simulation the program writes text files of the frame arrays (‘Frame #’.txt), a file containing the fate of each particle (TrackOutput.txt), and a file that reports the number of particles present in each time bin (FreqDist.txt). The FreqDist.txt file provides an arrival time distribution for no detector and using each of the CPCs. There is additional time added to account for diffusion broadening in the detector although under the experimental conditions, this value does not affect the shape or location of the calculated ATDs. The column headings for FreqDist.txt are (# is number of particles per bin): Time, # No Detector, # with 3786, # with 3786 and diffusion, # with 3788, # with 3788 and diffusion, # Considering only the Sample Exit tube (as a design tool).

The program reads five text files which contain the simulation parameters, the flow field exported from Fluent, a file to define zones, and two detector response time distributions. A brief description of the files and how to create them are as follows:

FlowField.txt

This file contains the geometry and solution data from Fluent. The file must first be exported from Fluent and then formatted using Excel.

- Within Fluent select *File-Export-Solution Data*
- Select *ASCII , Node,* and *Comma* for the filetype, location and delimiter
- In *Quantities* select *Axial Velocity, Radial Velocity, Mole Fraction air, User Memory 0, User Memory 1,* and *Cell Wall Distance*
- Select *Write* and create a filename with the .csv extension
- Open the file in Excel

- Reorder the columns as *nodenumber, x-coordinate, y-coordinate, axial-velocity, radial-velocity, udm-0, udm-1, molef-air, cell-wall-distance*
- Note the total number of nodes
- Sort the data by increasing *x-coordinate*
- Copy the data into a text file named *FlowField.txt*. Make sure that the end of the file has extra carriage returns removed

FlowZones.txt

This file is used to define how to divide the input data into zones to reduce the time required to locate the nearest neighbors.

- Open the sample file *FlowZones.txt*
- In the first row of the second column, set the starting axial location as the lowest value in your domain
- In the first row of the third column set the ending axial location of the first zone
- In the second row of the second column set the start of the second zone to a value slightly lower than the end of the first zone. This insures that if a particle is near a zone boundary it is weighted correctly.
- Repeat for the remaining zones
- Sample file:

1	-1.0	0.026	0	0
2	0.024	0.051	0	0
3	0.049	0.076	0	0
4	0.074	0.101	0	0
5	0.099	0.126	0	0
6	0.124	0.151	0	0
7	0.149	0.176	0	0
8	0.174	0.201	0	0
9	0.199	0.226	0	0
10	0.224	1.d3	0	0

Case.txt

This file defines the simulation conditions. The parameters are described in the sample file:

```
1000 ! Numpart = Number of simulated particles
150   ! Grabs= Number of frames captured during simulation
53773              ! Nodes = number of cells in Flow Field file minus 1
150   ! Numbin = Number of bins in freq dist
5.     !       tpop = 5. !time to populate inlet in seconds
10.    !       tmax=10. !maximum number of seconds for simulation
101300             ! pg = 101300 !Pa
1.983d-5 ! mu = Gas viscosity
298   ! Temp = Gas temp k
0.37d-9            ! dg = Gas molecule diameter
1d3   ! rhop = kg/m^3
1d-4    ! delt = the initial time step
.0001              !       distep=.0001 !distance between time steps used to adapt timestep
4.82d-3            !       tubedia=4.82e-3
-.22   !           zstart = initial locaiton of seeded particles
25000              !       inputmob = peak input mobility
1      !           xfer function type: 0 = triangular, 1 = gaussian
0      !           respow = resolving power of xfer function
3      ! nummode= Number of modes of input mobilities
25000              ! modehop = mobility jump between modes
1000 ! DMAV= Value to scale voltage, assumes that the model was created with 1kV at the highest potential
0.02d0   ! tbin = cponstant bin width (currently commented out)
1      ! Seeding 0=continuous, 1 = stop seeding after voltage is on
1      ! Charger 0=all particles neut, 1=all particles charged.
1.d14              ! Ion concentration (#/m^3)
```

CPC-3786.txt and CPC-3788.txt

These files contain the detector response time distribution data. The data are normalized to a peak value of 1.

3786		3788	
0	0	0.2	0
0.05	0	0.21	0
0.1	0	0.22	0
0.15	0	0.23	0
0.2	0	0.24	0
0.25	0	0.25	0.176470588
0.3	0	0.26	0.617647059
0.35	0	0.27	0.882352941
0.4	0	0.28	1
0.45	0	0.29	0.882352941
0.5	0	0.3	0.647058824
0.55	0	0.31	0.470588235
0.6	0	0.32	0.264705882
0.65	0	0.33	0.205882353
0.7	0.025	0.34	0.147058824
0.75	0.375	0.35	0.117647059
0.8	0.85	0.36	0.088235294

0.85	1	0.37	0.058823529
0.9	0.875	0.38	0.044117647
0.95	0.625	0.39	0.044117647
1	0.35	0.4	0.044117647
1.05	0.225	0.41	0.029411765
1.1	0.175	0.42	0.029411765
1.15	0.1	0.43	0.014705882
1.2	0.075	0.44	0.005882353
1.25	0.05	0.45	0.011764706
1.3	0.05	0.46	0.011764706
1.35	0.05	0.47	0.011764706
1.4	0.0375	0.48	0.011764706
1.45	0.025	0.49	0.011764706
1.5	0.025	0.5	0.011764706
1.55	0.025	0.51	0.011764706
1.6	0.025	0.52	0.011764706
1.65	0.025	0.53	0.011764706
1.7	0.0125	0.54	0.005882353
1.75	0	0.55	0
1.8	0	0.56	0
1.85	0	0.57	0
1.9	0	0.58	0
1.95	0	0.59	0
2	0	0.6	0

A.4 Using MovieMaker.exe

MovieMaker.exe creates bitmap images of frames created by ParticleTracker.exe that can then be used to generate video files using a videom editor program such as EnVe (Computational Engineering International Inc.). The program reads the same Case.txt and FlowField.txt files used in ParticleTracker.exe. The program also reads the frame array files generated by ParticleTracker.exe (named 'FrameNumber'.txt) and the arrival time distribution file (FreqDist.txt). The program also uses a file named Pathlines.txt which contains trajectories of uncharged particles released at the drift flow inlet of the DTIMS. The pathlines file is created by modifying ParticleTracker.exe to output particle position data to FreqDist.txt. The program reads the file and displays every third particle point for a frame and then steps to the next particle point at each subsequent frame step. The instrument boundaries are shown by plotting nodes within a set minimum wall distance.

A.5 Using DTIMS Analytical.exe

The program DTIMS Analytical.exe applies the equations described in Section 2.2. The program reads in Case.txt, CPC-3786.txt, and CPC-3788.txt and then uses a stochastic process to randomly assign drift times, residence time in the sample outlet tube, and detector times. The program also stochastically removes particles from the simulation due to diffusion losses to the screen or tubing. The output file FreqDist.txt is in the same format as described in the ParticleTracker.exe description.

A.6 LabVIEW program and Excel template

The LabVIEW program used to operate the DTIMS uses a National Instruments USB DAQ model 6008 or 6009 to control the high voltage relay, set the mass flow controllers, and acquire counts from the detector. The program is also capable of controlling the high voltage on the Bertan power supply although if voltage ramping isn't used the voltage can be set directly on the supply.

To improve counting statistics, several scans can be made for a measurement. The counts per unit time in the given time interval are recorded using the real measurement time. While, the software attempts to record the bins at set intervals, there often is a slight random discrepancy. This discrepancy is accounted for by an Excel template which determines the counts per set time bin using linear interpolation of the measured data. The Excel template can also be used to find the peak arrival time by least squared fitting a weighted Gaussian curve to the data. To perform the fitting, use the built in Excel

solver to adjust the peak arrival time and standard deviation to set the least squares sum cell equal to zero.

A.7 Source Code – Analytical Solver

```
! DTIMS Analytical Simulation
! Written by Derek Oberreit 2/2013
! This program reads a flow field from Fluent and then performs Langevin tracking of
particles
! The flow field file should be organizied by: num,zpos,rpos,zvel,rvel,Ez,Er,Inlet mole
fraction, Cell wall distance
! The order of the flow field file should be incrementing x pos then y pos

    Program main
    Implicit none
    Double Precision, Allocatable :: Location(:,:,:)
    Double Precision, Allocatable :: FlowField(:,:)
    Double Precision, Allocatable :: FreqDist(:,:)
    Double Precision, Dimension(0:40,0:1) :: CPC86,CPC88 !Format starting at 0
    Double Precision FlowZones(0:9,0:4)
    Character*50 filename
    Integer numpart, grabs, nodes, numbin, seeding, Charger,nq !Variable Integers
    Integer n,m,i,j,k !Incrementing integers for general loops
    Integer NodeNum,Col,Row,s,zn,nbin,sframe !Incrementing integers
    Integer good !Logical integer
    Double Precision tmax,delt,t,tpop, tbin !Variables for timing
    Double Precision twrite,dwrite !Variables for Pathlines
    Double Precision
inputmob,measmob,respow,randshift,sampcent,tubedia,zstart,nummode,modehop,xfertype
!Variables to define inlet particles
    Double Precision dp, cc, mp, ff, rhop, beta , sigma1, sigma2 !Particle variables
    Double Precision pg, mu, Temp, ng, dg, mg, lambda, kn !Gas variables
    Double Precision xp,yp,zp,rp,vxp,vyp,vzp,vrp,xi,yi,zi,ri !Particle position variables
    Double precision xpo,ypo,zpo,distep !Particle position placeholders
    Double Precision ux,uy,uz,ur,fx,fy,fz,fr,theta,DMAV,DMAon ! Flowfield variables
    Integer nn1,nn2,nn3 !Row locations of nearest nodes
    Double Precision dist,cn1,cn2,cn3,nr1,nr2,nr3 !Distances to nearest nodes
    Double Precision tcpc, tdiff !CPC time broadening variables
    Double Precision kb, pi, ex, q !Fixed constants
    Double Precision mij,fij,mj,fj,aj,Knd,nuc,nufm,eps0,epsp,psiI,betaij,Hogan,nion,tcoll
!Charging variables
    Double precision udrift, delx, L, RDT, tave, PsiE, Pe, deltdr, delt0, sigma, qdet,
Lsamp,qsamp, muGK, tsamp, deltRM, Ldrift

        ! Constants
        kb = 1.380658d-23 !Boltzman constant
        pi = 3.14159d0
        ex = 2.71828d0
        q=1.602d-19 !positve for positive voltages
        mg = 28.97d-3/6.02d23

        udrift = .00265
        delx = .008
        L = .227 !meters, length of drift region for field.
        Ldrift = .224
        Ldrift = Ldrift-0.5*delx
        Qdet=.615 !lpm
        Lsamp = .163 !meters
        Qsamp = 0.8 !Lpm


        Open(1,File="Case.txt") !Open file containing case information
```

```
        ! Assign array dimensions based on case info
        Read(1,*) numpart
        Read(1,*) grabs
        Read(1,*) nodes
        Read(1,*) numbin
        Allocate (Location(0:(numpart-1),0:5,0:grabs))
        Allocate (FlowField(0:nodes,0:8))
        Allocate (FreqDist(0:numbin,0:6))
        Read(1,*) tpop !time to populate inlet in seconds
        Read(1,*) tmax !maximum number of seconds for simulation
        Read(1,*) pg
        Read(1,*) mu !Gas viscosity
        Read(1,*) Temp !Gas temp k
        Read(1,*) dg !Gas molecule diameter
        ! Calculate gas variables
        ng = pg/kb/Temp
        lambda = 1/2**.5/pi/dg**2/ng !mean free path
        Read(1,*) rhop !Particle density
        Read(1,*) delt !
        Read(1,*) distep !distance between time steps
        Read(1,*) tubedia !
        Read(1,*) Zstart

        Read(1,*) inputmob !
        Read(1,*) xfertype !0=triangular, 1=gaussian
        Read(1,*) respow !
        Read(1,*) nummode
        Read(1,*) modehop
        Read(1,*) DMAV
        Read(1,*) tbin !only used for constant bin width
        Read(1,*) Seeding
        Read(1,*) Charger
        Read(1,*) nion
        Call system_clock(s) !Get system time
        Call srand(s) !Seed random number generator with system time
        OPEN (13,FILE="CPC-3786.txt", STATUS='old')
        Read (13,*) ((CPC86(row,col),col=0,1), row=0,40)
        OPEN (14,FILE="CPC-3788.txt", STATUS='old')
        Read (14,*) ((CPC88(row,col),col=0,1), row=0,40)
        Open (17,File="TrackOutput.txt", Status='unknown')
!       open (18,File='FreqDist.txt', Status='unknown')
       Open (20,File="Inputdist.txt", Status='unknown')



       tmax = .227**2*inputmob/DMAV+5.
       tmax=L**2./(DMAV/inputmob-udrift*L)+5.


       Do i=0,(numbin)
!       FreqDist(i,0)=i*tbin !Initialize freq dist output with timestamp
        Do j=1,6
        FreqDist(i,j)= 0.
        end do

       FreqDist(i,0)= 10.**((log10(tmax)+1.)/(numbin-1.)*i-1.) !Initialize freq dist
output with timestamp
       end do

       Do i=0,(numpart-1)

       twrite=0

       nbin=0 !Current bin location
       sampcent=0

       good=0
```

```
       measmob=inputmob+modehop*int(nummode*rand())
       if (respow.ne.0) then
        good = 0
          do while (good.eq.0)
          if (xfertype.eq.0) then
          randshift = rand()-0.5
          if (randshift .gt. 0) then
           if (rand().lt.randshift*(-2.)+1) then
           measmob=randshift*measmob/respow*2.+measmob
           good=1
           endif
          else
           if (rand().lt.randshift*2.+1) then
           measmob=randshift*measmob/respow*2.+measmob
           good = 1
           endif
         endif
         else if (xfertype.eq.1) then
         measmob=measmob/respow/2./sqrt(2.*log(2.))*sqrt(-
2.*log(rand()))*cos(2*pi*rand())+measmob
         good=1
         endif
         end do
        endif
         write (20,*) measmob, xi,yi,zi

       ff = measmob*q
       dp = sqrt(measmob*3./4./pg*sqrt(2*kB*Temp/mg/pi)*q/1.36)+dg
       mp = rhop/6d0*pi*dp**3
       beta = ff/mp
       good = 1
            muGK=pi*kb*Temp*Lsamp/measmob/(Qsamp/60./1000.)/q
            if (muGK.lt.0.02)then
            if (rand().GT.(1.-2.56*muGK**(2./3.)+1.2*muGK+.1767*mu**(4./3.))) then
              write (6,*) t,i,' tube diff 1', dp,mu, 1-
2.56*muGK**(2./3.)+1.2*muGK+.1767*mu**(4./3.)
             write (17,'(1x,7e11.3,A)') t,xi,yi,zi,xp,yp,zp,' tube diff'
             good = 0
            endif
            else
            if (rand().GT. .819*exp(-3.66*muGK)+.0975*exp(-22.3*muGK)+.0325*exp(-
57.0*muGK)) then
              write (6,*) t,i,' tube diff 2', dp,mu, .819*exp(-3.66*muGK)+.0975*exp(-
22.3*muGK)+.0325*exp(-57.0*muGK)
             write (17,'(1x,7e11.3,A)') t,xi,yi,zi,xp,yp,zp,' tube diff'
             good = 0
             endif
            endif

            if (good .eq. 1) then
            if (rand().gt.exp(-10.8*.12*5e-4*(4*2.54e-4/kb/temp*ff)**(-2./3.)/pi/(1-
.12)/2.54e-4))then
             write (6,*) t,i,' screen diff', dp, exp(-10.8*.12*5e-4*(4*2.54e-
4/kb/temp*ff)**(-2./3.)/pi/(1-.12)/2.54e-4)
             write (17,'(1x,7e11.3,A)') t,xi,yi,zi,xp,yp,zp,' screen diff'
             good = 0
            endif
            endif

            if (good.eq.1)then
            tave=L**2./(DMAV/measmob-udrift*L)
            tave=L*Ldrift/(DMAV/measmob-udrift*L)
            delt0=delX*L/(DMAV/measmob-udrift*L)
            psiE = q*DMAV/kb/Temp
            Pe = udrift*L*q*measmob/kb/temp
            Pe = udrift*Ldrift*q*measmob/kb/temp
            RDT = 1./sqrt((delx/L)**2.+16.*log(2.)/(psiE-Pe))
            RDT = 1./sqrt((delx/Ldrift)**2.+16.*log(2.)/(psiE-Pe))
```

```
            deltdr =sqrt(delt0**2. +16.*log(2.)*tave*2./(psiE-Pe))
            delTRM = sqrt(delt0**2. +16.*log(2.)*tave*2.*kb*temp/dmaV/q)
            write (6,*) deltdr, deltRM, RDT, delt0, 16.*log(2.)*tave*2.*kb*temp/dmaV/q
            sigma = deltdr/2./sqrt(2.*log(2.))
            t=sigma*sqrt(-2d0*LOG(rand()))*cos(2*pi*rand())+tave !Box Meuller transform
!            t=t+.1/((Qdet/60./1000.)/.25/pi/tubedia**2.) ! Detector tube delay. Tube
length 0.1m.
            good=0
            do while (good.eq.0)
            rp=(rand()-0.5)*tubedia
            good = int((rp/tubedia*2.-(rp/tubedia*2.)**3.)/1.5396/rand())
            end do
            tsamp = .1/(2*((Qdet/60./1000.)/.25/pi/tubedia**2.)*(1.-(rp/tubedia*2.)**2))
 !          t=t+.1/((Qdet/60./1000.)/.25/pi/tubedia**2.) ! Detector tube delay. Tube
length 0.1m.
            t=t+tsamp
            nbin=nint((log10(t)+1.)*(numbin-1.)/(log10(tmax)+1.))
!            nbin=int(t/tbin)
            FreqDist(nbin,1)=FreqDist(nbin,1)+1.
            CALL CPCResponse(CPC86,tcpc,tdiff,temp,ff)
!            nbin=int((t+tcpc)/tbin)
            nbin=nint((log10(t+tcpc)+1.)*(numbin-1.)/(log10(tmax)+1.))
            FreqDist(nbin,2)= FreqDist(nbin,2)+1.
!            nbin=int((t+tcpc+tdiff)/tbin)
           nbin=nint((log10(t+tcpc+tdiff)+1.)*(numbin-1.)/(log10(tmax)+1.))
            FreqDist(nbin,3)=FreqDist(nbin,3)+1.
            CALL CPCResponse(CPC88,tcpc,tdiff,temp,ff)
!            nbin=int((t+tcpc)/tbin)
            nbin=nint((log10(t+tcpc)+1.)*(numbin-1.)/(log10(tmax)+1.))
            FreqDist(nbin,4)= FreqDist(nbin,4)+1.
!            nbin=int((t+tcpc+tdiff)/tbin)
           nbin=nint((log10(t+tcpc+tdiff)+1.)*(numbin-1.)/(log10(tmax)+1.))
            FreqDist(nbin,5)=FreqDist(nbin,5)+1.
!           nbin=nint((log10(tsamp)+1.)*(numbin-1.)/(log10(tmax)+1.))
!            FreqDist(nbin,6)=FreqDist(nbin,6)+1.
            write (6,*) t,nbin,i,' good'
            write (17,'(1x,10e11.3,A)') t,xi,yi,zi,xp,yp,zp,tcpc,tdiff,tsamp

            end if
       end do !time run


       OPEN (18,FILE='FreqDist.txt', status='unknown')
       write (18,'(1x,6e12.4)') ((FreqDist(i,j), j=0,5),i=0,numbin)
       close (18)

stop
end program

       SUBROUTINE GAUSSRAND(psi)
       double precision psi
       integer i
       psi=0
       do i=1,12
       psi=(rand()+psi)
       end do
       psi=psi-6
       end


       SUBROUTINE CPCResponse(CPC,tcpc,tdiff,temp,ff)
        Double Precision CPC(0:40,0:1)
        integer good, icpc
        double precision tcpc, mcpc, pcpc,tdiff
        double precision kb,temp,ff,pi
        kb = 1.380658d-23
        pi = 3.14159
            good=0
```

```
            do while (good.eq.0)
             tcpc=rand()*40
             icpc=int(tcpc)
             mcpc=(cpc((icpc+1),1)-cpc(icpc,1))
             pcpc=mcpc*tcpc+(cpc(icpc,1)-mcpc*icpc)
             if (rand().LT.pcpc) then
             good=1
             tcpc=(tcpc-icpc)*(cpc((icpc+1),0)-cpc(icpc,0))+cpc(icpc,0)
             tdiff=4*(kb*temp/ff*tcpc)**(0.5)*(LOG(2.))**(0.5)*sqrt(-
2d0*LOG(rand()))*cos(2*pi*rand())/.28*tcpc !where is .28 from?
             tdiff=2*(kb*temp/ff*tcpc)**(0.5)*sqrt(-2d0*LOG(rand()))*cos(2*pi*rand()) !I
think this is more correct
             end if
            end do
        END
```

A.8 Source Code – ParticleTracker.exe

```
! Particle Trajectories
! Written by Derek Oberreit 2/2013
! This program reads a flow field from Fluent and then performs Langevin tracking of
particles
! The flow field file should be organizied by: num,zpos,rpos,zvel,rvel,Ez,Er,Inlet mole
fraction, Cell wall distance
! The order of the flow field file should be incrementing x pos then y pos

    Program main
    Implicit none
    Double Precision, Allocatable :: Location(:,:,:)
    Double Precision, Allocatable :: FlowField(:,:)
    Double Precision, Allocatable :: FreqDist(:,:)
    Double Precision, Dimension(0:40,0:1) :: CPC86,CPC88 !Format starting at 0
    Double Precision FlowZones(0:9,0:4)
    Character*50 filename
    Integer numpart, grabs, nodes, numbin, seeding, Charger,nq !Variable Integers
    Integer n,m,i,j,k !Incrementing integers for general loops
    Integer NodeNum,Col,Row,s,zn,nbin,sframe !Incrementing integers
    Integer good !Logical integer
    Double Precision tmax,delt,t,tpop, tbin !Variables for timing
    Double Precision twrite,dwrite !Variables for Pathlines
    Double Precision
inputmob,measmob,respow,randshift,sampcent,tubedia,zstart,nummode,modehop,xfertype
!Variables to define inlet particles
    Double Precision dp, cc, mp, ff, rhop, beta , sigma1, sigma2 !Particle variables
    Double Precision pg, mu, Temp, ng, dg, mg, lambda, kn !Gas variables
    Double Precision xp,yp,zp,rp,vxp,vyp,vzp,vrp,xi,yi,zi,ri !Particle position variables
    Double precision xpo,ypo,zpo,distep !Particle position placeholders
    Double Precision ux,uy,uz,ur,fx,fy,fz,fr,theta,DMAV,DMAon ! Flowfield variables
    Integer nn1,nn2,nn3 !Row locations of nearest nodes
    Double Precision dist,cn1,cn2,cn3,nr1,nr2,nr3 !Distances to nearest nodes
    Double Precision tcpc, tdiff !CPC time broadening variables
    Double Precision kb, pi, ex, q !Fixed constants
    Double Precision mij,fij,mj,fj,aj,Knd,nuc,nufm,eps0,epsp,psiI,betaij,Hogan,nion,tcoll
!Charging variables
    Double Precision CPCerr, driftErr, inputmobErr

        ! Constants
        kb = 1.380658d-23 !Boltzman constant
        pi = 3.14159d0
        ex = 2.71828d0
        q=1.602d-19 !positve for positive voltages
        mg = 28.97d-3/6.02d23
```

```
        Open(1,File="Case.txt") !Open file containing case information
        ! Assign array dimensions based on case info
        Read(1,*) numpart
        Read(1,*) grabs
        Read(1,*) nodes
        Read(1,*) numbin
        Allocate (Location(0:(numpart-1),0:5,0:grabs))
        Allocate (FlowField(0:nodes,0:8))
        Allocate (FreqDist(0:numbin,0:5))
        Read(1,*) tpop !time to populate inlet in seconds
        Read(1,*) tmax !maximum number of seconds for simulation
        Read(1,*) pg
        Read(1,*) mu !Gas viscosity
        Read(1,*) Temp !Gas temp k
        Read(1,*) dg !Gas molecule diameter
        ! Calculate gas variables
        ng = pg/kb/Temp
        lambda = 1/2**.5/pi/dg**2/ng !mean free path
        Read(1,*) rhop !Particle density
        Read(1,*) delt !
        Read(1,*) distep !distance between time steps
        Read(1,*) tubedia !
        Read(1,*) Zstart

        Read(1,*) inputmob !
        Read(1,*) xfertype !0=triangular, 1=gaussian
        Read(1,*) respow !
        Read(1,*) nummode
        Read(1,*) modehop
        Read(1,*) DMAV
        Read(1,*) tbin !only used for constant bin width
        Read(1,*) Seeding
        Read(1,*) Charger
        Read(1,*) nion
        Read(1,*) CPCerr
        Read(1,*) DriftErr
        Read(1,*) inputmobErr
        Call system_clock(s) !Get system time
        Call srand(s) !Seed random number generator with system time
        OPEN (13,FILE="CPC-3786.txt", STATUS='old')
        Read (13,*) ((CPC86(row,col),col=0,1), row=0,40)
        OPEN (14,FILE="CPC-3788.txt", STATUS='old')
        Read (14,*) ((CPC88(row,col),col=0,1), row=0,40)
        OPEN (15,FILE="FlowField.txt", STATUS='old')
        Read (15,*) ((FlowField(NodeNum,Col), Col=0,8), NodeNum=0,nodes)
        OPEN (16,FILE="FlowZones.txt", STATUS='old')
        Read (16,*) ((FlowZones(Row,Col), Col=0,4), Row=0,9)
        Open (17,File="TrackOutput.txt", Status='unknown')
!       open (18,File='FreqDist.txt', Status='unknown')
       Open (19,File="FlowZonesMod.txt", Status='unknown')
       Open (20,File="Inputdist.txt", Status='unknown')

       tmax = .227**2*inputmob/DMAV+5.
       tmax=.227**2./(DMAV/inputmob-.00265*.227)+5.
       tmax=.227**2./(DMAV/(inputmob+modehop*(nummode-1.))-.00265*.227)+5.
       tmax=.227**2./(DMAV/(inputmob*inputmoberr+modehop*(nummode-1.))-
(.00265*drifterr)*.227)+5.
       write (6,*) 'tmax=', tmax
    write (*,*) tmax
       Do i=0,9 !Assign row values to FlowZones
       Do j=0,nodes
       if (Flowfield(j,1).lt.FlowZones(i,1)-.001) then
        FlowZones(i,3)=j
        endif
       if (Flowfield(j,1).lt.Flowzones(i,2)+.001) then
       Flowzones(i,4)=j
```

```
       endif
       end do
       end do

       do row=0,9
       write (19,*)(FlowZones(Row,Col),Col=0,4)
!       write (6,*) (FlowZones(Row,Col), Col=0,4)
       end do
       Do n=0,grabs
        Do i=0,(numpart-1)
           location(i,1,n)=-.22
       end do
       end do


       Do i=0,(numbin)
!       FreqDist(i,0)=i*tbin !Initialize freq dist output with timestamp
        Do j=1,5
        FreqDist(i,j)= 0.
        end do

       FreqDist(i,0)= 10.**((log10(tmax)+1.)/(numbin-1.)*i-1.) !Initialize freq dist
output with timestamp
       end do

       Do i=0,(numpart-1)
       DMAon=0.
       nq = int(charger)
       if (seeding.eq.0) then
       t=rand()*(tmax+tpop)-tpop
       else
       t=rand()*tpop-tpop
       endif
!       t=0 !uncomment for pathlines
       twrite=0
       vxp=0
       vyp=0
       vzp=0
       nbin=0 !Current bin location
       sampcent=0
       zp=zstart
       good=0
       do while (good.eq.0)
!       xp=(rand()-0.5)*tubedia
!       yp=(rand()-0.5)*tubedia
!        yp=0 !use for rake
!       rp=sqrt(xp**2+yp**2)
!       good=int(tubedia/rp/2.) !verify particle lies in tube
!        good=int((2.*(rp/tubedia/2.)**2-(rp/tubedia/2.)**4)/rand())
        rp=(rand()-0.5)*tubedia
        good = int((rp/tubedia*2.-(rp/tubedia*2.)**3.)/1.5396/rand())
        end do
        theta=rand()*2*pi
        xp=rp*cos(theta)
        yp=rp*sin(theta)
!       zp=.226 !uncomment for pathlines
!       yp=0. !uncomment for pathlines
!       xp=sqrt( (i+1.)/numpart)*(.019-.004)+.004 !uncomment for pathlines
!              rp=sqrt(xp**2+yp**2)!uncomment for pathlines
       xi=xp
       yi=yp
       zi=zp
       ri=rp
       measmob=inputmob+modehop*int(nummode*rand())
       if (respow.ne.0) then
        good = 0
          do while (good.eq.0)
          if (xfertype.eq.0) then
```

```
          randshift = rand()-0.5
          if (randshift .gt. 0) then
           if (rand().lt.randshift*(-2.)+1) then
           measmob=randshift*measmob/respow*2.+measmob
           good=1
           endif
          else
           if (rand().lt.randshift*2.+1) then
           measmob=randshift*measmob/respow*2.+measmob
           good = 1
           endif
         endif
         else if (xfertype.eq.1) then
         measmob=measmob/respow/2./sqrt(2.*log(2.))*sqrt(-
2.*log(rand()))*cos(2*pi*rand())+measmob
         good=1
         endif
         end do
        endif
        measmob=measmob*inputmoberr
         write (20,*) measmob, xi,yi,zi

       ff = measmob*q
       dp = sqrt(measmob*3./4./pg*sqrt(2*kB*Temp/mg/pi)*q/1.36)+dg
       mp = rhop/6d0*pi*dp**3
       beta = ff/mp
       good = 0

      call NearestNode
(FlowZones,Flowfield,nodes,zp,rp,cn1,cn2,cn3,nn1,nn2,nn3,nr1,nr2,nr3)
       vzp= nr1*Flowfield(nn1,3)+nr2*Flowfield(nn2,3)+nr3*Flowfield(nn3,3)
       vrp= nr1*Flowfield(nn1,4)+nr2*Flowfield(nn2,4)+nr3*Flowfield(nn3,4)
       vxp=vrp
       vyp=vrp
       Do while (t.lt.tmax)
        if (t.gt.0) then
        DMAon=1.
!        DMAV=0 !uncomment for pathlines
!        Keep particles from flying away too fast at the start of the voltage field
        if (good.eq.0) then
        delt = .0001
!        delt= .001 !uncomment for pathlines
        good=1
        endif
        endif

        call
NearestNode(FlowZones,Flowfield,nodes,zp,rp,cn1,cn2,cn3,nn1,nn2,nn3,nr1,nr2,nr3)
        theta=ATAN2(yp,xp)


       uz= nr1*Flowfield(nn1,3)+nr2*Flowfield(nn2,3)+nr3*Flowfield(nn3,3)
       ur= nr1*Flowfield(nn1,4)+nr2*Flowfield(nn2,4)+nr3*Flowfield(nn3,4)
       ux=ur*COS(theta)
       uy=ur*SIN(theta)
        tcoll=1
       if (nq.eq.0) then
        if (rp.gt. .0095) then
         if (Flowfield(nn1,7).LT..5) then
          eps0 = 8.854e-12
                epsp = 10.
            PsiI = ((epsp-1)/(epsp-2))*q**2./(4.*pi*eps0*kb*Temp*dp/2.)
            nuc=1+0.3475*psiI**0.3802
            nufm=1+1.2534*psiI**.5
            mj = 100*1.66d-27
            fj = q/.0001
            mij = (mp*mj)/(mp+mj)
            fij = (ff*fj)/(ff+fj)
```

```
            knd=(kb*Temp*mij*nuc)**0.5/(fij*dp/2.*nufm)

Hogan=(4.*pi*knd**2.+25.836*knd**3.+(8*pi)**.5*11.211*knd**4)/(1+3.502*knd+7.211*knd**2.+
11.211*knd**3.)
            Hogan = (8*pi)**.5*KnD
            Betaij = Hogan*fij*(dp/2)**3.*nufm**2./(mij*nuc)
!            nion = 1.d12
            tcoll = 1./(Betaij*nion)
            nq=int(rand()*(1+delt/tcoll))
!            write (6,*) PsiI,nuc,nufm,mij,fij,knd,hogan,betaij,tcoll
!         nq=int(rand()*1.01)

          end if
          end if
          end if


       fz= (nr1*Flowfield(nn1,5)+nr2*Flowfield(nn2,5)+nr3*Flowfield(nn3,5))*nq*(-
q)*dmaV*DMAon/1000.
       fr= (nr1*Flowfield(nn1,6)+nr2*Flowfield(nn2,6)+nr3*Flowfield(nn3,6))*nq*(-
q)*dmaV*DMAon/1000.


       fx=fr*COS(theta)
       fy=fr*SIN(theta)
           sigma1=(kb*Temp/mp*(1.-ex**(-2.*beta*delt)))**(0.5)
           sigma2=(2.*kb*Temp/mp/(beta**2)*(beta*delt-2.*(1.-ex**(-beta*delt))/(1+ex**(-
beta*delt))))**(0.5)
!    sigma1=0 !uncomment for pathlines
!    sigma2=0 !uncomment for pathlines
!          Set original particle locations
           xpo=xp
           ypo=yp
           zpo=zp
           Call LANGEVIN(xp,vxp,sigma1,sigma2,Beta,delt,ff,mp,ux,fx)
           Call LANGEVIN(yp,vyp,sigma1,sigma2,Beta,delt,ff,mp,uy,fy)
           Call LANGEVIN(zp,vzp,sigma1,sigma2,Beta,delt,ff,mp,uz,fz)

!          Call VelVer(xp,vxp,delt,ff,mp,ux,fx)
!          Call VelVer(yp,vyp,delt,ff,mp,uy,fy)
!          Call VelVer(zp,vzp,delt,ff,mp,uz,fz)

           dist=((xpo-xp)**2+(ypo-yp)**2+(zpo-zp)**2)**0.5
           if ((cn1+cn2+cn3) .lt. distep) then
           delt = delt*(cn1+cn2+cn3)/dist
!           write(6,*) delt, (cn1+cn2+cn3)/3.
           else if (Flowfield(nn1,8).le.dist)then
            delt = delt*Flowfield(nn1,8)/10./dist
            else
             delt = delt*distep/dist
           endif
           if (nq.eq.0) then
            if (tcoll.lt.delt)then
            delt = tcoll/2.
!            write (6,*) tcoll
            endif
            endif
           rp=SQRT(xp**2+yp**2)
!            if ((t-twrite).gt..01) then
            dwrite=dwrite+dist
            if (dwrite.gt..002) then
!        write(17,'(1x,7e11.3,A)')t,zp,rp,uz,ur,fz,fr,' track'
        twrite=t
        dwrite=0
        endif

            sframe = (int((t+tpop)/(tmax+tpop)*grabs))
            location(i,0,sframe)=i
```

```
            location(i,1,sframe)=zp
            location(i,2,sframe)=rp
            location(i,3,sframe)=measmob
            location(i,4,sframe)=t
            location(i,5,sframe)=nq
            t=t+delt

            if (sign(1.d0,zpo)+sign(1.d0,zp).eq.0.) then
            if (rand().gt.exp(-10.8*.12*5e-4*(4*2.54e-4/kb/temp*ff)**(-2./3.)/pi/(1-
.12)/2.54e-4))then
             write (6,*) t,i,' screen diff', dp, exp(-10.8*.12*5e-4*(4*2.54e-
4/kb/temp*ff)**(-2./3.)/pi/(1-.12)/2.54e-4)
             write (17,'(1x,7e11.3,A)') t,xi,yi,zi,xp,yp,zp,' screen diff'
             exit
            endif
            endif


            if(t>=tmax) then !Verify particle not in wall, should be ,292
            write (6,*) t,i,' timeout', dp
           write (17,'(1x,7e11.3,A)') t,xi,yi,zi,xp,yp,zp, ' timeout'
            endif

            if (Flowfield(nn1,8).le..00001)then
                write (6,*) t,i,' wall', dp
                write (17,'(1x,7e11.3,A)') t,xi,yi,zi,xp,yp,zp,' wall'
                exit
            endif

            if (zp.gt..227)then
                if (rp.gt..003) then
                    write (6,*) t,i,'end screen', dp
                write (17,'(1x,7e11.3,A)') t,xi,yi,zi,xp,yp,zp,'end screen'
                    exit
                endif
            endif

            if(zp>.341) then !Verify particle not in wall, should be ,292

            nbin=nint((log10(t)+1.)*(numbin-1.)/(log10(tmax)+1.))
!            nbin=int(t/tbin)
            FreqDist(nbin,1)=FreqDist(nbin,1)+1.
            CALL CPCResponse(CPC86,tcpc,tdiff,temp,ff,cpcerr)
!            nbin=int((t+tcpc)/tbin)
            nbin=nint((log10(t+tcpc)+1.)*(numbin-1.)/(log10(tmax)+1.))
            FreqDist(nbin,2)= FreqDist(nbin,2)+1.
!            nbin=int((t+tcpc+tdiff)/tbin)
          nbin=nint((log10(t+tcpc+tdiff)+1.)*(numbin-1.)/(log10(tmax)+1.))
            FreqDist(nbin,3)=FreqDist(nbin,3)+1.
            CALL CPCResponse(CPC88,tcpc,tdiff,temp,ff,cpcerr)
!            nbin=int((t+tcpc)/tbin)
            nbin=nint((log10(t+tcpc)+1.)*(numbin-1.)/(log10(tmax)+1.))
            FreqDist(nbin,4)= FreqDist(nbin,4)+1.
!            nbin=int((t+tcpc+tdiff)/tbin)
          nbin=nint((log10(t+tcpc+tdiff)+1.)*(numbin-1.)/(log10(tmax)+1.))
            FreqDist(nbin,5)=FreqDist(nbin,5)+1.
            write (6,*) t,nbin,i,' good'
            write (17,'(1x,9e11.3,A)') t,xi,yi,zi,xp,yp,zp,tcpc,tdiff
            exit
            endif

       end do !time run
       Do n=sframe,grabs !fill rest of frames with particle location
            location(i,0,n)=i
            location(i,1,n)=zp
            location(i,2,n)=rp
            location(i,3,n)=measmob
            location(i,4,n)=t
```

```
            location(i,5,n)=nq

       end do
       end do

       do n=0,grabs
        write (filename,*) n,'.txt'
        open (18,File=filename,status='unknown')
         write (18,'(1x,6e12.4)') ((Location(i,j,n), j=0,5),i=0,(numpart-1))
        close (18)
        write (filename,*) n,'.bmp'


!
write(filename,'(a,1e12.2,a,1e12.4,a,1e12.4,a)')'Mob',measmob,'Dp',Dp,'DMAV',DMAV,'.csv'
!       OPEN (18,FILE=filename, status='unknown')
       OPEN (18,FILE='FreqDist.txt', status='unknown')
       write (18,'(1x,6e12.4)') ((FreqDist(i,j), j=0,5),i=0,numbin)
       close (18)
       end do


stop
end program

       SUBROUTINE GAUSSRAND(psi)
       double precision psi
       integer i
       psi=0
       do i=1,12
       psi=(rand()+psi)
       end do
       psi=psi-6
       end

        Subroutine NearestNode
(FlowZones,Flowfield,nodes,zp,rp,cn1,cn2,cn3,nn1,nn2,nn3,nr1,nr2,nr3)
          Integer nn1,nn2,nn3, zn, i, j, nodes
           Double Precision FlowZones(0:9,0:4)
          Double Precision, Dimension (0:nodes,0:8) :: FlowField

          double precision zp,rp,dist,cn1,cn2,cn3,nr1,nr2,nr3
                cn1=1. ! Set closest nodes to a high value
                cn2=1.
                cn3=1.
        Do zn=0,9
       if(zp.gt.flowzones(zn,1)) then
       if(zp.lt.flowzones(zn,2)) then
!        Do j=0,n !Find nearest node
         Do j=int(flowzones(zn,3)),int(flowzones(zn,4)) !Find nearest node

        dist=((Flowfield(j,1)-(zp))**2+(Flowfield(j,2)-rp)**2)**.5

        if (dist .lt. cn3) then
         nn3=j
         cn3=dist
        endif
        if (dist .lt. cn2) then
         nn3=nn2
         cn3=cn2
         nn2=j
         cn2=dist
        endif

        if (dist .lt. cn1) then
        nn2=nn1
        cn2=cn1
        nn1=j
```

```
        cn1=dist
        endif
       end do
       end if !flow zone upper
       end if !flow zone lower
       end do !running through zones
       nr1=cn1/(cn1+cn2+cn3)
       nr2=cn2/(cn1+cn2+cn3)
       nr3=cn3/(cn1+cn2+cn3)

       end subroutine

       SUBROUTINE CPCResponse(CPC,tcpc,tdiff,temp,ff,cpcerr)
        Double Precision CPC(0:40,0:1)
        integer good, icpc
        double precision tcpc, mcpc, pcpc,tdiff,cpcerr
        double precision kb,temp,ff,pi
        kb = 1.380658d-23
        pi = 3.14159
            good=0
            do while (good.eq.0)
             tcpc=rand()*40
             icpc=int(tcpc)
             mcpc=(cpc((icpc+1),1)-cpc(icpc,1))
             pcpc=mcpc*tcpc+(cpc(icpc,1)-mcpc*icpc)
             if (rand().LT.pcpc) then
             good=1
             tcpc=(tcpc-icpc)*(cpc((icpc+1),0)-cpc(icpc,0))+cpc(icpc,0)
             tcpc=tcpc*cpcerr
             tdiff=4*(kb*temp/ff*tcpc)**(0.5)*(LOG(2.))**(0.5)*sqrt(-
2d0*LOG(rand()))*cos(2*pi*rand())/.28*tcpc !where is .28 from?
             tdiff=2*(kb*temp/ff*tcpc)**(0.5)*sqrt(-2d0*LOG(rand()))*cos(2*pi*rand()) !I
think this is more correct
            end if
           end do
        END

       SUBROUTINE Langevin(x,vx,sigma1,sigma2,Beta,delt,ff,mp,ux,fx)
        implicit none
       double precision x,vx,sigma1,sigma2,Beta,delt,ff,mp,ux,fx
       double precision xt, vxt, psi, ex, a1, a2
              ex=2.71828d0
             call gaussrand(psi)
             a1 = sigma1*psi
             vxt=vx*ex**(-beta*delt)+(ff*(ux)+fx)/mp/beta*(1-ex**(-beta*delt))+a1
             call gaussrand(psi)
             a2 = sigma2*psi
             xt= x+1/beta*(vxt+vx-2*(ff*(ux)+fx)/mp/beta)*(1-ex**(-beta*delt))/(1+ex**(-
beta*delt))+(fx+ff*(ux))/mp/beta*delt+a2
             vx=vxt
             x=xt
       end

        Subroutine VelVer(x,vx,delt,ff,mp,ux,fx)
            implicit none
          double precision ax,x,vx,delt,ff,mp,ux,fx
          ax=(fx+ff*(ux-vx))/mp
          x=x+vx*delt+.5*ax*delt**2.
          vx=vx+ax*delt
        end
```

A.9 Source Code – Movie Maker.exe

```
program main
  use dislin
  implicit none

     Double Precision, Allocatable :: Location(:,:,:)
    Double Precision, Allocatable :: FlowField(:,:)
    Double Precision, Allocatable :: FreqDist(:,:)
    Real, Allocatable :: xray(:), yray(:), y0ray(:)
    Double Precision, Dimension(0:40,0:1) :: CPC86,CPC88 !Format starting at 0
    Double Precision FlowZones(0:9,0:4)
    Character*50 filename
    Integer numpart, grabs, nodes, numbin !Variable Integers
    Integer n,m,i,j,k !Incrementing integers for general loops
    Integer NodeNum,Col,Row,s,zn,nbin,sframe !Incrementing integers
    Integer good !Logical integer
    Double Precision tmax,delt,t,tpop, tbin !Variables for timing
    Double Precision twrite,dwrite !Variables for Pathlines
    Double Precision
inputmob,measmob,respow,randshift,sampcent,tubedia,zstart,nummode,modehop !Variables to
define inlet particles
    Double Precision dp, cc, mp, ff, rhop, beta , sigma1, sigma2 !Particle variables
    Double Precision pg, mu, Temp, ng, dg, mg, lambda, kn !Gas variables
    Double Precision xp,yp,zp,rp,vxp,vyp,vzp,vrp,xi,yi,zi,ri !Particle position variables
    Double precision xpo,ypo,zpo,distep !Particle position placeholders
    Double Precision ux,uy,uz,ur,fx,fy,fz,fr,theta,DMAV,DMAon ! Flowfield variables
    Integer nn1,nn2,nn3 !Row locations of nearest nodes
    Double Precision dist,cn1,cn2,cn3,nr1,nr2,nr3 !Distances to nearest nodes
    Double Precision tcpc, tdiff !CPC time broadening variables
    Double Precision kb, pi, ex, q !Fixed constants

  CHARACTER (LEN=50) :: CTIT
  CHARACTER (LEN=2)  :: CSTR
  INTEGER :: NY,NXP,NL


  Real Pathlines(1649,8)
!  real, dimension (100) :: xray, yray, y0ray
  real, dimension (100,100) :: zmat
  real, dimension (21) :: Zlvray
  integer, dimension (2) :: NRAY
  real xoff, yoff, xscal, yscal


        Open(1,File='Case.txt') !Open file containing case information
        ! Assign array dimensions based on case info
        Read(1,*) numpart
        Read(1,*) grabs
        Read(1,*) nodes
        Read(1,*) numbin
        Allocate (Location(0:(numpart-1),0:5,0:grabs))
        Allocate (FlowField(0:nodes,0:8))
        Allocate (FreqDist(0:numbin,0:5))
        Allocate (xray(numbin),yray(numbin),y0ray(numbin))
        Read(1,*) tpop !time to populate inlet in seconds
        Read(1,*) tmax !maximum number of seconds for simulation

       tbin=0.02d0

         OPEN (15,FILE='FlowField.txt', STATUS='old')
       Read (15,*) ((FlowField(NodeNum,Col), Col=0,8), NodeNum=0,nodes)

       OPEN (18,FILE='Pathlines.txt', status='old')
       read (18,*) ((Pathlines(i,j), j=1,7),i=1,1648)
       close (18)
```

```
Do i=1,1648
    Pathlines (i,8)=mod(i,3)
end do

        write(filename,*)'FreqDist.txt'
       OPEN (18,FILE='FreqDist.txt', status='old')
       read (18,'(1x,6e12.4)') ((FreqDist(i,j), j=0,5),i=0,(numbin-1))
       close (18)

       do n=0,grabs
        write (filename,*) n,'.txt'
        open (18,File=filename,status='old')
         read (18,*) ((Location(i,j,n), j=0,5),i=0,(numpart-1))
        close (18)



        write (filename,*) n,'.bmp'
        CALL IMGFMT ('rgb')
        CALL SETPAG('DA4L')
!        CALL WINSIZ (1706, 1206)
        CALL METAFL('BMP')
        CALL SCRMOD('REVERS')
        CALL SETFIL (filename)
        CALL DISINI()
        CALL PAGERA()
        CALL COMPLX()
        CALL HEIGHT(40)
        CALL BMPFNT('HELVE')
        write (CTIT,*) 'Drift Tube Ion Mobility Spectrometer '
        NL=NLMESS(CTIT)
        CALL MESSAG(CTIT,(2970-NL)/2,100)
        t=(dble(n)/dble(grabs)*(tmax+tpop)-tpop)
        write (*,*) t
        write (CTIT,'(1x,A,1e11.3)') 'Measurement Time (s) ', t
        NL=NLMESS(CTIT)
        CALL MESSAG(CTIT,(2970-NL)/2,200)
        If (t.lt.0) then
            call color('red')
        write (CTIT,*) 'Drift Voltage Off'
        else
            call color('green')
                    write (CTIT,*) 'Drift Voltage On'
                    end if
        NL=NLMESS(CTIT)
        CALL MESSAG(CTIT,(2970-NL)/2,300)
        call color ('white')
        xoff=1200
        yoff=700
        xscal=5000
        yscal=15000

        nray(1)=10
        nray(2)=10
!        CALL MYLINE (NRAY, 2)
        CALL XMOVE (xoff,(yscal*(-0.02)+yoff))
        CALL XDRAW (xoff,(yscal*0.02+yoff))
        CALL XMOVE ((xscal*(.228))+xoff,(yscal*(0.02)+yoff))
        CALL XDRAW ((xscal*(.228))+xoff,(yscal*(0.003)+yoff))
        CALL XMOVE ((xscal*(.228))+xoff,(yscal*(-0.02)+yoff))
        CALL XDRAW ((xscal*(.228))+xoff,(yscal*(-0.003)+yoff))



! Draw the perimeter
        do i=0,nodes
            if (Flowfield(i,8).le.1.e-5) then
```

```
      nxp = int(Flowfield(i,1)*xscal)+xoff
      ny = int(Flowfield(i,2)*yscal)+yoff
            Call hsymbl(1)
                  CALL SYMBOL(21,nxp,ny)
      ny = int(Flowfield(i,2)*-yscal)+yoff
                  CALL SYMBOL(21,nxp,ny)
                  end if
        end do
! Draw the pathlnes
 CALL TPRVAL (0.5)
 call TPRini

      do i=1,1648
!
        CALL HSYMBL(2)
        CALL COLOR ('red')
        if (mod(n,3).eq.Pathlines(i,8)) then
      nxp = int(Pathlines(i,2)*xscal)+xoff
      ny = int(Pathlines(i,3)*yscal)+yoff
      CALL SYMBOL(21,nxp,ny)
      ny = int(Pathlines(i,3)*(-yscal))+yoff
      CALL SYMBOL(21,nxp,ny)
endif
      end do
      CALL TPRFIN

!Draw the dots
      do i=0,(numpart-1)
!        CALL HSYMBL(int(location(i,3,n)*1.e9))
       if (location(i,3,n).le.25000.*1.) then
        CALL HSYMBL(5)
        CALL COLOR ('blue')
        else if (location(i,3,n).le.25000.*2.) then
        CALL HSYMBL(10)
        CALL COLOR ('green')
        else if (location(i,3,n).le.25000.*3.) then
                CALL HSYMBL(15)
        CALL COLOR ('yellow')
        else
                 CALL HSYMBL(20)
        CALL COLOR ('orange')
       endif

!       uncomment for charger
!       if (location(i,5,n).eq.1) then
!                  CALL HSYMBL(20)
!        CALL COLOR ('orange')
!        end if

      nxp = int(Location(i,1,n)*xscal)+xoff
      ny = int(Location(i,2,n)*yscal)+yoff
      CALL SYMBOL(21,nxp,ny)
      ny = int(Location(i,2,n)*(-yscal))+yoff
      CALL SYMBOL(21,nxp,ny)

        CALL COLOR ('white')
      nxp = int(Location(i,1,n)*xscal)+xoff
      ny = int(Location(i,2,n)*yscal)+yoff
      CALL SYMBOL(15,nxp,ny)
      ny = int(Location(i,2,n)*(-yscal))+yoff
      CALL SYMBOL(15,nxp,ny)


      end do



        j=0
```

```
        do i=0,numbin
         if (FreqDist(i,1).gt.j) then
        j=FreqDist(i,1)
        endif

        end do

      CALL COMPLX()
      CALL TICKS(1,'X')
      CALL AXSLEN (2500, 700)
      CALL AXSPOS(300,1900)
      CALL COLOR('WHITE')
      CALL AXSSCL ('log', 'x')
      CALL LABELS ('exp', 'x')
      CALL HEIGHT(30)
      CALL BMPFNT('HELVE')
      CALL TITLIN('Mobility Distribution',3)
      CALL NAME ('Time (s)', 'x')
                 CALL NAME ('Number/bin', 'y')
       CALL VKYTIT (-100)
         CALL GRAF((-1.),log10(real(FreqDist((Numbin-1),0))),(-
1.),(.5),0.,real(j+1),0.,real((j+1)/5.))
write (6,*) log10(real(FreqDist((numbin-1),0))), 'here'
!write (*,*) FreqDist((numbin-1),0)
          CALL LABELS('none','BARS')
          CALL LABPOS('OUTSIDE','BARS')
          CALL COLOR('RED')
        do i=1,(numbin)
        yray(i)=0.
        y0ray(i)=0.
        xray(i)=FreqDist((i-1),0)
!        write (*,*) xray(i)
        end do

        if (t.gt.0.) then
        do i=1,(nint((log10(t)+1.)*(numbin-1.)/(log10(tmax)+1.)))
        yray(i)=FreqDist(i,1)
!        write (*,*) yray(i)

        end do
        do i = (1+nint((log10(t)+1.)*(numbin-1.)/(log10(tmax)+1.))),(numbin-1)
        yray(i)=0.
        end do
        end if



          CALL BARS(Xray,Yray,Y0ray,numbin)
          write (6,*) Xray(87), yray(87)
          CALL COLOR('FORE')

          CALL HEIGHT(50)
          CALL TITLE()


        CALL ENDGRF()
         if (FreqDist(i,1).gt.j) then
        j=FreqDist(i,1)
        endif
        yray(1)=0.
        yray(2)=dble(j+1)
        CALL SETSCL (YRAY, 2, 'y')



        !CALL BARS (XRAY, Y1RAY, Y2RAY, 101)
        CALL COLOR ('white')
```

```
        CALL AXSPOS (300, 2000)
        CALL AXSLEN (2500, 700)
!        CALL AXSSCL ('log', 'x')

        CALL HEIGHT(20)
        do i=1,(numbin-1)
        xray(i)=0.
        end do
        if (t.gt.0.) then
        do i=1,(nint((log10(t)+1.)*(numbin-1.)/(log10(tmax)+1.)))
        xray(i)=FreqDist(i,1)
        end do
        do i = (1+nint((log10(t)+1.)*(numbin-1.)/(log10(tmax)+1.))),(numbin-1)
        xray(i)=0.
        end do
        end if
!        CALL QPLBAR (XRAY, (numbin-1))
      CALL DISFIN


       end do
       end program
```

A.10 Source Code – Fluent UDF

```
/*Particle Motion UDF
Electrostatic force adapted from Hyo K Ahn Masters project
Drag and Brownian force from Xialong Wang Thesis
Tied together by Derek Oberreit Aug-31-2010*/
#include "udf.h"
#include "sg.h"
#include "prop.h"
#include "dpm.h"
#include "surf.h"
#include "random.h"
#define gasconst 1.38e-23
#define mfp_r 6.74e-8
#define S 110.4
#define T_r 296.15
#define p_r 1.01e5
#define gama 1.4
#define fm 0.824 /*momentum accomodation coefficient*/
#define A 1.142
#define Q 0.558
#define B 0.999
#define pi 3.1415926
#define TSTART 0.0
#define TSCAN 60.0
#define VLO 5000.0
#define VHI 5000.0 /*Model potential field at this value*/
#define qe -1.6e-19
/************************************************************************
**********************/
DEFINE_ADJUST(PotentialToGradient, domain)
{
Thread *t;
cell_t c;
/*domain = Get_Domain(0);*/
```

```
/*The conditional statement if (NULL != THREAD STORAGE(t,SV UDS I(0)))
is used to
 check if the storage for the user-defined scalar with index 0 has
been allocated, while
 NULL != T STORAGE R NV(t,SV UDSI G(0)) checks whether the storage of
the gradient
 of the user-defined scalar with index 0 has been allocated.*/
thread_loop_c (t,domain)

if (NULL != THREAD_STORAGE(t,SV_UDS_I(0) ) &&
NULL != T_STORAGE_R_NV(t,SV_UDSI_G(0)))
{
begin_c_loop (c,t)
/*Calculate the gradient at each point in the mesh and store each component in
separate array*/
{
       C_UDMI(c,t,0) = C_UDSI_G(c,t,0)[0];
       C_UDMI(c,t,1) = C_UDSI_G(c,t,0)[1];
       C_UDMI(c,t,2) = C_UDSI_G(c,t,0)[2];
}
end_c_loop(c,t)

}
}
/**********************************************************************
**********************/
/* Diffusion coefficient can be any non-zero value in this case.*/
DEFINE_DIFFUSIVITY(diff_e,c,t,i)
{
return 8.85418782e-12;
}


/**********************************************************************
**********************/
DEFINE_UDS_FLUX(PotentialField,f,t,i)
{
return 0e1;
}
/**********************************************************************
**********************/

DEFINE_UDS_FLUX(my_uds_flux,f,t,i)
{
  cell_t  c0,  c1 = -1;
  Thread *t0, *t1 = NULL;
  real NV_VEC(psi_vec), NV_VEC(Area), flux = (0.0);
  real Zp = 1.79e-6;
  c0 = F_C0(f,t);
  t0 = F_C0_THREAD(f,t);
  F_AREA(Area,f,t);

  /* If face lies at domain boundary, use face values; */
  /* If face lies IN the domain, use average of adjacent cells. */

 if (BOUNDARY_FACE_THREAD_P(t)) /*Most face values will be available*/
    {
      real dens;

      /* Depending on its BC, density may not be set on face thread*/
```

```
      if (NNULLP(THREAD_STORAGE(t,SV_DENSITY)))
        dens = F_R(f,t);   /* Set dens to face value if available */
      else
        dens = C_R(c0,t0); /* else, set dens to cell value */

      NV_DS(psi_vec,  =, (F_U(f,t)+Zp*C_UDSI_G(c0,t0,0)[0]),
(F_V(f,t)+Zp*C_UDSI_G(c0,t0,0)[1]), (F_W(f,t)+Zp*C_UDSI_G(c0,t0,0)[2]), *,
dens);

      flux = NV_DOT(psi_vec, Area); /* flux through Face */
    }
  else
    {
      c1 = F_C1(f,t);       /* Get cell on other side of face */
      t1 = F_C1_THREAD(f,t);

      NV_DS(psi_vec,  =,
(C_U(c0,t0)+Zp*C_UDSI_G(c0,t0,0)[0]),(C_V(c0,t0)+Zp*C_UDSI_G(c0,t0,0)[1]),(C_W(
c0,t0)+Zp*C_UDSI_G(c0,t0,0)[2]),*,C_R(c0,t0));
      NV_DS(psi_vec, +=,
(C_U(c1,t1)+Zp*C_UDSI_G(c0,t0,0)[0]),(C_V(c1,t1)+Zp*C_UDSI_G(c0,t0,0)[1]),(C_W(
c1,t1)+Zp*C_UDSI_G(c0,t0,0)[2]),*,C_R(c1,t1));

      flux = NV_DOT(psi_vec, Area)/2.0; /* Average flux through face */
    }

  /* ANSYS FLUENT will multiply the returned value by phi_f (the scalar's
     value at the face) to get the "complete'' advective term.  */

  return flux;
}
/************************************************************************
**********************/

/*drag force according to Peng Liu's thesis */
/*this model accounts for different Rep and Map regions */
/*modified on July 21, 2004 */
/*Xiaoliang Wang*/

DEFINE_DPM_DRAG(LiuDrag, Re, p)
{
  double drag_force;
/* get the current cell that particle sit in*/
  cell_t c = RP_CELL(&p->cCell);
  Thread *t = RP_THREAD(&p->cCell);
  double p_operating = RP_Get_Real ("operating-pressure");
  double pressure=C_P(c,t)+p_operating;
  double temp=C_T(c,t);
  double viscosity=C_MU_L(c,t);
  double density=C_R(c,t);
  double Dp=P_DIAM(p);
  double conc,mfp,Cc;
  double w,sound,Ma,Kn,Ccont,Cfm,Cinv,Cd;

  sound=pow(gama*C_RGAS(c,t)*temp, 0.5);
  Ma=Re*viscosity/density/Dp/sound;

  mfp=mfp_r*temp/T_r*p_r/pressure*(1.0+S/T_r)/(1.0+S/temp);
  Kn=mfp/Dp;
```

```
  Ccont=24.0/Re*(1.0+0.15*pow(Re, 0.687))*(1+exp(-0.427/pow(Ma,4.63)));

Cfm=2.0/pow(gama*pi/2.0,0.5)/Ma*(pow(64.0/9.0+gama*pi/2.0*pow(Ma,2.0),0.5)+fm*p
i/3.0);

  Cinv=1.0/Ccont+1.0/Cfm*(A+Q*exp(-B/2.0/Kn))/(A+Q);
  Cd=1.0/Cinv;

  drag_force = 18.0/24.0*Cd*Re;

/*       Message("%f,%f,%f,%f,%f,%f\n",Re, Ma,
temp,pressure,viscosity,drag_force);*/
      return (drag_force);
}


DEFINE_DPM_DRAG(WangDrag, Re, p)
{
  double drag_force;
/* get the current cell that particle sit in*/
  cell_t c = RP_CELL(&p->cCell);
  Thread *t = RP_THREAD(&p->cCell);
  double p_operating = RP_Get_Real ("operating-pressure");
  double pressure=C_P(c,t)+p_operating;
 /* double pressure=C_P(c,t)+101325.0;*/
  double temp=C_T(c,t);
  double Dp=P_DIAM(p);
  double conc,mfp,Cc;
  double w;

  /*conc=pressure/gasconst/temp;*/
  /* mfp=1.0/(sqrt(2.0)*conc*M_PI*Dm*Dm);*/
  mfp=mfp_r*temp/T_r*p_r/pressure*(1.0+S/T_r)/(1.0+S/temp);
  Cc=1.0+2.0*mfp/Dp*(1.257+0.4*exp(-1.1*Dp/2.0/mfp));

    if (Re < 0.01)
    {
    drag_force=18.0/Cc;
    }
  else if (Re < 20.0)
    {
    w = log10(Re);
    drag_force = (18.0 + 2.367*pow(Re,0.82-0.05*w))/Cc ;
    }
  else
    /* Note: suggested valid range 20 < Re < 260 */
    {
    drag_force = (18.0 + 3.483*pow(Re,0.6305))/Cc ;
       }
       /*  Message("%f,%f,%e,%f\n",p_operating, pressure,Cc,drag_force);*/
      return (drag_force);
}

/************************************************************/
/* Calculate the Brownian force according to DPM manual (Chap 19)*/
/* p. 19-10                                                 */
/* Xiaoliang Wang 2004/03/03                                */
/************************************************************/
```

```
DEFINE_DPM_BODY_FORCE(Brownian, p, i)
{
  double bforce;
  cell_t c = RP_CELL(&p->cCell);
  Thread *t = RP_THREAD(&p->cCell);
  double p_operating = RP_Get_Real ("operating-pressure");
  double pressure=C_P(c,t)+p_operating;
  double temp=C_T(c,t);
  double mu=C_MU_L(c,t);
  double rho=C_R(c,t);
  double nu=mu/rho;

  double Dp=P_DIAM(p);
  double rhop=P_RHO(p);
  double pdt=P_DT(p);

  double conc,mfp,Cc;
  double  x1,x2,w,y1,y2,y3;
  double ss;

  conc=pressure/gasconst/temp;

/*calculate mean free path and slip correction*/
  mfp=mfp_r*temp/T_r*p_r/pressure*(1.0+S/T_r)/(1.0+S/temp);
  Cc=1.0+2.0*mfp/Dp*(1.257+0.4*exp(-1.1*Dp/2.0/mfp));

/*-------------------------------------------------------------*/
/*       code to generate Gaussian random number           */
/*      ref: www.taygeta.com/random/gaussian.htm           */
/*  do {        */
/*        x1 = 2.0 * ran()-1.0;*/
/*        x2 = 2.0 * ran()-1.0;*/
/*        w = x1 * x1 + x2 * x2;*/
/*  }while (w>=1.0);*/
/*  w=sqrt((-2.0*ln(w))/w);*/
/*  y1=x1*w;*/
/*  y2=x2*w;*/
/*-------------------------------------------------------------*/

  y1=cheap_gauss_random();
  y2=cheap_gauss_random();
  y3=cheap_gauss_random();

  /*  if(pdt<1.0e-12) pdt=1.336637e-05;*/
  if(P_TIME(p)==0.0) bforce=0.0;
  else
   {

ss=216.0*nu*gasconst*temp/pow(pi,2.0)/rho/pow(Dp,5.0)/pow((rhop/rho),2.0)/Cc;
    if(i==0) bforce=y1*sqrt(pi*ss/pdt);
    else if(i==1) bforce=y2*sqrt(pi*ss/pdt);
    else if(i==2) bforce=y3*sqrt(pi*ss/pdt);
  /*printf("%e,%e,%e,%e\n",nu,rho,rhop,mu);*/
  /*printf("%e,%e,%e,%e,%e,%e\n",y1,y2,ss,pdt,Cc,bforce);*/
   }

/* an acceleration should be returned */
  return (bforce);
}
```

```
/************************************************************/
/* Calculate the Brownian force according to DPM manual (Chap 19)*/
/* p. 19-10                                                 */
/* Xiaoliang Wang 2004/03/03                                */
/* Electrostatic body force added by Derek Oberreit 2010-08-31*/
/************************************************************/


DEFINE_DPM_BODY_FORCE(BrownianElectrostatic, p, i)
{
  double bforce;
  cell_t c = RP_CELL(&p->cCell);
  Thread *t = RP_THREAD(&p->cCell);
  double p_operating = RP_Get_Real ("operating-pressure");
  double pressure=C_P(c,t)+p_operating;
  double temp=C_T(c,t);
  double mu=C_MU_L(c,t);
  double rho=C_R(c,t);
  double nu=mu/rho;

  double Dp=P_DIAM(p);
  double rhop=P_RHO(p);
  double massp=P_MASS(p);
  double pdt=P_DT(p);

  double conc,mfp,Cc;
  double  x1,x2,w,y1,y2,y3;
  double ss;

  conc=pressure/gasconst/temp;

/*calculate mean free path and slip correction*/
  mfp=mfp_r*temp/T_r*p_r/pressure*(1.0+S/T_r)/(1.0+S/temp);
  Cc=1.0+2.0*mfp/Dp*(1.257+0.4*exp(-1.1*Dp/2.0/mfp));

/*-----------------------------------------------------------*/
/*       code to generate Gaussian random number             */
/*      ref: www.taygeta.com/random/gaussian.htm             */
/*  do {        */
/*        x1 = 2.0 * ran()-1.0;*/
/*        x2 = 2.0 * ran()-1.0;*/
/*        w = x1 * x1 + x2 * x2;*/
/*  }while (w>=1.0);*/
/*  w=sqrt((-2.0*ln(w))/w);*/
/*  y1=x1*w;*/
/*  y2=x2*w;*/
/*-----------------------------------------------------------*/

  y1=cheap_gauss_random();
  y2=cheap_gauss_random();
  y3=cheap_gauss_random();

  /*  if(pdt<1.0e-12) pdt=1.336637e-05;*/
  if(P_TIME(p)==0.0) bforce=0.0;
  else
   {

ss=216.0*nu*gasconst*temp/pow(pi,2.0)/rho/pow(Dp,5.0)/pow((rhop/rho),2.0)/Cc;
    if(i==0) bforce=y1*sqrt(pi*ss/pdt)+qe*C_UDSI_G(c,t,0)[0]/massp;
```

```
    else if(i==1) bforce=y2*sqrt(pi*ss/pdt)+qe*C_UDSI_G(c,t,0)[1]/massp;
    else if(i==2) bforce=y3*sqrt(pi*ss/pdt)+qe*C_UDSI_G(c,t,0)[2]/massp;
  /*printf("%e,%e,%e,%e\n",nu,rho,rhop,mu);*/
  /*printf("%e,%e,%e,%e,%e,%e\n",y1,y2,ss,pdt,Cc,bforce);*/
   }

/* an acceleration should be returned */
  return (bforce);
}

DEFINE_DPM_BODY_FORCE(Electrostatic,p,i)
{
/*Read position*/
cell_t c = RP_CELL(&p->cCell);
Thread *t = RP_THREAD(&p->cCell);
double bforce;
double field;
/*field=((VHI-VLO)/TSCAN*(P_TIME(p)-TSTART)+VLO)/VHI;*/ /*use for positive
ramp*/
/*field=((VHI-VLO)/TSCAN*(P_TIME(p)-TSTART)+VLO)/VLO;*/ /*use for negative
ramp*/
field=9.0;
if(P_TIME(p)>= TSTART)
/* Calculate body force based on field at particle position */
{
if(i == 0) bforce = qe*field*C_UDSI_G(c,t,0)[0];
else if(i == 1) bforce = qe*field*C_UDSI_G(c,t,0)[1];
else if(i == 2) bforce = qe*field*C_UDSI_G(c,t,0)[2];
}
else
bforce = 0.0;
/* an acceleration should be returned */
return (bforce/P_MASS(p));
}

DEFINE_PROFILE(Inlet,t,i)
{
  real x[ND_ND];               /* this will hold the position vector */
  real y;
  face_t f;
if(CURRENT_TIME < .5)
  begin_f_loop(f,t)
    {
      F_CENTROID(x,f,t);
      y = x[1];
      F_PROFILE(f,t,i) = .253+((-.253)-.253)*CURRENT_TIME/0.1;
    }
  end_f_loop(f,t)
}



DEFINE_PROFILE(Outlet,t,i)
{
  real x[ND_ND];               /* this will hold the position vector */
  real y;
  face_t f;
if(CURRENT_TIME < .5)
  begin_f_loop(f,t)
    {
```

```
      F_CENTROID(x,f,t);
      y = x[1];
      F_PROFILE(f,t,i) = -.722+(-.0344-(-.722))*CURRENT_TIME/0.1;
    }
  end_f_loop(f,t)
}
```

Appendix B Schematics and Diagrams

B.1 DTIMS High Voltage Switcher